CERN-THESIS-2013-412

NLO Corrections and Parton Showers in the LHC Era

Zur Erlangung des akademischen Grades eines
DOKTORS DER NATURWISSENSCHAFTEN
von der Fakultät für Physik des
Karlsruher Institutes für Technologie (KIT)
genehmigte

DISSERTATION

von

Dipl.-Phys. Ken Boris Arnold
aus Bruchsal

Tag der mündlichen Prüfung: 10.5.2013
Referent: Prof. Dr. D. Zeppenfeld
Korreferent: Prof. Dr. M. Steinhauser

Erklärung

Ich versichere, dass ich meine Dissertation selbstständig verfasst und keine anderen als die angegebenen Hilfsmittel benutzt habe. Die Arbeit wurde bisher nicht als Prüfungsarbeit verwendet.

Ich habe an keinem früheren Promotionsverfahren teilgenommen.

Ken Arnold
Karlsruhe, den 8. April 2013

Für Eva

Abstract

The Large Hadron Collider provides a challenging environment, not only for experimentalists. Precise predictions are needed in order to use its potential to full capacity. This thesis focuses on predictions including higher-order corrections in a twofold way. Both results for a pure parton level calculation and for a calculation incorporating a parton shower are presented.

Higgs boson plus photon production via vector boson fusion was implemented in a fully flexible parton-level Monte-Carlo program. The results at next-to-leading order accuracy are discussed. It is found that the corrections are large in some regions of phase space.

For the simulation of a parton shower matched to a next-to-leading order matrix element, a mixed-language runtime interface was established to use existing matrix elements for Higgs boson production via vector boson fusion. Results are discussed for different parton shower algorithms and matching schemes. The simulation is shown to have a substantial dependence on the shower algorithm and matching scheme in some of the examined observables. This indicates a significant systematical uncertainty in such calculations.

Zusammenfassung

Der Large Hadron Collider liefert nicht nur für Experimentalphysiker eine herausfordernde Umgebung. Präzise Vorhersagen sind von Nöten um sein Potential voll ausschöpfen zu können. Das Hauptaugenmerk dieser Arbeit liegt auf Vorhersagen, die Korrekturen höherer Ordnung mit einfließen lassen. Dabei werden zwei Wege beschritten. Sowohl Ergebnisse für eine Rechnung rein auf Partonniveau werden präsentiert, als auch solche einer Rechnung, die einen Partonschauer beinhaltet.

Higgs-Boson-plus-Photon-Produktion durch Fusion schwacher Vektorbosonen wurde in einem flexiblen Monte-Carlo-Programm auf Partonniveau implementiert. Die Ergebnisse in nächstführender Ordnung werden diskutiert. Dabei stellt sich heraus, dass die Korrekturen in manchen Phasenraumregionen groß sind.

Für die Simulation eines Partonschauers in Zusammenarbeit mit einem Matrixelement nächstführender Ordnung wurde ein gemischtsprachiges Laufzeit-Interface etabliert um bereits vorhandene Matrixelemente für Higgs-Boson-Produktion durch Fusion schwacher Eichbosonen nutzen zu können. Die mit verschiedenen Partonschauer-Algorithmen und Matching-Schemata erhaltenen Ergebnisse werden gegenübergestellt. Dabei zeigt sich sowohl eine erhebliche Abhängigkeit vom Partonschauer als auch vom Matching-Schema bei manchen der betrachteten Observablen. Dies deutet auf signifikante systematische Unsicherheiten solcher Rechnungen hin.

Contents

Introduction

Curiosity has always been a major source of motivation of mankind. We, as a race, could only be as successful biologically as we are because we have constantly expanded our knowledge and understanding of nature. Our evolutionary history is a history of the evolution of the human brain, that allowed us to develop control over fire, speech and the motor skills to construct tools.

We have come a long way since then. Although in most cases not necessary for survival anymore, curiosity is still a motor of society today. Our knowledge of nature has increased to the very fundamental building blocks. Although we know today that we can only model physics and will never know the "truth" about subatomic processes, we still strive for a better understanding of the universe.

Philosophiæ Naturalis Principia Mathematica [1], published 1686/1687, is a cornerstone of classical mechanics and already includes a first description of one of the fundamental forces of nature: gravitation. Ironically, although it was the first force to be described, it it still the worst understood today, at least at the quantum level.

Another giant leap was achieved by James Clerk Maxwell, who developed a consistent formulation of classical electromagnetism in 1865 [2]. The understanding of the electromagnetic force was paving the way for modern physics as it introduced fields as physical entities. Also, it was the first Lorentz-covariant theory, long before the formulation of special relativity by Einstein.

The emergence of particle physics is not so clear. Important experimental discoveries date back to the late 19th century, like the discoveries of X-Rays by Röntgen or of radioactivity by Becquerel. On the theory side, the development of quantum mechanics was clearly a mile stone, but not only for particle physics. Technologies that could only be developed by a concise knowledge of quantum mechanics influence our daily lives.

The first relativistic quantum field theory, quantum electrodynamics (QED), was formulated within an ongoing struggle against divergencies by Dirac, Bethe, Tomonaga, Schwinger, Dyson and others. In succession, two more fundamental forces could be theoretically described: the strong and the weak force. To incorporate the latter within a unified description together with QED, the Higgs mechanism of spontaneous symmetry breaking was introduced. It predicted a new particle, the Higgs boson, that remained undiscovered for almost 50 years.

During the past decades, a tremendous effort was made to construct the most powerful human made particle accelerator to date, the Large Hadron Collider

(LHC) and its experiments. It could verify the existence of a new resonance, however, it is still unclear if it is the Higgs boson predicted by the Standard Model of particle physics, which incorporates quantum chromodynamics (QCD) and electroweak interactions.

Currently, there are seven experiments using the machine. The two largest and most famous ones, the multi-purpose detectors ATLAS and CMS, are mainly devoted to detect the Higgs boson and possible signals of physics beyond the Standard Model. ALICE is specialised to produce and measure quark-gluon plasma within lead-lead collisions. LHCb is an asymmetric detector and focuses on measurements of B mesons. It shares a cavern with the smaller MoEDAL experiment. The main purpose of MoEDAL is to detect new stable, massive particles such as magnetic monopoles. The two remaining experiments in the list, TOTEM and LHCf, are both built to resolve particles in the very forward direction. One of the goals of TOTEM is to measure the total cross section of proton-proton collisions. LHCf tries to gain insight to the dynamics of cosmic rays by monitoring neutral pions.

With such a broad physics programme aiming at new physics phenomena, the wish for a better understanding of QCD, a theory which arose already during the sixties and seventies of the last century, seems superfluous at first. However, to find something new it is always necessary to know what is old. Especially to improve the efficiency of ATLAS and CMS, the most precise predictions for observables are needed. At such high energies as at the LHC, the largest distortions hereby come from QCD induced processes.

Calculations for the LHC can be split into at least two different parts: The calculation of the hard matrix element and the event simulation. The hard matrix element is calculated up to a fixed order in the coupling constants. It can be improved by including higher orders. For QCD, next-to-leading order (NLO) calculations in the strong coupling constant are almost standard today.

The event simulation consists of several steps. First, an all order approximation in the limit of soft and collinear emissions is delivered by a parton shower algorithm. Then, hadronisation takes place and converts the final quarks and gluons into bound states. In the final step, these bound states are allowed to decay into observable particles. The thesis at hand is dealing both with matrix element calculations at NLO and with event simulation. However, the part on event simulation will not cover the whole evolution, but only parton showers.

In Chapter 1, an introduction to the theoretical foundations is given to prepare the ground for discussions. The Standard Model of particle physics and its particle content is outlined. Electroweak theory is sketched in short by an explanation of the basic principles of spontaneous symmetry breaking. The rise of gauge boson masses and the production of SM Higgs bosons at the LHC are revisited. At the end of the chapter, QCD and some of its implications such as asymptotic freedom are explained.

Chapter 2 continues the discussion of the basics, but focuses on techniques that are common within calculations in high-energy physics. An introduction to

Monte-Carlo methods is given. The structure of event generators is discussed and the need for jet algorithms clarified. The idea of parton shower algorithms and their validity are highlighted, as they make up a substantial part of this thesis. A way of sequential phase space decomposition is introduced, which was used for the parton-shower part of this work.

At the end of Chapter 2, the difficulties that arise in QCD at NLO are explained together with their solutions. For matrix element calculations, a subtraction formalism is needed to render the different integrals separately finite to make them solvable by numerical integration. When entering a parton shower algorithm with an NLO matrix element, new problems arise as there are certain kinematical regimes that are populated by both approximations, which leads to a double counting of contributions. These have to be removed for a consistent calculation. That procedure is known as NLO matching. There are two different matching schemes available: MC@NLO [3] and POWHEG [4, 5].

Within Chapter 3, the second part of this thesis begins, which deals with NLO QCD corrections to $H\gamma jj$ production via vector boson fusion (VBF). VBF is one of the dominant channels for Higgs boson production and due to its event topology, it plays an important role not only for the detection of the Higgs boson, but also for the measurement of its couplings. The additional photon in the process may help to disentangle processes with a decay $H \to b\bar{b}$ from their QCD backgrounds. For this thesis, the process of $H\gamma jj$ production was calculated up to NLO QCD accuracy. The calculation was implemented in form of a flexible Monte-Carlo program and is publicly available within the package VBFNLO [6].

Chapter 4 starts the third part of the thesis at hand, which covers NLO matched Hjj production by fusion of weak gauge bosons. This process is especially interesting for parton shower simulations, as it features well-separated jets in different detector hemispheres with a large gap in between, where radiation is suppressed. For the matched calculations, the Matchbox addon to Herwig++ [7, 8] was used, which allows automated fixed order and matched NLO calculations, once the matrix elements and some bookkeeping information are supplied. As part of the work for this thesis, an interface between Matchbox and VBFNLO was established, which allows to use the VBFNLO Hjj matrix elements within Matchbox.

The chapter begins by explaining several details of Herwig++ that are needed later on. The focus here lies on the generation of phase space and the parton shower algorithms. The two different shower implementations that are available within Herwig++ are explained. These are the default shower with Altarelli-Parisi splitting kernels and the dipole shower, based on Catani-Seymour kernels. As the latter has an additional freedom in the distribution of transverse momentum, two different splitting schemes are contrasted.

Within Chapter 5, the setup of the analysis is described in detail. The steps that were taken to ensure the validity of the implementation are also presented.

In Chapter 6, the two shower implementations are compared within a LO plus shower calculation of the Hjj process. It is important to understand the modifications that are introduced during the shower. As the two shower algorithms differ

in their behaviour away from the soft and collinear limits, the comparison of the two can be used to estimate the systematic uncertainties.

Chapter 7 is dedicated to the comparison of the two matching schemes, MC@NLO and POWHEG. For precise predictions for the LHC, their differences need to be known and their behaviour needs to be understood. Matchbox delivers the ideal framework for such a comparison, as it allows to run both matching schemes within the same setup.

At the end of this thesis, two appendices document the structure of the implementations that were needed for the calculations whose results were presented.

Part I

Basics

Chapter 1

Foundations of high-energy physics

The first part of this thesis sheds light on the groundwork of contemporary high energy particle physics. The historical background for the development of the Standard Model (SM) of particle physics is outlined and the model is described shortly. Subsequently, the two main ingredients of the SM, namely electroweak theory and quantum chromodynamics (QCD), receive further discussion. By the end of this chapter, the main ingredients of the SM and some of their implications will have been explained, which compose the theoretical background of the work at hand.

1.1 The Standard Model of particle physics

The SM is an outstandingly successful theory, capable of describing almost all observed physical forces. Its predictions can be astonishingly exact, for example in the case of the Landé g-factor. Its success is also an annoyance, at least from some physicists point of view. Knowing that in the high-energy regime some new theory must be valid, theorists around the world are trying to find hints that point out how that new theory may look like. The SM describes three of the four fundamental forces with an unrivalled precision. Gravity is not included as the Einstein field equations can not be quantised in a consistent way because they are not renormalisable. Although some ideas exist, no theory of quantum gravity could be confirmed experimentally yet.

Particles in the SM can be differentiated into two groups: Fermions, with half-integer spin and bosons with integer spin. Fermions are further divided into left- and righthanded quarks,

$$\begin{pmatrix} u \\ d \end{pmatrix}_L, \qquad \begin{pmatrix} c \\ s \end{pmatrix}_L, \qquad \begin{pmatrix} t \\ b \end{pmatrix}_L,$$

$$u_R, \qquad d_R, \qquad c_R, \qquad s_R, \qquad t_R, \qquad b_R, \tag{1.1}$$

and left- and righthanded leptons,

$$\begin{pmatrix} e \\ \nu_e \end{pmatrix}_L, \qquad \begin{pmatrix} \mu \\ \nu_\mu \end{pmatrix}_L, \qquad \begin{pmatrix} \tau \\ \nu_\tau \end{pmatrix}_L,$$

$$e_R, \qquad \nu_{eR}, \qquad \mu_R, \qquad \nu_{\mu R}, \qquad \tau_R, \qquad \nu_{\tau R}. \tag{1.2}$$

Lefthanded fields are doublets under $SU(2)_L$ transformations whereas righthanded fields act as singlets. Therefore, it is debatable if the right-handed neutrinos $\nu_{e,\mu,\tau R}$ are already particles beyond the Standard Model as they do not directly participate in any of the interactions of the SM, and thus remain undiscovered. However, they are needed within the SM to generate nonzero neutrino masses, therefore they were added here.

Bosons in the SM with spin 1 are the force carriers of the strong and electroweak force

$$g \qquad A \qquad W^\pm \qquad Z, \tag{1.3}$$

which are called gluons, photons, W and Z bosons. In addition, there is a boson of spin 0, the only fundamental scalar particle in the model, that is

$$H, \tag{1.4}$$

the famous Higgs boson, which recently even made its way into daily news (under a religiously crooked and misleading name that shall not be mentioned here).

The parts of the Standard Model emerged somewhere around the 70's of the last century, when many of the central ingredients were still missing, but were discovered piece by piece. Discoveries included the gluon [9] 1979 at DESY, the W boson [10] and the Z boson [11] 1983 at CERN, and the top quark [12,13] 1995 at Fermilab.

One part was still missing: The Higgs boson, the quantum of a scalar field breaking electroweak symmetry and leading to the observed particle masses, still awaited its discovery. Very recently, a new resonance showed up [14, 15], which is very probable *a* Higgs boson [16,17], but not necessarily *the* Higgs boson postulated within the SM. Up to now, it is not known whether the newly discovered resonance has spin 0 or 2 [18]. Spin 1 can be excluded because of observations of decays into γ pairs, which is forbidden for spin 1 particles by the Landau-Yang theorem [19,20] due to angular momentum conservation. Once its spin has been determined, also the couplings of the new resonance will need to be measured to confirm the existence of a SM-like Higgs boson.

1.2 Electroweak symmetry breaking

The current section is dedicated to the theory of electroweak interactions and the Higgs boson. Within this section, the existence of a Higgs field is motivated by

gauge field masses, which can be generated by a Higgs field vacuum expectation value. Subsequently, a detour to the experimental side is taken to explain the basics of Higgs production at the LHC.

Electroweak forces in the Standard Model are described by an $SU(2)_L \times U(1)_Y$ gauge theory. As explicit gauge boson mass terms break gauge invariance, they are forbidden. To resolve this contradiction with the high observed masses of W and Z bosons, the symmetry of the Lagrangian must be broken by the ground state, which means by spontaneous symmetry breaking.

Defining an additional scalar field, the Higgs field

$$\mathbf{\Phi} = \frac{1}{\sqrt{2}} \begin{pmatrix} \chi_2(x) + i\chi_1(x) \\ v + H(x) - i\chi_3(x) \end{pmatrix} \tag{1.5}$$

and its contribution to the Lagrangian

$$\begin{aligned} \mathcal{L}_{\text{Higgs}} =& (D_\mu \Phi)^\dagger D^\mu \Phi + \mu^2 \Phi^\dagger \Phi - \frac{\lambda}{2}(\Phi^\dagger \Phi)^2 \\ &+ \sum_{i,j=1}^{N_g} \left(y_e^{ij} \bar{L}^i \Phi e_R^j + y_d^{ij} \bar{Q}^i \Phi d_R^j + y_u^{ji} \bar{Q}^i \tilde{\Phi} u_R^j + \text{h.c.} \right), \end{aligned} \tag{1.6}$$

where the indices i and j run over all fermion generations and the covariant derivative is defined as

$$D_\mu = \partial_\mu - \frac{i}{2} g_1 B_\mu - \frac{i}{2} g_2 \tau^a W_\mu^a, \tag{1.7}$$

results in a ground state which breaks gauge invariance and which can be chosen as $\frac{1}{\sqrt{2}}\binom{0}{v}$. L and Q in (1.6) are the lefthanded isospin doublets of leptons and quarks. e_R, u_R and d_R are the righthanded singlets of leptons, up-type quarks and down-type quarks respectively. $\tilde{\Phi}$ is the hypercharge conjugate of Φ and the coupling constants $y_{\{e,u,d\}}$ are called Yukawa couplings.

After the Higgs field acquires a vacuum expectation value, a $U(1)_{EM}$ symmetry remains. The neutral components of the $SU(2)_L \times U(1)_Y$ gauge fields can be redefined to yield the photon field A, respecting the $U(1)_{EM}$ symmetry, and the Z field, orthogonal to A, by

$$\begin{pmatrix} Z_\mu \\ A_\mu \end{pmatrix} = \frac{1}{\sqrt{g_2^2 + {g_1}^2}} \begin{pmatrix} g_2 W_\mu^3 - g_1 B_\mu \\ g_2 W_\mu^3 + g_1 B_\mu \end{pmatrix} = \begin{pmatrix} \cos\theta_W & -\sin\theta_W \\ \sin\theta_W & \cos\theta_W \end{pmatrix} \begin{pmatrix} W_\mu^3 \\ B_\mu \end{pmatrix}. \tag{1.8}$$

The remaining two components are composed to have positive and negative electromagnetic charge,

$$\begin{aligned} W_\mu^+ &= \frac{1}{\sqrt{2}}(W_\mu^1 - iW_\mu^2), \\ W_\mu^- &= \frac{1}{\sqrt{2}}(W_\mu^1 + iW_\mu^2). \end{aligned} \tag{1.9}$$

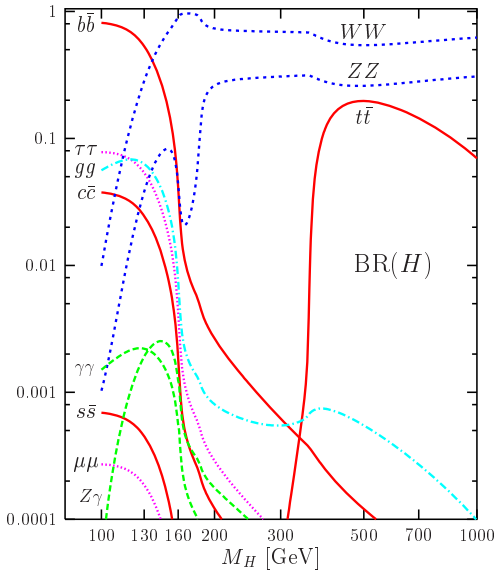

Figure 1.1: SM branching ratios of the Higgs boson (from [21]). If the newly discovered resonance at 126 GeV is a SM Higgs, then decays into $b\bar{b}$ pairs are dominating.

Due to the Yukawa interaction terms in (1.5), also fermions receive a mass by interacting with the vacuum expectation value of the Higgs field. This mass is directly proportional to the coupling strength to the Higgs boson, so that the production cross section and decay widths of a SM Higgs are largest when it can couple to heavy particles.

1.2.1 Higgs boson production at the LHC

As the Higgs boson coupling is directly proportional to the mass of a particle, the various production mechanisms involve heavy particles. The most important production channels are

- Gluon fusion via heavy quark loops
- Fusion of W ad Z bosons (weak or vector boson fusion, WBF/VBF)
- Higgs-strahlung off heavy vector bosons
- Associated production with $t\bar{t}$ pairs

The Feynman diagrams for all these processes are sketched in Figure 1.2.

Gluon fusion is a loop induced process which, in the SM, is dominated by t quark loops. In models with two Higgs doublets, contributions from b quarks can be enhanced. Although gluon fusion has been shown to exhibit a larger cross section over the whole Higgs mass range (see Figure 1.3), the QCD induced process has sizeable higher order corrections. The NLO corrections increase the cross section by

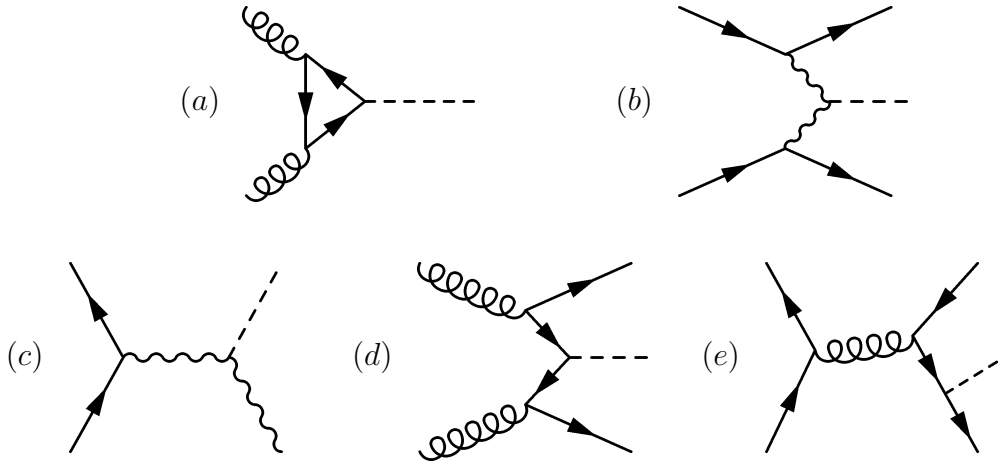

Figure 1.2: Higgs production channels (from [22]): (a): Gluon fusion, (b): Fusion of heavy gauge bosons, (c): Higgs-strahlung, (d): Gluon induced production in association with t quarks, (e): Quark induced production in association with t quarks.

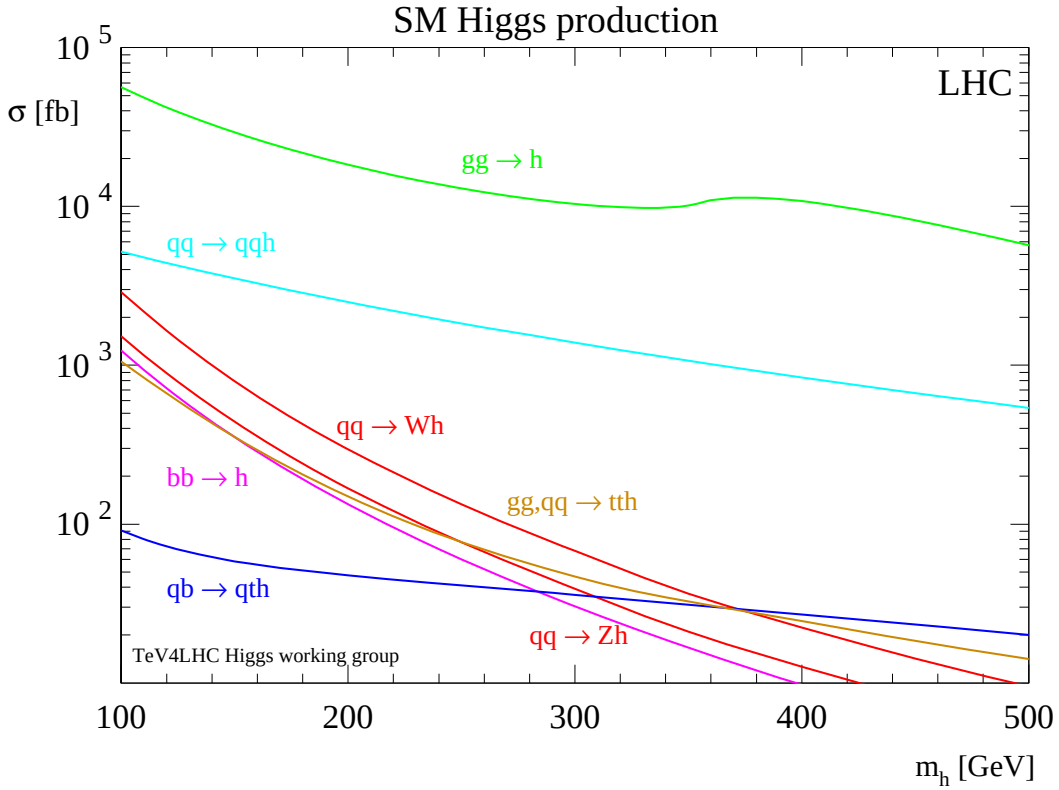

Figure 1.3: SM Higgs cross sections at the LHC with $\sqrt{S} = 14\,\text{TeV}$ (from [23]).

80% to 100% [24]. The NNLO corrections are known [25–27] and add again about 25% to the total cross section. The size of higher order correction goes together with a large amount of additional radiations. The rich colour structure in gluon fusion is adding another problem, as the phase space available for parton shower emissions is large. The result is a highly populated, unspecific event structure.

VBF has the second largest cross section for a SM Higgs boson and Hjj production via vector boson fusion is predicted to have a very specific event topology. The t-channel Feynman diagram of the process results in events which are characterised by a pronounced rapidity gap: The ideal event consists of two jets, widely separated in rapidity, with a Higgs boson in the central region in between. The missing colour exchange between the quark lines at leading order (LO) leads to suppressed QCD radiation in the rapidity gap where the Higgs boson resides, thus providing a relatively clean environment for measuring the Higgs decay products. Hjj VBF processes have a residual scale dependence typically around 5% at NLO [28, 29], which is reduced to below 2% at NNLO [30].

The third largest cross section is contributed by Higgs-strahlung. These processes are experimentally interesting because of the decay modes $H \to W^+W^-$ and $H \to b\bar{b}$, which allow the measurement of the Higgs boson couplings.

Associated production with $t\bar{t}$ pairs has, for low Higgs masses, a very specific signature with four b jets and two W bosons, making the identification very dependent on correct b-tagging. It contributes only with a very small cross section, but allows for the measurement of the t Yukawa coupling.

1.3 Quantum chromodynamics

After the detour to Higgs physics in the last section, the current section is returning to more theoretical aspects again. QCD and some of its implications are discussed. These are the existence of asymptotic freedom and confinement. The latter is posing a QCD inherent problem on low energy calculations while the former is approving the correctness of perturbative expansion in the high energy regime.

After the discovery of an overwhelmingly large number of hadronic resonances, the idea that these had to be bound states of a new class of elementary particles arose. Mesons were thought to be made up of two constituents whereas Baryons should consist of three such particles. Due to the Pauli principle, the discovery of the Δ^{++} particle, a baryon with spin $^3/_2$ meant also the advent of a new fundamental quantum number, the colour charge.

QCD is a non-abelian gauge theory describing strong interactions between colour charged particles. The Lagrangian reads

$$\mathcal{L} = \sum_{i=1}^{N_f} \bar{\Psi}_i (i \not{D} - m_i) \Psi_i - \frac{1}{4} \mathrm{Tr}[F^a_{\mu\nu} F^{a\mu\nu}] \tag{1.10}$$

with Ψ_i being the quark field of type i, $i \in u, d, c, s, b, t$. The covariant derivative is defined as

$$D_\mu = \partial_\mu + ig\frac{\lambda^a}{2}A^a_\mu \tag{1.11}$$

with the Gell-Mann matrices λ^a being the generators of the related Lie algebra in its defining representation. The Lie bracket is defined as

$$[\frac{\lambda^a}{2}, \frac{\lambda^b}{2}] = f^{abc}\frac{\lambda^c}{2}, \tag{1.12}$$

where the structure constants can be derived as

$$f^{abc} = -\frac{1}{4}\left(\mathrm{Tr}[\lambda^a\lambda^b\lambda^c] - \mathrm{Tr}[\lambda^c\lambda^b\lambda^a]\right). \tag{1.13}$$

The field strength tensor in (1.10) is defined by

$$F^a_{\mu\nu}(x) = \partial_\mu A^a_\nu(x) - \partial_\nu A^a_\mu(x) - gf^{abc}A^b_\mu(x)A^c_\nu(x). \tag{1.14}$$

A well known strategy to solve problems in physics is to use perturbation theory. The general procedure is to solve an easier version of the problem and treat the real problem as a minor deviation from the easier version, which can be Taylor-expanded in a small parameter and then solved order by order until the necessary precision is achieved.

In perturbative quantum field theory, transition matrix elements are calculated within an expansion of the coupling constant $\alpha_S = g_S^2/4\pi$. The differential cross section for a process $a + b \to X$ is then constructed with the help of the matrix element for this process $\mathcal{M}_{a+b\to X}$, a phase space element $\mathrm{d}\phi_X$, and a flux factor for the incoming particles as

$$\mathrm{d}\sigma_{a+b\to X} = \frac{1}{4\sqrt{(p_a \cdot p_b)^2 - p_a^2 p_b^2}}\left|\mathcal{M}_{a+b\to X}\right|\mathrm{d}\phi_X. \tag{1.15}$$

1.3.1 Asymptotic freedom and confinement

As with most other theories in modern physics, also QCD cannot be solved exactly. Even worse, at low energies, its coupling constant is large, which makes it impossible to solve by a perturbative expansion. Low energy bound states of QCD, such as the proton, need to be accessed by other methods, like for example lattice gauge theory. With increasing energy, however, its coupling constant decreases, so that a solution by perturbative expansion becomes feasible.

The evolution of the strong coupling constant eases the intuitive understanding of two remarkable features of QCD: Confinement and asymptotic freedom. To the present day, no free colour charged objects have ever been observed. A very appealing and simple picture of the problem is that the gluon field between colour charged objects manifests itself in the form of a narrow flux tube, because the field

itself carries colour. When separating the original colour charges more and more, the energy density of the flux tube increases until it rips, inducing pair production. However, the true theoretical foundations of confinement are not understood, although there are several different proposals (see [31] for a review).

On the other side of the energy spectrum, in high energy reactions, it was observed that the constituents of hadrons behave as free particles. For the theoretical study of this property, named asymptotic freedom, Gross, Politzer and Wilczek [32, 33] were awarded with a Nobel prize in 2004.

The fact that the coupling constant needs to evolve with the energy scale of the process is a consequence of the renormalisation programme. Within higher-order calculations in quantum field theories, divergencies arise within loop diagrams. When computing an amplitude with a loop, an integration over the loop momentum needs to be done. As there is no natural limit on the upper boundary of the loop momentum, the integrals may diverge as the integration range approaches infinity.

The problem is treated by introducing a subtraction point at which the integral is split into a convergent and a divergent piece. When the divergencies are regularised and carried through the calculation, they can be absorbed by redefining parameters of the Lagrangian. The motivation behind that approach is that *bare* parameters of the theory are not measurable and thus, are undefined. Therefore, nothing prevents them from being divergent. The ultraviolet divergencies from the higher order calculation cancel against the divergencies in the bare parameters and leave the measurable *physical* quantities as finite objects.

There is, however, an ambiguity in the procedure. The subtraction point is at an arbitrary energy scale, so varying it may not affect the physical observables. As the bare parameters should be fixed, a change in the subtraction point must be accompanied with a change in more than one renormalised parameter which cancels at the level of observables. In practice, this introduces a scaling behaviour in the coupling constant of the theory, which can be expressed by the so-called beta function,

$$Q^2 \frac{\partial \alpha_S(Q^2)}{\partial Q^2} = \beta(\alpha_S). \tag{1.16}$$

Moving back to QCD, the behaviour of decreasing coupling at high energies is explained by the actual form of the beta function. Just like other quantities in high energy physics, it can be calculated order by order in the strong coupling constant. As the beta function up to one-loop approximation

$$\beta\left(g(\mu^2)\right) = \frac{\partial g(\mu^2)}{\partial \ln(\mu^2)} = -\frac{g^3\left((\mu^2)\right)}{16\pi^2}\left(11 - \frac{2}{3}N_f\right), \tag{1.17}$$

which governs the evolution of α_S, is negative for the known number of quark flavours $N_f = 6$, the strong coupling constant must decrease with increasing energy.

During the transition from a high scale where the hard matrix element can be calculated in perturbation theory down to a lower cutoff scale, additional radiative emissions happen. They can be approximated in the limit of being soft and/or

collinear, in which case their kinematical structure overcomes the smallness of the coupling constant. This leads to the rise of large logarithmic corrections and is the realm of the parton shower approximation, which will be explained later.

1.3.2 Parton distribution functions

For hadronic collisions where in the matrix element the incoming particles a and b are constituents of a bound state, the differential cross section in (1.15) needs to be convoluted with parton distribution functions (PDFs), as only the momentum of the colliding hadron is fixed by the accelerator. The hadronic cross section is written as

$$\sigma_{\text{Hadronic}} = \sum_{a,b} \int_0^1 \mathrm{d}x_a f_a(x_a, \mu_{F,a}) \int_0^1 \mathrm{d}x_b f_b(x_b, \mu_{F,b}) \int \mathrm{d}\sigma^{a,b}. \tag{1.18}$$

a and b index the type of incoming partons and $\sigma^{a,b}$ is the corresponding partonic cross section. The PDF factors f_a and f_b depend on the momentum fractions x of the incoming partons and the factorisation scales μ_F.

PDFs give the probability to find a parton with a given momentum fraction x at a certain factorisation scale μ_F inside the colliding hadron and open the possibility to have a theoretically well defined initial state for the calculation of matrix elements. As hadronic bound states necessarily comprise low energy physics, PDFs contain non-perturbative physics which needs to be fitted to data. Their evolution with varying scales, however, can be calculated with the help of the Dokshitzer-Gribov-Lipatov-Altarelli-Parisi (DGLAP) evolution equations [34–36].

Chapter 2

Calculational techniques for numerical evaluations

After the fundamentals of phenomenological high energy physics were discussed in the previous chapter, we move on to more specific solutions to problems in the field. Within the current section, the basic ideas behind the methods used in the thesis at hand shall be reviewed. The starting point is a general introduction into Monte-Carlo methods, the name under which probabilistic calculation approaches are subsumed. Afterwards, a summary of event generation to keep the overall picture of the simulated processes in mind will be given before moving on to describing a convenient way of phase space decomposition. At the end of this chapter, the anatomy of NLO subtraction and matching formalisms will be discussed.

2.1 Monte-Carlo methods

The idea of using random acts cleverly chosen to converge to a desired solution is not new. Already in the 18th century, Buffon proposed a way for the probabilistic determination of π by throwing needles on a striped floor. The methods have quite evolved since then. One of the most classic papers is [37], already proposing the use of "modern computing machines". Today, not only the speed of computers has increased, but also intricate mechanisms have been developed to enhance the convergence of Monte-Carlo integration, for example the VEGAS algorithm [38,39] or, as a more recent implementation, the ExSample library [40].

The simplest procedure works as follows. An estimation of the integral

$$I = \int_V f\left(\vec{x}\right) \mathrm{d}^n x \tag{2.1}$$

is achieved by evaluating f at N pseudo-random points $\vec{x}_i$ from a uniform probability distribution. In practice, the size of the integration volume V is unity, as the random numbers are picked from an n-dimensional hypercube of edge length

unity. The average

$$\bar{f} = \frac{V}{N} \sum_{i=1}^{N} f\left(\vec{x}_i\right) \tag{2.2}$$

converges against the true value of I like $1/\sqrt{N}$, independent of the integral dimensionality. This is the main advantage of Monte-Carlo integration over other numerical integration procedures such as the trapezoid rule or the Simpson rule, which converge slower in higher dimensions. If N is large enough, the error of the result can be estimated by the sample variance

$$\sigma_I = \sqrt{\mathrm{VAR}(f)} = \sqrt{\frac{1}{N-1} \sum_{i=1}^{N} f^2\left(\vec{x}_i\right) - \frac{N}{N-1} \bar{f}^2}. \tag{2.3}$$

This is a consequence from the central limit theorem, stating that the estimates (2.2) converge to a normal distribution around the true value I.

Monte-Carlo integration can be improved by using a non-flat probability distribution from which the random numbers are drawn. For sake of simplicity, we stick to a one-dimensional integral

$$\int f(x) \mathrm{d}x. \tag{2.4}$$

This can be rewritten by defining an analytically integrable function $g(x)$ which approximates $f(x)$,

$$\int \frac{f(x)}{g(x)} g(x) \mathrm{d}x = \int \frac{f(x)}{g(x)} \mathrm{d}y. \tag{2.5}$$

Now, the sampling can take place in terms of y and as $\frac{f(x)}{g(x)} \approx 1$, the variance of the integral is reduced.

For complicated functions, like for example a superposition of several peaks, the approach can be extended to a multi-channel integration. Here, the integral is rewritten in terms of a linear combination of integrable functions

$$\sum_i \alpha_i g_i(x), \tag{2.6}$$

each approximating the integral in distinct regions. Then, the integral can be split into several parts by

$$\int \frac{f(x)}{\sum_i \alpha_i g_i(x)} \sum_i \alpha_i g_i(x) \mathrm{d}x = \sum_i \alpha_i \int \frac{f(x)}{\sum_i \alpha_i g_i(x)} \mathrm{d}y_i. \tag{2.7}$$

The coefficients α_i need to be adapted with regard to the contributions of each integral to the total integral.

In order to improve the accuracy, one can rely on importance sampling, i.e. sampling points according to their contribution to the integral. To be independent of the exact shape of the function to be integrated, the probability distribution can be adapted in several steps. In the VEGAS algorithm, this happens by dividing the integration volume into several same sized hypercubes at the beginning. After the first iteration, the boundaries of the hypercubes are shifted, so that they become hypercuboids of different sizes. The number of sampled points per hypercuboid is approximately the same for each of them, so that the sampling densities rise in the smaller hypercuboids.

ExSample uses another approach. Being built to maximise the unweighting efficiency, the hypercubes are split instead of shifting their borders. After a certain number of events, the algorithm splits cells which fail to produce an unweighting efficiency below a user defined value. As such a splitting can happen along different axes, the axis k which is split is determined in a way to minimise the gain value

$$g_k(x_k) = \frac{\int_{x_k^-}^{x_k} \mathrm{d}x \langle f \rangle_k(x) - \int_{x_k}^{x_k^+} \mathrm{d}x \langle f \rangle_k(x)}{\int_{x_k^-}^{x_k^+} \mathrm{d}x \langle f \rangle_k(x)}, \tag{2.8}$$

where $x_k^\pm$ are the upper and lower boundaries of the cell. $\langle f \rangle_k(x)$ is the projection of the integrand on the axis k. For reasons of simplicity, the splitting point x_k is chosen to be in the middle of the cell,

$$x_k = \frac{x_k^+ - x_k^-}{2}. \tag{2.9}$$

2.2 Event generators

A large part of the work for the thesis at hand involved the calculation of NLO matched Higgs production. Therefore, an abstract of event generation is given in this section. Although the description is oriented closely at Herwig++, the event generator used in the main part of this study, differences to other generators, mainly PYTHIA [41], are emphasised wherever necessary. Special care will be taken to explain how jet algorithms work, which allow the reduction of a complex final state to few abstract objects. In an additional subsection, the legitimacy of parton shower algorithms is justified by an examination of the collinear and soft limits.

The general purpose of an event generator is to simulate the evolution from the hard scale of the perturbatively calculated matrix element down to the soft scale of stable and quasi-stable particles which can be measured in detectors. To achieve this, several steps can be distinguished, each corresponding to one realm of physics.

For the hard matrix element, the standard of precision is still the LO calculation, although many efforts are made to incorporate NLO matrix elements by matching or merging methods. NLO matching is understood as incorporating

higher order corrections of the hard matrix element consistently in a showered calculation and will be described in a more detailed way in Section 2.4.2. The term merging means employing matrix elements of varying jet multiplicity to improve the prediction of multi-jet observables. For LO matrix elements, the CKKW [42] method is widely used. The first conceptual paper of an extension to NLO was written almost a decade ago [43], followed by different suggestions of schemes [44–47].

In some sense parallel to the hard matrix element, additional hard and soft interactions may take place. At the LHC, the probability of having additional semi-hard scatterings is large because the PDFs are probed in a kinematic regime where even the subleading partonic content of the proton can initiate a perturbative process. Such additional collisions which, while hard, are still softer than the matrix element of interest, are called multiple partonic interactions (MPI). Both in Herwig++ and in PYTHIA, they are brought in as additional QCD $2 \to 2$ scatterings.

After the shower initiating partons are present, the evolution can take place. The final- and initial-state partons of the matrix element(s) are allowed to emit QCD radiation. The forward evolution of the final state partons is called final-state radiation (FSR). In contrast, the initial-state partons are evolved backwards by initial-state radiation (ISR) down to a hard scale where they can be assigned to the incoming hadrons. Within ISR, also final state particles are emitted, which act as initiators of FSR themselves.

Parton showers can differ in the choice of the evolution variable and splitting kernels. The only property that is fixed by QCD is the behaviour in the limit of soft and/or collinear emissions. This leaves a freedom in the parametrisation of splitting kernels away from that singular region. Herwig++ offers two different showers, which are compared in detail in this work. The default option is also based on DGLAP splitting kernels, but together with an evolution variable tied to the opening angle of emissions. The latest shower implementation is based on Catani-Seymour $2 \to 3$ dipole splitting kernels and is ordered in transverse momentum.

When the shower evolution has lowered the scales down to a lower cutoff value, which is typically chosen somewhere around 1 GeV, hadronisation kicks in. At low energies, perturbation theory breaks down. Here, lattice gauge theory allows predictions from first principles on a discretised spacetime. In collider phenomenology however, it is fortunately sufficient to employ simple phenomenological models to describe the transition from partonic to hadronic states. Two types of models are to be accentuated here: string models and cluster models.

String models are based on the picture that the field between colour charged particles forms a string-like object. The situation is sketched in Figure 2.1. Strings are allowed to break up into smaller pieces by popping additional particle antiparticle pairs out of the vacuum. These nonperturbatively produced particle pairs may consist of $q\bar{q}$ pairs or diquark pairs. Within so-called popcorn models, also the simultaneous production of two $q\bar{q}$ pairs in one step is introduced.

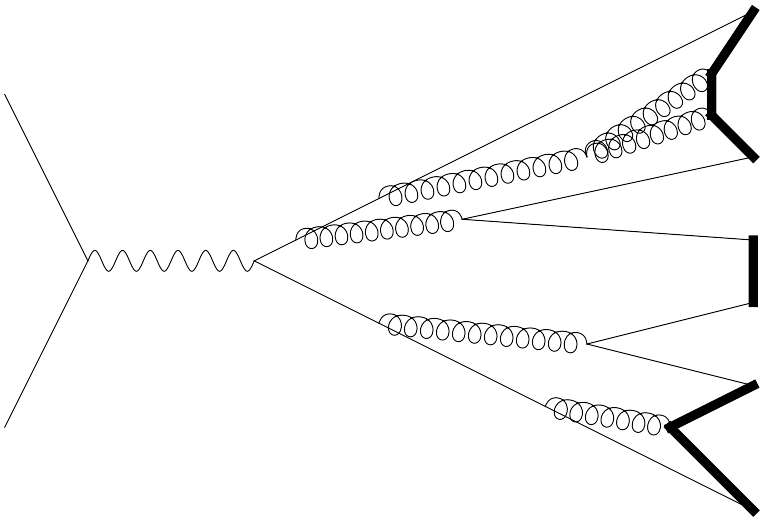

Figure 2.1: Sketch of string hadronisation models, from [22]. Colour connected partons form string-like objects, which are allowed to rip iteratively into smaller pieces.

After a cascade of ripping processes, the resulting substrings are converted into mesons and baryons based on their particle content. During the process, attached gluons lead to kinks in the string, which affect the hadronic angular distributions. Within PYTHIA, mostly the Lund string model is used, which is described in detail in [48].

Cluster models are not motivated by a picture of the strong force building flux tubes, but are based on a property of QCD that is known as colour preconfinement [49]: Quark lines carrying the same colour index form clusters with a universal mass distribution, peaked at low masses. The process is sketched in Figure 2.2.

In cluster models, gluons have to be split nonperturbatively into $q\bar{q}$ pairs before the recombination takes place. Then, colour-connected partons are joined to form clusters. These are assumed to be highly excited hadron states and are able to decay isotropically into the known hadrons in $1 \rightarrow 2$ processes. If a cluster mass is too high, it may need to undergo one or more intermediate decays into lighter clusters before it can be converted into hadrons. It may also occur that a cluster is too light to decay into two hadrons. In this case, it is converted directly into a single hadron.

The cluster model implemented in Herwig++ is described in [50]. In order to improve the model, colour reconnection can be imposed. That means the exchange of soft gluons before the cluster stage to minimise the invariant cluster mass, which improves the agreement with experimental data [51].

2.2.1 Jet algorithms

QCD radiation, which is simulated within parton showers, tends to produce high particle multiplicities in confined areas in the legoplot plane. Therefore, it is de-

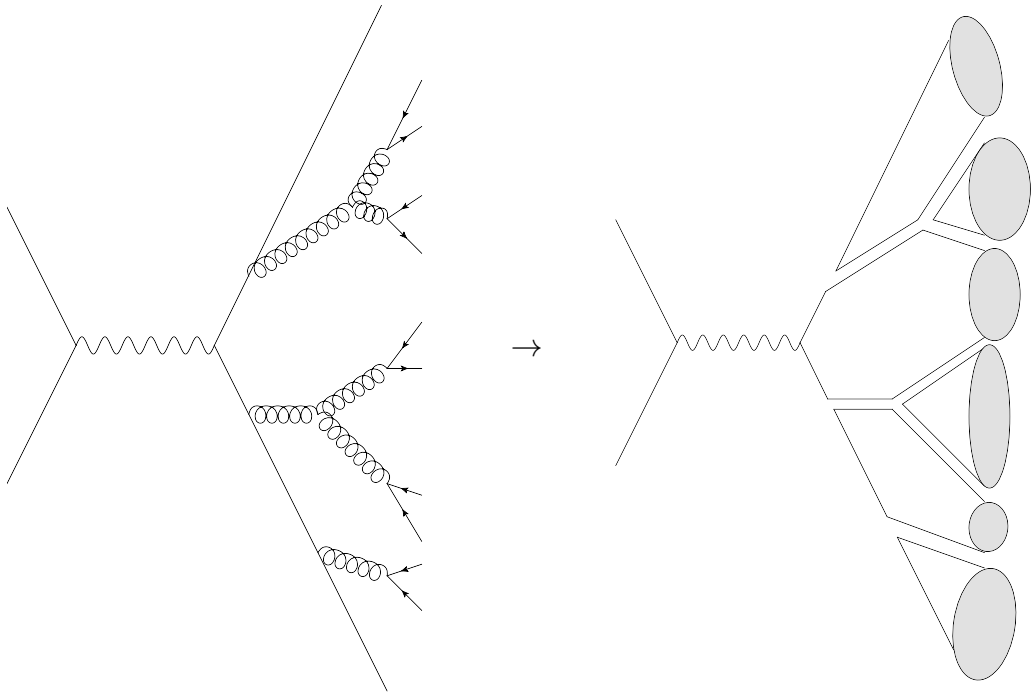

Figure 2.2: Hadronisation in cluster models. Gluons in the final state must undergo a nonperturbative splitting before the conversion to clusters may take place. The clusters are then decayed into the observed baryons and mesons.

sireable to reduce the information content of an event. To this end, jet algorithms are introduced. A meaningful comparison between theory and experiment can only be achieved after a suitable jet algorithm has been applied.

A basic requirement for the algorithm is to be infrared safe. The results are not allowed to change if an additional soft particle is radiated. The splitting of a particle into two collinear ones must also leave all jets invariant. The latter property is known as collinear safety.

Two types of jet algorithms must be distinguished: Cone algorithms and algorithms with sequential recombination. Cone algorithms try to define a jet as all particles within a circle in the legoplot plane, spanned by pseudorapidity η and azimuthal angle ϕ. The diameter of the circle is an input parameter of the algorithm while its centre is varied to find a position where it coincides with the barycentre of the circle, which can for example be defined using transverse energy weighted sums

$$\begin{aligned} \eta_{\mathrm{CM}}^{\mathrm{cone}} &= \sum_i \frac{E_T^i \eta_i}{E_T^{\mathrm{cone}}} \\ \phi_{\mathrm{CM}}^{\mathrm{cone}} &= \sum_i \frac{E_T^i \Phi_i}{E_T^{\mathrm{cone}}}. \end{aligned} \tag{2.10}$$

The index i runs over all particles within the circle area.

The problem with cone algorithms is that the simpler ones lack infrared or collinear safety as starting points need to be chosen from which stable cone positions are constructed iteratively. Existing exact, infrared and collinear safe cone algorithms capable of finding all stable cones, for example the one suggested in [52], need $\mathcal{O}(N2^N)$ steps to complete, where N is the number of particles to be considered. This is far too many to be utilised in hadron collisions. There exists an infrared and collinear safe algorithm needing only $\mathcal{O}(N^2 \ln N)$ steps, SISCone [53], which is only approximative in the sense that it may miss some stable cones.

The other type of jet algorithms are based on sequential recombination. Instead of trying to fit all the detected particles into predetermined shapes at once, they recombine them or remove them from the algorithm step by step until the final jets are found.

An inclusive sequential recombination jet algorithm reads as follows:

1. All distances d_{ij} between objects (particles or protojets, in case one or more recombinations took place already) i and j as well as the separations d_{iB} between i and the beam axis are calculated as

$$d_{ij} = \min(k_{T,i}^{2p}, k_{T,j}^{2p}) \frac{\Delta R_{ij}^2}{D_{\text{cone}}^2}, \qquad d_{iB} = k_{T,i}^{2p}, \tag{2.11}$$

   where ΔR_{ij} is the legoplot distance between i and j and $k_{T,i}$ is the transverse momentum of i. D_{cone} is a free parameter of the algorithm.

2. If the minimum of all d_{ij} and d_{iB} is a d_{ij}, then i and j are merged to a new object which replaces the original particles i and j from the algorithm. If the minimum distance is a d_{iB}, then i is identified as a final jet and also removed from the algorithm.

3. If there are any objects left, repeat from the first step.

The parameter p in (2.11) is usually chosen to be $p = 1, 0, -1$. The corresponding algorithms are called k_T- [54, 55], Cambridge/Aachen [56, 57] and anti-k_T-algorithm [58] respectively. The anti-k_T-algorithm is especially interesting, as the borders of its jets are resistant concerning additional soft emissions. The reconstructed jets show similar circular shapes in the legoplot plane as the ones that are reconstructed by cone algorithms. That behaviour shows up due to the $1/k_T^2$ proportionality in the separation definition, which forces soft emissions to recombine with hard ones first instead of with other soft emissions.

2.2.2 Parton showers

Although calculations within perturbative QCD usually give surprisingly predictive results, this is not true for all phase space regions. The emission of additional gluons in arbitrary QCD processes can lead to large logarithmic enhancements $\ln(\Lambda_{\text{hard}}/\Lambda_{\text{cutoff}})$, where $\Lambda_{\text{hard/cutoff}}$ are the scale of the hard process and the shower cutoff scale. The latter is usually chosen around 1 GeV, where the perturbative

expansion begins to break down. In the following, the basic principles of a parton shower algorithm based on Altarelli-Parisi splitting functions will be discussed in a very general way.

The starting point is the observation that upon emission of a gluon off an external line with momentum p and mass m, an additional propagator of the form

$$\frac{1}{(p \pm q)^2 - m^2} = \frac{\pm 1}{2\omega E(1 - v\cos\theta)}, \tag{2.12}$$

needs to be inserted. Here, q and ω denote the gluon momentum and energy while E and v are energy and velocity of the emitting parton. The propagator in (2.12) gives a large contribution if either the emitted gluon is soft ($\omega \to 0$) or the emitting parton is soft ($v \to 1$) and the additional gluon is emitted collinearly to it ($\theta \to 0$). The latter case will be discussed first.

In the limit of an additional collinear emission within an n parton process with differential cross section $\mathrm{d}\sigma_n$, the differential cross section factorises into [59]

$$\mathrm{d}\sigma_{n+1} = \mathrm{d}\sigma_n \frac{\mathrm{d}\tilde{q}^2}{\tilde{q}^2} \mathrm{d}z \frac{\alpha_S}{2\pi} P_{\tilde{ij}\to ij}(z), \tag{2.13}$$

which was already averaged over the azimuthal angle of the additional emission. The variable $\tilde{q}^2$ is the energy scale of the emission and z is the energy fraction the emission carries away. $P_{\tilde{ij}\to ij}(z)$ is the corresponding splitting function for the process and, for the case of massive partons, given by [7, 60]

$$\begin{aligned}
P_{\tilde{q}\to qg} &= \frac{C_F}{1-z}\left[1 + z^2 - \frac{2m_q^2}{z\tilde{q}^2}\right] \\
P_{\tilde{g}\to gg} &= C_A\left[\frac{z}{1-z} + \frac{1-z}{z} + z(1-z)\right] \\
P_{\tilde{g}\to q\bar{q}} &= T_R\left[1 - 2z(1-z) + \frac{2m_q^2}{z(1-z)\tilde{q}^2}\right].
\end{aligned} \tag{2.14}$$

These are the Altarelli-Parisi splitting kernels. There are other possible parametrisations of the QCD singularities which can also be used as shower kernels, for example within antenna showers [61] or of course in the dipole shower implemented in Herwig++ [62].

The collinear factorisation theorem (2.13) can be used to calculate more than one emission. In order to avoid collinear infinities, the shower cutoff scale Λ_{cutoff} is introduced and the probability of having no resolved emission, i.e. no emission above Λ_{cutoff}, within an interval $\mathrm{d}\tilde{q}^2$ is given by

$$1 - \sum_{i,j} \frac{\mathrm{d}\tilde{q}^2}{\tilde{q}^2} \mathrm{d}z \frac{\alpha_S}{2\pi} P_{\tilde{ij}\to ij}(z). \tag{2.15}$$

Making the transition to a finite continuous interval, the no-emission probability for each possible splitting exponentiates and gives rise to the corresponding Sudakov

form factor

$$\Delta_{\tilde{ij}\to ij}(\tilde{q}_a^2,\tilde{q}_b^2)=\exp\left[-\int_{\tilde{q}_a^2}^{\tilde{q}_b^2}\frac{\mathrm{d}\tilde{q}'^2}{\tilde{q}'^2}\int \mathrm{d}z\frac{\alpha_S}{2\pi}P_{\tilde{ij}\to ij}(z)\Theta(p_T^2)\right] \tag{2.16}$$

which is the probability of having no emission between the two scales $\tilde{q}_a^2$ and $\tilde{q}_b^2$. The additional Heaviside function comes into play to accommodate the proper phase space boundaries of the z integration.

So far, only the collinear limit was incorporated in the Sudakov form factor, but also in the soft limit, where the energy ω of the additional emission becomes small in (2.12), large contributions arise. In the soft limit, the factorisation theorem reads [59]

$$d\sigma_{n+1}=d\sigma_n\frac{d\omega}{\omega}\frac{d\Omega}{2\pi}\frac{\alpha_S}{2\pi}\sum_{i,j}C_{ij}W_{ij} \tag{2.17}$$

with Ω as the solid angle of the emission and a colour factor C_{ij}. W_{ij} is the antenna function

$$W_{ij}=\frac{E_g^2 p_i\cdot p_j}{(p_i\cdot q)(p_j\cdot q)}=\frac{1-v_iv_j\cos\theta_{ij}}{(1-v_i\cos\theta_{iq})(1-v_j\cos\theta_{jq})}. \tag{2.18}$$

Assuming both possible emitter lines i and j to be massless, this can be rewritten to yield

$$W_{ij}=W_{ij}^{[i]}+W_{ij}^{[j]} \tag{2.19}$$

by using the definition

$$W_{ij}^{[i]}=\frac{1}{2}\left(W_{ij}+\frac{1}{1-\cos\theta_{iq}}-\frac{1}{1-\cos\theta_{jq}}\right). \tag{2.20}$$

Integrating (2.20) over the azimuthal angle of the emission,

$$\int_0^{2\pi}\mathrm{d}\Phi_{iq}\,W_{ij}^{[i]}=\frac{1}{1-\cos\theta_{iq}}\cdot\Theta(\theta_{ij}-\theta_{iq}), \tag{2.21}$$

reveals that emissions are only allowed within a cone of opening angle θ_{ij}. Thus, additional soft emissions are restricted to successively smaller emission angles. This property of (2.21) is known as angular ordering and arises from destructive interference of soft gluons. The evolution scale choices of the Herwig++ default and dipole shower respect angular ordering.

So far, the very basics of event generation were sketched and some of its details, namely the need for jet algorithms and their realisation, were discussed. In the end, the need for an all-order expansion with a parton shower algorithm was reasoned. However, the scope of the current section was only introductory. A substantial part of this thesis at hand is devoted to the comparison of two different shower implementations. These are treated in Section 4 in more detail.

2.3 Phase space decomposition

As the integration of a field theoretical cross section does not immediately involve an integral over the random number space but an integral over the physical phase space, an appropriate mapping between the two is needed. Such a mapping should be chosen in a way to smoothen peaks in the integrated function. The best way is to approximate the antiderivative of the integrated function, as the substitution

$$y(x) = F(x) + \Delta(x), \tag{2.22}$$

where

$$\begin{aligned} F'(x) &= f(x), \\ \Delta'(x) &= \epsilon(x), \quad |\epsilon(x)| \ll f(x), \end{aligned} \tag{2.23}$$

in an integral

$$\int \mathrm{d}x f(x) = \int \mathrm{d}y \frac{1}{1+\epsilon(x)/f(x)} \approx \int \mathrm{d}y \left(1 - \frac{\epsilon(x)}{f(x)}\right) \tag{2.24}$$

lowers the variance of the integral. By this, the Monte Carlo error can be reduced drastically.

In quantum field theory, usually many diagrams contribute to a single process. The peak structure of the squared sum of those is governed by the propagators of the single diagrams, but can be altered by gauge cancellations. A good approximation to the real structure is to model the peak structure of each squared diagram separately and do a multi-channel phase space integration. The individual phase space mapping can be achieved with a sequential splitting algorithm.

As already mentioned in [63], a convenient phase space decomposition in terms of invariant masses is obtained as follows. Let

$$\mathrm{d}\Phi_n(p_a + p_b; p_1, \ldots, p_n) = (2\pi)^4 \delta^{(4)}\left(p_a + p_b - \sum_{i=1}^{n} p_i\right) \prod_{i=1}^{n} \frac{\mathrm{d}^4 p_i}{(2\pi)^4} \delta(p_i^2 - m_i^2)\Theta(p_i^0) \tag{2.25}$$

be the phase space of the kinematical process $p_a + p_b \to \sum_{i=1}^{n} p_i$. With the definitions

$$q_k = \sum_{j=1}^{k} p_j, \qquad M_k^2 = q_k^2, \tag{2.26}$$

the phase space can be rewritten by inserting unity

$$1 = \int \mathrm{d}M_{n-1}^2 \delta(q_{n-1}^2 - M_{n-1}^2)\Theta(q_{n-1}^0) \times \int \mathrm{d}^4 q_{n-1} \delta^{(4)}(p_a + p_b - q_{n-1} - p_n) \tag{2.27}$$

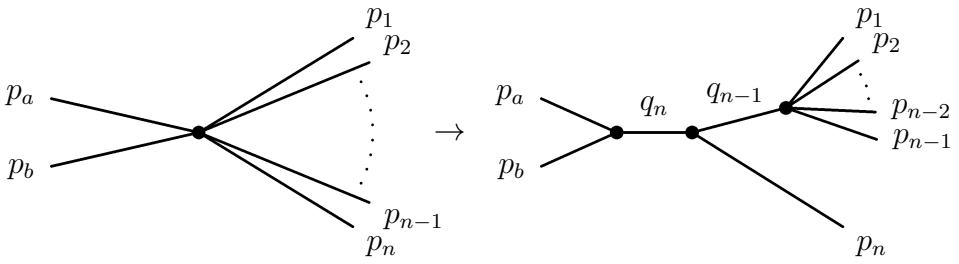

Figure 2.3: Recursive building of the phase space for s-channel splittings.

in (2.25). Note that each of the integrals in (2.27) separately reduces to unity by integration of the δ-distributions. The result can be expressed as

$$\begin{aligned}
&\mathrm{d}\Phi_n(p_a+p_b;p_1,\ldots,p_n)\\
&\quad=\int \mathrm{d}M_{n-1}^2 \int \mathrm{d}^4q_{n-1}\frac{\mathrm{d}^4p_n}{(2\pi^4)}\\
&\qquad\times\delta^{(4)}(p_a+p_b-q_{n-1}-p_n)\delta(q_{n-1}^2-M_{n-1}^2)\delta(p_n^2-M_n^2)\Theta(q_{n-1}^0)\Theta(p_n^0)\\
&\qquad\times(2\pi)^4\delta^{(4)}\left(q_{n-1}-\sum_{i=1}^{n-1}p_i\right)\prod_{i=1}^{n-1}\frac{\mathrm{d}^4p_i}{(2\pi)^4}\delta(p_i^2-M_i^2)\Theta(p_i^0)\\
&\quad=\int_{(\sum_{i=1}^{n-1}M_i)^2}^{(\sqrt{s}-M_n)^2}\mathrm{d}M_{n-1}^2\int \mathrm{d}\Phi_2(p_a+p_b;q_{n-1},p_n)\cdot\mathrm{d}\Phi_{n-1}(q_{n-1};p_1,\ldots,p_{n-1}) \quad (2.28)
\end{aligned}$$

which can be interpreted diagrammatically as seen in Figure 2.3. The upper and lower bounds of the integration range of M_{n-1}^2 can be deduced by the fact that it needs to be at least enough energy to generate the minimally allowed invariant masses downstream but not more than what is maximally available. In the centre-of-mass frame of the decaying virtual particle of momentum q_n, the generation of azimuthal and polar angles in the process $M_n \to p_n + M_{n-1}$ is trivial. The involved two-particle phase space can be written as

$$\begin{aligned}
\Phi_2(p_a+p_b;q_{n-1},p_n)&=\int\frac{|\vec{q}_{n-1}|\mathrm{d}|E_{n-1}|\mathrm{d}\Omega_{n-1}}{4\sqrt{s}}\delta\left(E_{n-1}-\frac{s+M_{n-1}^2-m_n^2}{2\sqrt{s}}\right)\\
&=\frac{\sqrt{\lambda\left(s,M_{n-1}^2,m_n^2\right)}}{8s}\int_0^{2\pi}\mathrm{d}\varphi_{n-1}\int_{-1}^{1}\mathrm{d}\cos\theta_{n-1}, \qquad (2.29)
\end{aligned}$$

with the Källén function

$$\lambda(x,y,z)=x^2+y^2+z^2-2xy-2yz-2zx. \qquad (2.30)$$

For a sequence of s-channel splittings, the propagator invariants can be generated consecutively by repeated application of (2.28). Recurrent boosts into the rest frame of the generated propagator are needed to map out the solid angle variables of the decomposition.

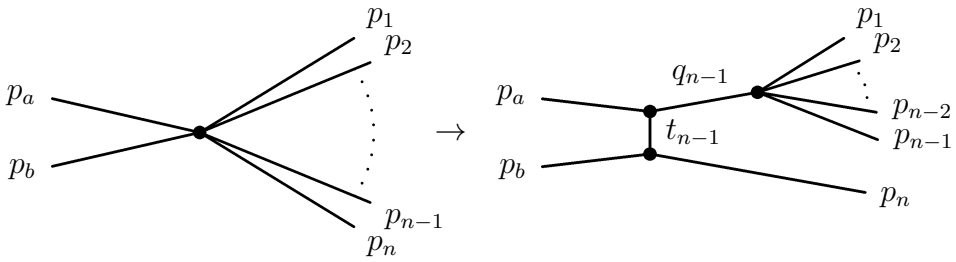

Figure 2.4: Recursive building of the phase space for t-channel splittings.

For t-channel splittings, the interpretation of (2.28) is not as straightforward because the calculation of the limits on the invariant is more involved. The polar angle is related to the Mandelstam variable,

$$t_{k-1} = (p_a - q_{k-1})^2 = m_a^2 + M_{k-1}^2 - 2E_a E_{k-1} + 2|\vec{p}_a||\vec{p}_{k-1}|\cos\theta_{k-1}. \tag{2.31}$$

Hence it is convenient to change the integration variable to

$$\mathrm{d}t = 2|\vec{p}_a||\vec{p}_{n-1}|\mathrm{d}\cos\theta_{n-1} \tag{2.32}$$

and (2.29) changes to

$$\Phi_2(p_a + p_b; q_{n-1}, p_n) = \frac{1}{8sp_a}\int_0^{2\pi}\mathrm{d}\varphi_{n-1}\int_{t_{n-1}^-}^{t_{n-1}^+}\mathrm{d}t_{n-1}, \tag{2.33}$$

where the limits on the t_{n-1}-integration as derived from (2.31) are given by

$$t_{n-1}^{\pm} = m_a^2 + M_{n-1}^2 - 2E_a E_{n-1} \pm 2|\vec{p}_a||\vec{p}_{n-1}|. \tag{2.34}$$

The diagrammatical interpretation of the splitting is sketched in Figure 2.4. For repeated mappings of t-channel propagators, boosts to the rest frame of the decaying virtual particles q_k are necessary just like in the case of s-channel splittings.

2.4 QCD at next-to-leading order

As mentioned in Section 1.3, QCD can be solved perturbatively if the energy scale of the process is sufficiently high, as the coupling constant is small then. However, it is still about a factor of 10 larger than the QED coupling constant. Therefore, higher order terms in QCD calculations are needed much earlier than in the QED case. As it is convenient to calculate cross sections and observable distributions by Monte-Carlo integration, a way of dealing with singularities, which naturally arise within higher order calculations, must be found. In the following, the formalism of dipole subtraction is described, which is also the tool of choice for the calculations that were done for the thesis at hand.

Subsequently, the problems that arise when applying a parton shower to an NLO calculation are discussed. These problems arise by double counting of terms that may either be generated by the NLO matrix element or by the shower expansion of the Born terms therein. Solutions of the problem involve either a modification of the expanded matrix elements or a modification of the first shower emission to keep the results after the shower correct to NLO.

2.4.1 Dipole subtraction

The general form of an NLO QCD cross section at a hadron collider reads

$$\sigma_{\mathrm{NLO}} = \sum_{a,b} \int_0^1 \mathrm{d}x_a f_a(x_a) \int_0^1 \mathrm{d}x_b f_b(x_b) \cdot \left[\int_m \mathrm{d}\sigma_B^{a,b} + \int_m \mathrm{d}\sigma_V^{a,b} + \int_{m+1} \mathrm{d}\sigma_R^{a,b} \right], \tag{2.35}$$

where the dependences on factorisation and renormalisation scales were dropped. a and b index the incoming partons with the parton distribution functions (PDFs) f_a and f_b giving their respective densities in the colliding hadrons. $\sigma_B^{a,b}$, $\sigma_V^{a,b}$ and $\sigma_R^{a,b}$ are the corresponding partonic Born, renormalised virtual and real-emission differential cross sections for the process $a + b \to X$. The number of final-state particles in the given process is given by m.

As the virtual differential cross section contains infrared divergencies which cancel against soft and collinear divergencies arising by integration of the real-emission contributions, the total cross section is finite at NLO [64, 65]. However, due to the complexity of the involved matrix elements and phase space integrals, usually the only way to get a result is to do a numerical calculation. As the phase space integrals typically exhibit a high dimensionality, Monte Carlo integration is the best solution here. Each integral has to be treated separately then, so the cancellation of singularities has to be done beforehand. Only after the analytical cancellation of divergencies, the different integrals are finite and can be treated by Monte-Carlo methods. A popular approach for such a subtraction scheme is the Catani-Seymour dipole subtraction [66].

The general procedure is to construct so-called dipole terms,

$$\mathrm{d}\sigma_A^{a,b} = \sum_{\mathrm{Dipoles}} \mathrm{d}\sigma_B^{a,b} \otimes \left(\mathrm{d}V_{\mathrm{Dipole}}^{a,b} + \mathrm{d}\tilde{V}_{\mathrm{Dipole}}^{a,b} \right) \tag{2.36}$$

that feature the same singularity structure as the real-emission matrix element within their process-independent parts $\mathrm{d}V_{\mathrm{Dipole}}$ and $\mathrm{d}\tilde{V}_{\mathrm{Dipole}}^{a,b}$. The $\mathrm{d}\tilde{V}_{\mathrm{Dipole}}^{a,b}$ terms are remnants of the cancellation of singularities that arise from emissions collinear to one of the initial-state hadrons. The $\mathrm{d}V_{\mathrm{Dipole}}$ terms actually cancel singularities themselves. The process-independent parts of the subtraction terms can be analytically integrated over a one-parton phase space once and for all. The symbol $\otimes$

denotes that there is no true factorisation, but rather a convolution of colour and spin correlated matrix elements with dipole terms.

The dipole terms are inserted into (2.35) by adding and subtracting them. Rearranging and factorising out initial-state collinear singularities into the PDFs results in

$$\begin{aligned}\sigma_{\mathrm{NLO}} = &\sum_{a,b}\int_0^1 \mathrm{d}x_a f_a(x_a)\int_0^1 \mathrm{d}x_b f(x_b)\int_m \mathrm{d}\sigma_B^{a,b}\\ &+\sum_{a,b}\int_0^1 \mathrm{d}x_a \tilde{f}_a(x_a)\int_0^1 \mathrm{d}x_b \tilde{f}(x_b)\\ &\cdot\left[\int_m\left[\mathrm{d}\sigma_V^{a,b}+\mathrm{d}\sigma_B^{a,b}\otimes\mathcal{I}\right]+\int\mathrm{d}x\int_m\left[\mathrm{d}\sigma_B^{a,b}\otimes(\mathcal{P}(x)+\mathcal{K}(x))\right]\right.\\ &\left.+\int_{m+1}\left[\mathrm{d}\sigma_R^{a,b}-\sum_{\mathrm{Dipoles}}\mathrm{d}\sigma_B^{a,b}\otimes\left(\mathrm{d}V_{\mathrm{Dipole}}^{a,b}+\mathrm{d}\tilde{V}_{\mathrm{Dipole}}^{a,b}\right)\right]\right],\end{aligned}\tag{2.37}$$

where each integral is rendered separately finite by construction of the subtraction terms. The finite collinear remainder containing the $\mathcal{P}$ and $\mathcal{K}$ insertion operators arises as a relic of the absorption of the singularities stemming from emissions collinear to the incoming hadrons.

2.4.2 NLO matching

When running a parton shower with the Sudakov form factor

$$\begin{aligned}\Delta_\xi(q_0,q_1) &= \exp\left\{-\int_{q_0^2}^{q_1^2}\frac{\mathrm{d}q'^2}{q'^2}\int\mathrm{d}z\frac{\alpha_S}{2\pi}P_\xi(z,q')\right\}\\ &\approx 1-\int_{q_0^2}^{q_1^2}\frac{\mathrm{d}q'^2}{q'^2}\int\mathrm{d}z\frac{\alpha_S}{2\pi}P_\xi(z,q')\end{aligned}\tag{2.38}$$

on a Born configuration, higher order terms arise. The index ξ numbers the possible splitting functions P_ξ. When requiring at most one additional splitting, the situation after the shower can be calculated by summing the probabilities of either none or exactly one additional splitting, folded with the differential Born cross

section. The observable after the parton shower then takes the form

$$\begin{aligned}\langle O\rangle_{PS} = &\sum_{a,b}\int_0^1 \mathrm{d}x_a f_a(x_a)\int_0^1 \mathrm{d}x_b f(x_b)\\ &\cdot\left[\int_m \mathrm{d}\sigma_B^{a,b} F_O^{(m)}\Delta_\xi(q_c,q_{max})\right.\\ &\left.+\int_m \mathrm{d}\sigma_B^{a,b}\int_{q_c^2}^{q_{max}^2}\frac{\mathrm{d}q'^2}{q'^2}\int \mathrm{d}z F_O^{(m+1)}\frac{\alpha_S}{2\pi}P_\xi(z,q)\Delta_\xi(q,q_{max})\right]\\ \approx &\sum_{a,b}\int_0^1 \mathrm{d}x_a f_a(x_a)\int_0^1 \mathrm{d}x_b f(x_b)\\ &\cdot\left[\int_m \mathrm{d}\sigma_B^{a,b} F_O^{(m)}\left\{1-\int_{q^2>q_c^2}\mathrm{d}P_\xi\right\}+\int_m \mathrm{d}\sigma_B^{a,b}\int_{q^2>q_c^2}\mathrm{d}P_\xi F_O^{(m+1)}\right]. \end{aligned}\tag{2.39}$$

Here, $F_O^{(m)}$ is the jet-defining function for an m parton configuration. q_c^2 and q_{max}^2 give the lower cutoff scale and the maximal allowed scale of the shower respectively. The term in the second line of (2.39) is responsible for the probability to have no branching at all while the term in the third line gives the probability to have one splitting at a scale between q_c^2 and q_{max}^2 and none above. The last line introduces the notation

$$\int_{q^2>q_c^2}\mathrm{d}P_\xi = \int_{q_c^2}^{q_{max}^2}\frac{\mathrm{d}q'^2}{q'^2}\int \mathrm{d}z\frac{\alpha_S}{2\pi}P_\xi(z,q'). \tag{2.40}$$

These higher-order terms in (2.39) are the leading logarithmic approximation of the NLO matrix elements by the parton shower. When naively acting with a parton shower on an NLO matrix element, these approximations would be double counted. Knowing the expansion of the shower's Sudakov form factor, however, the additional terms can be subtracted from the NLO matrix element before showering,

$$\begin{aligned}\langle O\rangle_{\mathrm{MC@NLO}} = &\int_m F_O^{(m)}\left[\mathrm{d}\sigma_B^{a,b}+\mathrm{d}\sigma_V^{a,b}+\mathrm{d}\sigma_B^{a,b}\otimes\mathcal{I}\right]\\ &+\int\mathrm{d}x\int_m F_O^{(m)}\left[\mathrm{d}\sigma_B^{a,b}\otimes(\mathcal{P}(x)+\mathcal{K}(x))\right]\\ &+\int_m F_O^{(m)}\left[\mathrm{d}\sigma_B^{a,b}\int_1\mathrm{d}P_\xi-\sum_{\mathrm{Dipoles}}\int_1\sigma_B^{a,b}\otimes\left(\mathrm{d}V_{\mathrm{Dipole}}^{a,b}+\mathrm{d}\tilde{V}_{\mathrm{Dipole}}^{a,b}\right)\right]\\ &+\int_{m+1}F_O^{(m+1)}\left[\mathrm{d}\sigma_R^{a,b}-\mathrm{d}\sigma_B^{a,b}\mathrm{d}P_\xi\right]. \end{aligned}\tag{2.41}$$

Equation (2.41) was derived in [3] under the name of MC@NLO matching. After exponentiation with a parton shower and expansion in the strong coupling constant, it reproduces the correct NLO cross section. It is also important to

note that by construction, terms with m particle configurations and terms with $m+1$ particle configurations carry separately finite weights, so that in a practical implementation, they can be treated separately. Further, we have neglected terms of the form

$$\int \mathrm{d}\sigma_B^{a,b} \int_0^{q_c} \mathrm{d}P_\xi \left[F_O^m - F_O^{m+1}\right], \tag{2.42}$$

which are only power corrections vanishing for a sufficiently small shower cutoff scale q_c.

The MC@NLO matching scheme has two possible drawbacks, one being the fact that there is a small fraction of events with a negative weight as the integrands of (2.41) are not necessarily positive definite. In practice, this does not pose a problem as the only drawback with respect to a positive definite integrand is a larger runtime for the Monte Carlo integration to get to the same level of precision.

The other, more severe drawback is, that the subtraction terms derived from (2.39) depend on the Sudakov form factor of the parton shower. Hence, the procedure has to be adapted to a certain shower evolution. On the other hand, this can also be used to simplify the structure of the calculation substantially. By employing the same splitting functions in the Sudakov form factor as in the NLO subtraction scheme, the second to last line of (2.41) vanishes and only

$$\begin{aligned}\langle O\rangle_{\text{MC@NLO}}^{\text{dipPS}} &= \int_m F_O^{(m)} \left[\mathrm{d}\sigma_B^{a,b} + \mathrm{d}\sigma_V^{a,b} + \mathrm{d}\sigma_B^{a,b} \otimes \mathcal{I} + \int \mathrm{d}x\, \mathrm{d}\sigma_B^{a,b} \otimes (\mathcal{P}(x) + \mathcal{K}(x))\right] \\ &\quad + \int_{m+1} F_O^{(m+1)} \left[\mathrm{d}\sigma_R^{a,b} - \mathrm{d}\sigma_B^{a,b}\mathrm{d}P_\xi\right] \\ &= \int_m F_O^{(m)} \mathrm{d}\sigma_{\mathbb{S}}^{a,b} + \int_{m+1} F_O^{(m+1)} \mathrm{d}\sigma_{\mathbb{H}}^{a,b}\end{aligned} \tag{2.43}$$

remains. A shower achieving this simplification, based on Catani-Seymour dipole splittings, was implemented into Herwig++ and publicly released recently [62]. Equation (2.43) consists of two terms that enter the shower separately: Soft events $\mathrm{d}\sigma_{\mathbb{S}}^{a,b}$, based on a Born-like m-parton configuration and hard events $\mathrm{d}\sigma_{\mathbb{H}}^{a,b}$, where the shower starts from a real-emission configuration with $m+1$ partons.

Going back to (2.41), another toehold for its simplification can be found within its last line. Dropping this contribution can be achieved by using a Sudakov form factor for the first shower emission that mimics the exact real-emission contribution so that

$$\mathrm{d}\sigma_B^{a,b} \int_1 \mathrm{d}P_\xi = \mathrm{d}\sigma_R^{a,b}. \tag{2.44}$$

This matching scheme is known as POsitive Weight Hard Emission Generator (POWHEG) [4, 5]. The parton shower evolution is then piled upon parton-level

events with born kinematics only, having the weight of the $\bar{B}$ function, which consists of Born, virtual and integrated subtracted real-emission contributions,

$$\begin{aligned}\langle O\rangle_{\text{POWHEG}} = \int_m F_O^{(m)} \Bigg[&\mathrm{d}\sigma_B^{a,b} + \mathrm{d}\sigma_V^{a,b} + \mathrm{d}\sigma_B^{a,b} \otimes \mathcal{I} + \int \mathrm{d}x\, \mathrm{d}\sigma_B^{a,b} \otimes (\mathcal{P}(x) + \mathcal{K}(x)) \\ &+ \mathrm{d}\sigma_R^{a,b} - \sum_{\text{Dipoles}} \int_1 \sigma_B^{a,b} \otimes \left(\mathrm{d}V_{\text{Dipole}}^{a,b} + \mathrm{d}\tilde{V}_{\text{Dipole}}^{a,b} \right) \Bigg] \\ = \int_m F_O^{(m)} \bar{B}^{a,b} &\mathrm{d}\Phi_m. \end{aligned} \tag{2.45}$$

The hardest emission is handled by a Sudakov form factor which depends explicitly on the exact squared real emission and Born matrix elements $R\left(\Phi_m, \Phi_X\right)$ and $B\left(\Phi_m\right)$

$$\Delta_{\text{NLO}}(p_\perp) = \exp\left[- \int_1 \mathrm{d}\Phi_X \frac{R\left(\Phi_m, \Phi_X\right)}{B\left(\Phi_m\right)} \theta\left(p_\perp^X - p_\perp\right) \right], \tag{2.46}$$

where X is the additional emission.

The POWHEG matching scheme works very well with a $p_\perp$-ordered shower. With an angular ordered shower however, some peculiarities have to be minded, as the POWHEG NLO emission does not respect the angular ordering. In order to produce soft emissions at a larger emission angle as the POWHEG emission, a so called truncated shower needs to be employed.

Afterwards, the hardest emission is generated using the Sudakov of (2.46), before further partons can be emitted. To ensure that the POWHEG emission is indeed the hardest one, emissions that produce a higher transverse momentum are vetoed, i.e. if such an emission occurs, it is rejected.

In Herwig++, such a situation arises when employing the default shower. The shower evolution then splits into three parts:

1. Truncated shower: Soft and wide-angle emissions
2. POWHEG emissions with the hardest transverse momentum of all branchings
3. Vetoed shower: Further evolution with smaller angles and lower transverse momenta

The dipole shower, which takes transverse momentum as its evolution variable, does not need to be split into different regimes. The first emission is just replaced with the POWHEG emission and further evolution follows the Sudakov form factor of the dipole shower.

Both matching schemes, MC@NLO and POWHEG, recover the correct behaviour up to NLO after expansion with the parton shower. Also, both schemes generate the correct leading logarithms. Beyond that, they differ. Therefore, a substantial part of this thesis is to compare the predictions obtained by the two approaches within the same setup in order to gain information on the size of these differences which can be considered systematic uncertainties.

Summary of part I

The first part of this thesis gives an introduction to the basic principles and methods that are used later on. The field theoretical background is established by illustrating electroweak symmetry breaking and QCD. Both are substantial parts of the SM, the best confirmed theory of particle interactions known to date.

It is explained that due to QCD being a non-abelian gauge theory, which results in charged gauge bosons, properties as asymptotic freedom and confinement arise. Although not being able to treat soft physics within perturbation theory in the strong coupling constant, the perturbative results at high energy scales are predictive. The DGLAP evolution allows for the factorisation of soft physics in the initial state into experimentally measurable quantities, the PDFs.

Additional radiations, which cannot be treated in the Feynman diagram approach, can not be neglected completely. Large logarithms arise in the all-order expansion by soft and/or collinear divergencies. In this limit, a parton shower approach should be followed to improve the results.

NLO terms can be numerically calculated by Monte-Carlo methods with the help of an NLO subtraction scheme such as Catani-Seymour dipole subtraction. However, they are also approximated by a parton shower and a Born matrix element. This leads to the problem of double counting when trying to operate a shower on an NLO matrix element. Two solutions are discussed: The MC@NLO scheme, where the double counted terms are explicitly subtracted before showering and the POWHEG scheme, which uses a special Sudakov form factor for the hardest emission. This POWHEG-Sudakov incorporates the exact real emission matrix element.

For a calculation beyond leading order, jet algorithms need to be employed. They also allow to compare experimental and theoretical results by reducing the complexity of a high multiplicity final state to few theoretically well-defined objects. Care has to be taken within the construction of a jet algorithm to ensure collinear and infrared safety.

After having established an understanding of the basics of high energy physics in the current part, the next part of the thesis shows the application within the calculation of $H\gamma jj$ production at NLO QCD.

Part II

Higgs plus photon production at NLO

Chapter 3

Higgs boson production in association with a photon via vector boson fusion

The recent discovery of a Higgs boson candidate is a milestone in high energy physics. To achieve certainty that it is the Higgs boson predicted by the SM, all its couplings have to be measured and compared with theoretical predictions. The experimental determination of the $Hb\bar{b}$ Yukawa coupling is a difficult task, as the signal channel is spoiled by QCD backgrounds with high cross sections. There were several proposals of new analysis methods to cope with these challenging problems. Exploring the jet substructure in "fat-jets" [67, 68] can help improving the signal-to-background ratio. Another possibility arises by requiring the presence of an additional W boson in Higgs production via vector boson fusion [69, 70], which is unfortunately also leading to a decreasing cross section. To some extent, this can be prevented by requiring an additional photon instead of a W boson.

The bulk of the backgrounds to the $H \to b\bar{b}$ decay channel are composed of gluonic components (see Figure 3.1). Due to the nonexistence of a gluon-photon coupling in the Standard Model, the requirement of an extra photon leads to a drastic suppression of the QCD backgrounds. The mechanism works in an opposite way than applying a central jet veto: Instead of forbidding the typical additional radiation of the background process, the signal is required to show central photon radiation, which is uncommon for the expected backgrounds.

In addition to coupling effects, there is also a destructive interference in quark scattering by a neutral gauge boson in the t-channel of diagrams where photons are emitted from incoming and outgoing fermion lines, respectively. This effect not only arises in QCD background processes, but also in the ZZ fusion signal process. Thereby, not only the relevant background processes are suppressed, but also the ZZ fusion component of the signal channel. WW fusion is unaffected by the interference, so it experiences a relative enhancement.

In [71], a detailed signal and background analysis at leading order was presented. The work was done using the automated tools ALPGEN [72] and MadE-

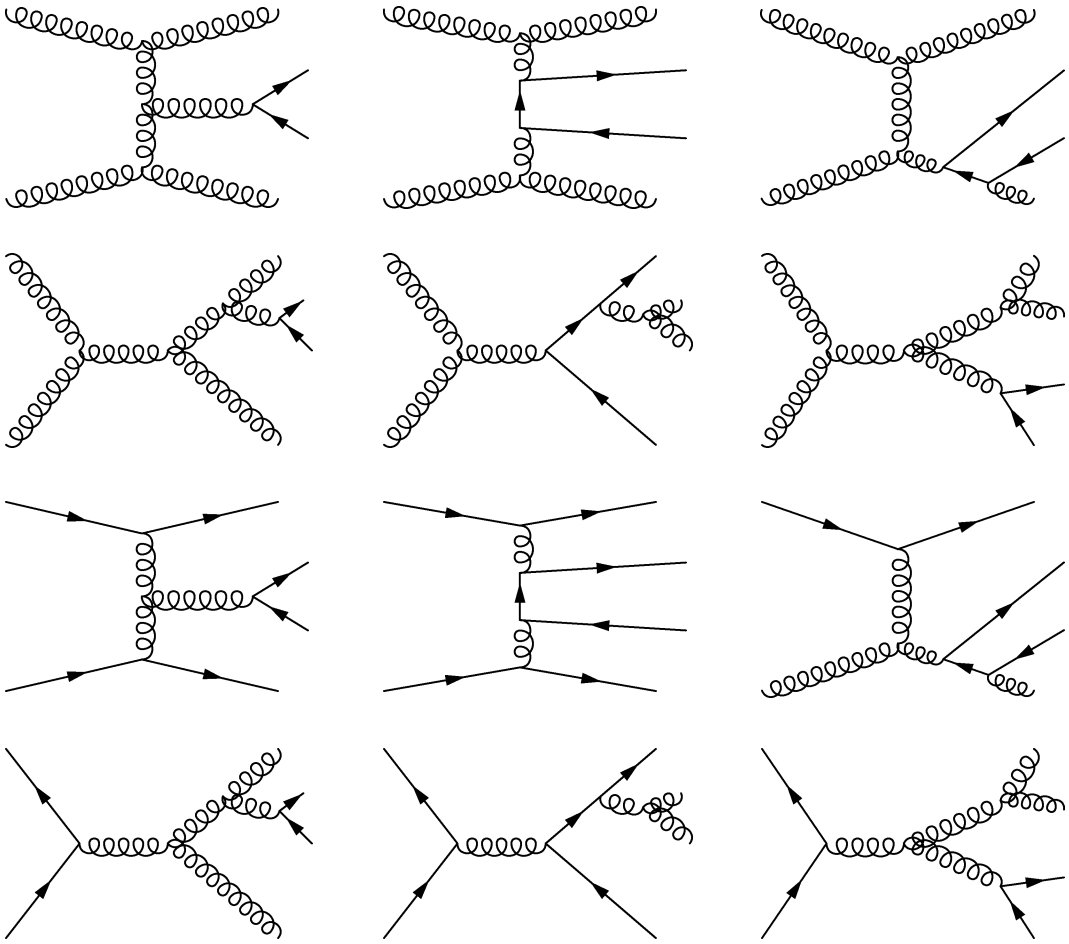

Figure 3.1: Some of the relevant Feynman diagrams of the QCD background to $H \to b\bar{b}$. Gluonic components compose a large part of the cross section.

vent [73]. The authors found that the additional photon requirement reduces the signal by a factor of approximately 1/100 whereas the background is reduced by a factor of 1/3000. The resulting statistical significances $S/\sqrt{B}$ are somewhere between 2 and 3 for a 14 TeV collider with an integrated luminosity of 100/fb. It was also mentioned that the additional photon can improve the experimental triggering. Additional selection cuts were proposed on the invariant mass of the $b\bar{b}\gamma$ system.

A later parton shower study [74] of signals and backgrounds using ALPGEN followed by a full PYTHIA [41] event generation could confirm the results for realistic final states. They used different cuts than [71], resulting in a slightly lower significance of $1 \lesssim S/\sqrt{B} \lesssim 2$.

For a precise prediction and reliable estimates of theoretical uncertainties, an LO calculation is not sufficient. In order to improve the prediction, a next-to-leading order calculation has been performed in this work. Three independent implementations of the whole process were developed by the authors of [75,76]. The implementation of the author of the thesis at hand is based on HELAS subroutines [77] and was proven to be the fastest one, therefore this calculation was chosen to be published as part of the parton-level Monte-Carlo program VBFNLO [6].

3.1 Elements of the calculation

3.1.1 Approximations

To minimise computing time, several approximations have been used which have proven their validity already within other VBF-type processes. As the most interesting phase space regions are those where the two tagging jets are widely separated in rapidity, the VBFNLO implementation neglects interference terms between t- and u-channel diagrams, which are present for identical quark flavours only. This is known as "VBF approximation". It was shown that these disregarded contributions are small in the relevant regions for Higgs searches in the VBF channel [29].

In addition, diagrams with annihilation processes $q\bar{q} \to ZH\gamma$ and a subsequent decay $Z \to q\bar{q}$ are neglected. In the calculation, all fermion masses are set to zero. The $H\gamma jj$ production process is simulated separately and then combined with a subsequent decay of the Higgs boson into two generic fermions. In the results which are shown in Section 3.3, the branching ratio is set to unity, i.e. all decay channels are summed up. Contributions with external bottom or top quarks in the initial state are neglected and the Cabibbo-Kobayashi-Maskawa matrix is approximated by the identity matrix.

3.1.2 Real and virtual corrections

Due to colour conservation, virtual contributions where a gluon connects the two incoming fermion lines vanish within the VBF approximation. The only loop corrections that contribute are composed of self-energies, triangle and box diagrams

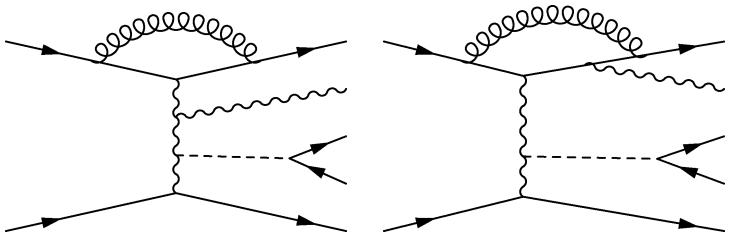

Figure 3.2: Representative Feynman diagrams of virtual corrections to $H\gamma jj$ production. The graph type with the triple gauge boson vertex on the left is only possible for t-channel exchange of Z bosons and receives only the shown vertex correction. The other graph applies to both W and Z boson exchange and features self-energy, vertex and the shown box loop correction.

with an additional gluon attached to a single quark line. Two of the relevant diagrams which give corrections to the upper quark line are shown in Figure 3.2. The combination of all virtual corrections to quark line i can be cast into the general form of the virtual amplitude

$$\mathcal{M}_V^i = \mathcal{M}_B \frac{\alpha_s(\mu_R)}{2\pi} C_F \left(\frac{4\pi\mu_R^2}{Q_i^2}\right)^{\epsilon} \Gamma(1+\epsilon) \left(-\frac{2}{\epsilon^2} - \frac{3}{\epsilon} + c_{\text{virt}}\right) + \tilde{\mathcal{M}}_V^i \,, \qquad (3.1)$$

where $C_F = 4/3$ and $c_{\text{virt}} = \pi^2/3 - 7$ in dimensional reduction ($c_{\text{virt}} = \pi^2/3 - 8$ in conventional dimensional regularisation). Q_i is related to the momentum transfer from the initial-state fermion with momentum p_{in}^i to the final state fermion with momentum p_{fi}^i by $Q_i^2 = -(p_{\text{in}}^i - p_{\text{fi}}^i)^2$.

The finite amplitudes $\tilde{\mathcal{M}}_V^i$ are evaluated by the help of Passarino-Veltman tensor reduction [78]. A detailed description of the loop calculations and subroutines that are used for the publicly available version of this process can be found in [79].

For a small number of phase space points, numerical instabilities occur. These arise because of small Gram determinants in the Passarino-Veltman reduction formalism. To prevent them from spoiling the convergence of the integration, a gauge check has been introduced: The virtual amplitudes have to fulfil Ward identities at every phase space point up to a user defined precision. If a phase space point violates the Ward identities, the virtual contributions $\tilde{\mathcal{M}}_V^i$ from this point are removed. It was checked that the fraction of phase space points that do not fulfil the gauge check with a relative accuracy of at least 10^{-3} is less than 0.1 permille. By varying the required accuracy, it was checked that the numerical error due to removing these contributions is small.

The real-emission diagrams are obtained by insertions of a gluon at all possible points in the LO diagrams. Also, new channels with gluons in the initial state have to be considered. They are crossing-related to the ones with a gluon in the final state. The Catani-Seymour subtraction formalism, described in Section 2.4.1, was employed to combine them with the virtual corrections. The integrated

counterterm in form of the insertion operator is given by

$$\langle \mathcal{I}(\epsilon) \rangle = |\mathcal{M}_B|^2 \frac{\alpha_s(\mu_R)}{2\pi} \left(\frac{4\pi\mu_R^2}{Q_i^2} \right)^2 \Gamma(1+\epsilon) \left[\frac{2}{\epsilon^2} + \frac{3}{\epsilon} + 9 - \frac{4}{3}\pi^2 \right]. \tag{3.2}$$

3.1.3 Checks

The building blocks of the calculation have been tested thoroughly. The three independent implementations, which were developed by the authors of [75, 76], were compared both at the amplitude level and at the level of integrated cross sections. The individual amplitudes agreed perfectly and the cross sections were consistent within the achieved statistical uncertainties at the sub-permille level.

A cross check of the amplitudes against MadGraph [80] at a randomly drawn set of phase space points has shown agreement to about 12 digits. Integrated LO cross sections were also compared to results from MadEvent [73, 81] and showed agreement within the accuracies of the two programs.

QED gauge invariance of the leading-order, real-emission and virtual contributions was tested by replacing the photon polarisation vector with its momentum and checking that the resulting contributions vanish. The same method was utilised to check the QCD gauge invariance of the real-emission contributions by replacing the gluon polarisation vector with its momentum.

3.2 Parameters and cuts

A value of 126 GeV for the Higgs mass is chosen in the following. Before the discovery of a new resonance at the LHC, results for $H\gamma jj$ production were published in [75, 76] for a Higgs mass of 120 GeV. The setup used within the following generally keeps the other parameters that were used in these two publications fixed, but they are reviewed here for completeness.

As the determination of the $Hb\bar{b}$ Yukawa coupling is a long-term goal in the LHC experimental program, we assume a hadronic centre-of-mass energy of $\sqrt{S} = 14\,\text{TeV}$ in the following analysis. The masses of the electroweak gauge bosons are chosen as $m_W = 80.398\,\text{GeV}$ and $m_Z = 91.188\,\text{GeV}$ and the Fermi constant is $G_F = 1.166 \times 10^{-5}/\,\text{GeV}$. These parameters allow for the calculation of the electroweak coupling constant α_{QED} and the sine of the Weinberg angle $\sin\theta_W$ with the help of LO electroweak relations.

The CTEQ6L1 PDF set [82] at LO and the CTEQ10 PDFs [83] at NLO are used as defaults unless stated otherwise. To approximate the error of the PDF choice, results with the MSTW2008 PDFs [84] are also shown.

The k_T jet algorithm [54, 55, 85] in the form as described in [52] with a cone parameter of $D = 0.7$ is used to reconstruct jets from final state partons with rapidities $|y_p| \leq 5$. The E-scheme is used to recombine the partonic momenta, which means that the jet momentum is just the sum of the four momenta of its

constituents. At least two outgoing jets are required with

$$p_{Tj} > 20\,\text{GeV}, \qquad |y_j| \leq 5, \tag{3.3}$$

where p_{Tj} and $|y_j|$ denote transverse momentum and rapidity of the recombined jet. The jets are numbered by their ordering in transverse momentum and the two jets with the largest p_T will be referred to as tagging jets.

The Frixione isolation criterion [86] is used to avoid collinear singularities of the photon with other final-state particles. The naive solution of cutting away all emissions close to the photon would spoil the convergence behaviour of the Catani-Seymour subtraction formalism as the correct cancellation of infrared singularities needs real-emission contributions within the whole phase space. Frixione suggested to only allow events if the energy deposited in a cone around the photon is lower than

$$\sum_{i:\Delta R_{i\gamma}<\Delta R} p_{Ti} \leq \frac{1-\cos\Delta R}{1-\cos\delta_0} p_{T\gamma} \qquad \forall \Delta R \leq \delta_0. \tag{3.4}$$

The index i sums over all final-state partons found within a legoplot distance of ΔR around the photon. p_{Ti} denotes the transverse momentum, and $\Delta R_{i\gamma}$ the separation of parton i from the photon. δ_0 stands for a fixed separation and is a free parameter of the cut. The parameter takes the value

$$\delta_0 = 0.7 \tag{3.5}$$

throughout the analysis presented here.

As already mentioned before, the branching ratio of the Higgs decay to $b\bar{b}$ is not included in the results presented here. However, the general impact of the Higgs decay products, labelled d in the following, on phase space cuts is accounted for. We require the photon and the Higgs decay products, which are generated by an isotropic decay, to be central and to have sufficiently large transverse momenta,

$$\begin{aligned} |y_\gamma| &< 2.5, & |y_d| &< 2.5, \\ p_{T,\gamma} &> 20\,\text{GeV}, & p_{T,d} &> 20\,\text{GeV}. \end{aligned} \tag{3.6}$$

In the inclusive-cuts scenario, the two tagging jets must fulfil the requirement of a small minimum invariant mass,

$$m_{jj}^{\text{tag}} > 100\,\text{GeV}, \tag{3.7}$$

and all particles and jets have to be separated by

$$\Delta R_{dd} > 0.4, \qquad \Delta R_{d\gamma} > 0.4, \qquad \Delta R_{jd} > 0.4, \qquad \Delta R_{j\gamma} > 0.4. \tag{3.8}$$

A different set of more stringent cuts is applied within the VBF cuts scenario. Here, a larger invariant mass of the tagging jets is required,

$$m_{jj}^{\text{tag}} > 600\,\text{GeV}, \tag{3.9}$$

as well as larger separations of the particles

$$\Delta R_{dd} > 0.7, \qquad \Delta R_{d\gamma} > 0.7, \qquad \Delta R_{jd} > 0.7, \qquad \Delta R_{j\gamma} > 0.7. \tag{3.10}$$

As the analysis aims at decays into b-quarks, the separation of the decay particles was increased to improve the tagging. In addition, the two tagging jets are required to be well separated in rapidity,

$$|y_{j1} - y_{j2}| > 4, \tag{3.11}$$

and to be emitted into different detector hemispheres,

$$y_{j1} y_{j2} < 0. \tag{3.12}$$

Within the VBF cuts, the Higgs decay products and the photon need to be located in the rapidity gap between the tagging jets,

$$\begin{aligned} \min(y_{j1}, y_{j2}) \leq & y_d \leq \max(y_{j1}, y_{j2}) \\ \min(y_{j1}, y_{j2}) \leq & y_\gamma \leq \max(y_{j1}, y_{j2}). \end{aligned} \tag{3.13}$$

3.3 Results

The factorisation scale μ_F and the renormalisation scale μ_R were varied in order to estimate the dependence of the results on these unphysical scales. This can be seen as an estimate for the size of higher order corrections. The factorisation and renormalisation scales depend on a basic scale parameter μ_0,

$$\mu_F = \xi_F \mu_0, \qquad \mu_R = \xi_R \mu_0. \tag{3.14}$$

ξ_F and ξ_R are called factorisation scale factor and renormalisation scale factor, respectively.

Two different choices for μ_0 were made. The more common one for VBF-type reactions is related to the momentum transfer of the attached electroweak bosons,

$$\mu_{0,i}^2 = Q_i^2 = \left| p_{\text{in}}^i - \sum_{k \in \text{final state}} p_k^i \right|^2. \tag{3.15}$$

Here the sum runs over all final-state partons on line i, so there can be one or two summands depending if the scale is calculated for a real-emission or a Born-type configuration. With this choice of a scale parameter, two different scales are applied to the upper and lower fermion line. Another possible choice is to sum transverse momenta of all jets and set

$$\mu_0^2 = m_H^2 + \sum_{\text{jets}} p_{Tj}^2. \tag{3.16}$$

$\sigma^{\text{inclusive}}$[fb] for $\sqrt{S} = 14$ TeV and $m_H = 126$ GeV

LO				
	CTEQ		MSTW	
ξ	$\mu_0^2 = Q_i^2$	$\mu_0^2 = m_H^2 + \sum p_{Tj}^2$	$\mu_0^2 = Q_i^2$	$\mu_0^2 = m_H^2 + \sum p_{Tj}^2$
0.5	28.68	27.44	28.60	27.24
1.0	27.55	26.34	27.37	26.07
2.0	26.45	25.30	26.19	24.96
NLO				
	CTEQ		MSTW	
ξ	$\mu_0^2 = Q_i^2$	$\mu_0^2 = m_H^2 + \sum p_{Tj}^2$	$\mu_0^2 = Q_i^2$	$\mu_0^2 = m_H^2 + \sum p_{Tj}^2$
0.5	28.22	28.75	28.06	28.60
1.0	28.55	28.85	28.41	28.76
2.0	28.67	28.85	28.58	28.76

σ^{VBF}[fb] for $\sqrt{S} = 14$ TeV and $m_H = 126$ GeV

LO				
	CTEQ		MSTW	
ξ	$\mu_0^2 = Q_i^2$	$\mu_0^2 = m_H^2 + \sum p_{Tj}^2$	$\mu_0^2 = Q_i^2$	$\mu_0^2 = m_H^2 + \sum p_{Tj}^2$
0.5	15.63	14.43	15.43	14.16
1.0	14.55	13.48	14.29	13.16
2.0	13.60	12.63	13.29	12.28
NLO				
	CTEQ		MSTW	
ξ	$\mu_0^2 = Q_i^2$	$\mu_0^2 = m_H^2 + \sum p_{Tj}^2$	$\mu_0^2 = Q_i^2$	$\mu_0^2 = m_H^2 + \sum p_{Tj}^2$
0.5	14.61	14.87	14.56	14.83
1.0	14.81	14.89	14.76	14.84
2.0	14.86	14.79	14.80	14.72

Table 3.1: Cross sections obtained for different values of the scale factor $\xi = \xi_F = \xi_R$ within inclusive (top) and VBF cuts (bottom). The errors of the results are below the permille level.

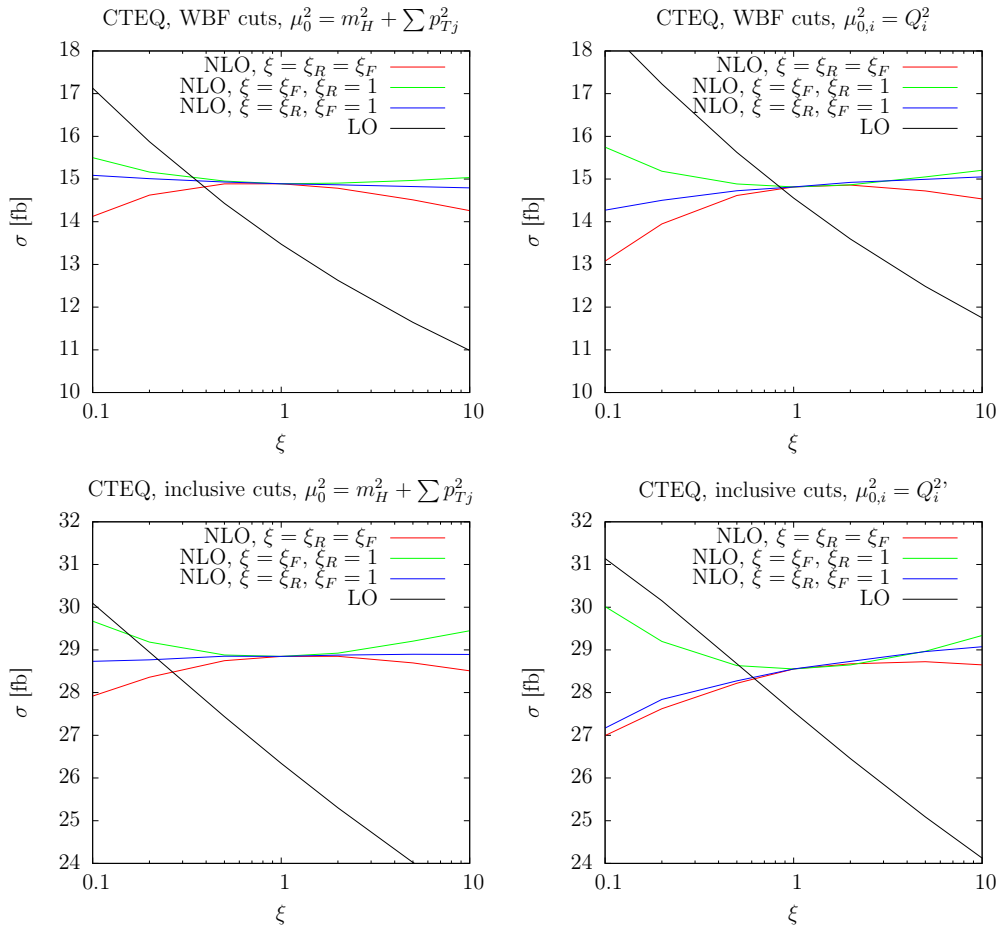

Figure 3.3: Cross sections with CTEQ PDFs as function of the scale factor ξ.

The general behaviour upon variation of the scale factors and basic scale choices can be seen in Figure 3.3. For the graphs, the scale factors were varied between values of 0.1 to 10. Also, the impact of independent variation of the renormalisation and factorisation scale is shown.

The integrated cross sections for inclusive and VBF cuts are collected in Table 3.1. For the table, the scale factors were set to $\xi_F = \xi_R = \xi$ and were varied between $\xi = 0.5$ and $\xi = 2.0$. The variation of the cross section in that range decreases from about 15% at LO to 2% at NLO for VBF cuts. For inclusive cuts, the scale variation is only 8% already at LO and the NLO stabilises the dependencies again up to around 2%. The K-factor, defined as

$$K = \frac{\sigma^{NLO}}{\sigma^{LO}}, \tag{3.17}$$

is generally larger for the $\mu_0^2 = m_H^2 + \sum p_{Tj}^2$ scale choice than for $\mu_0^2 = Q_i^2$. Also, the impact of the scale variation on the latter is smaller.

In order to examine the impact of the PDF choice, the results for both CTEQ and MSTW PDFs are listed in Table 3.1. At LO, switching from CTEQ to MSTW

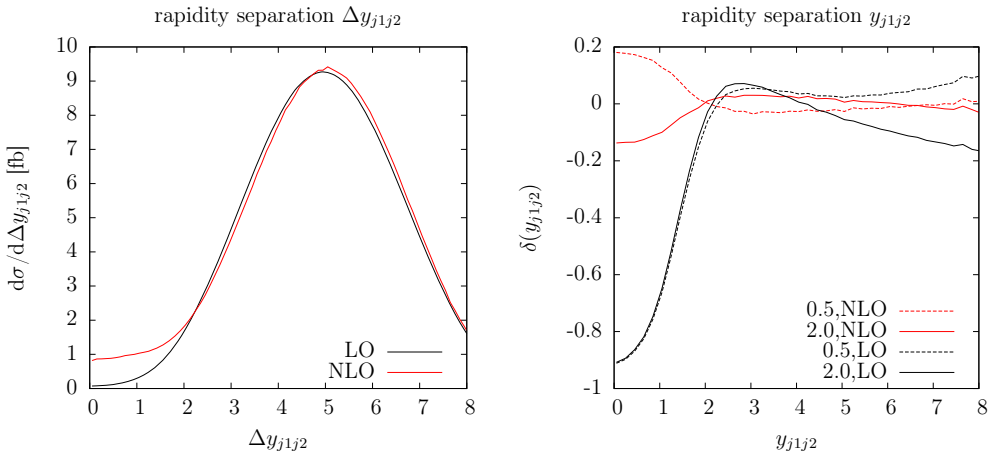

Figure 3.4: Rapidity separation distribution of the tagging jets and corresponding distribution of the δ function as defined in (3.18) for inclusive cuts.

decreases the cross section by about 1% and thereby affects the cross section less than the scale variation. When going to NLO, the relative importance of the PDF uncertainty increases as the scale dependence decreases. Both uncertainties end up being small and of comparable size of about 2%. The choice of the basic scale factor μ_0 shows an effect on the cross sections of the same magnitude.

Understanding the kinematic properties of the tagging jets is of vital importance when it comes to the selection of VBF events at a collider experiment. The rapidity separation of the tagging jets in VBF-like reactions is generally larger than in QCD-induced background processes (see for example [87]). The invariant mass distributions also peak at higher values. Therefore, to diminish background influences, both, rapidity separation and invariant mass of the tagging jets, belong to the most efficient observables to cut on. Figure 3.4 shows the rapidity separation of the two tagging jets in $H\gamma jj$ production for inclusive cuts. In the lower end of the distribution, the shape receives large corrections by additional radiations. This can happen primarily if the two hardest emissions stem from the same fermion line. However, these parts are removed when switching to the VBF cuts scenario. The bulk of the Δy_{j1j2} distribution is shifted to slightly larger values, although the NLO-corrected curve follows the LO result closely.

In Figure 3.5, the invariant mass distribution of the two hardest jets is plotted, again for inclusive cuts. Unlike the relevant QCD background, the m_{jj} distribution in $H\gamma jj$ production peaks at high values and falls off slowly. It is only mildly affected by QCD corrections, which shift the curve to lower values of the invariant mass.

To analyse the phase space dependence of NLO corrections and scale uncertainties, the variable

$$\delta(\mathcal{O}) = \frac{\mathrm{d}\sigma(\xi_F, \xi_R)/\mathrm{d}\mathcal{O}}{\mathrm{d}\sigma^{NLO}(\xi = 1)/\mathrm{d}\mathcal{O}} - 1 \tag{3.18}$$

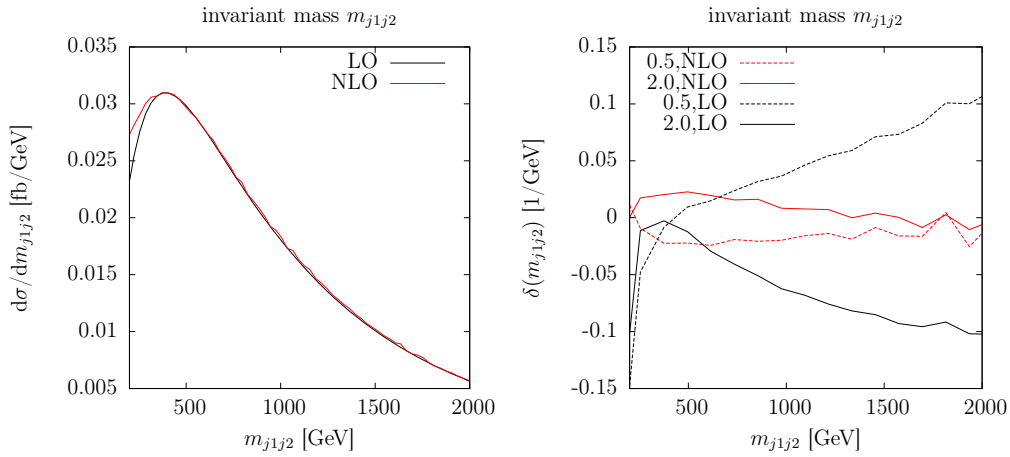

Figure 3.5: Invariant mass distribution of the tagging jets and corresponding distribution of the δ function for inclusive cuts.

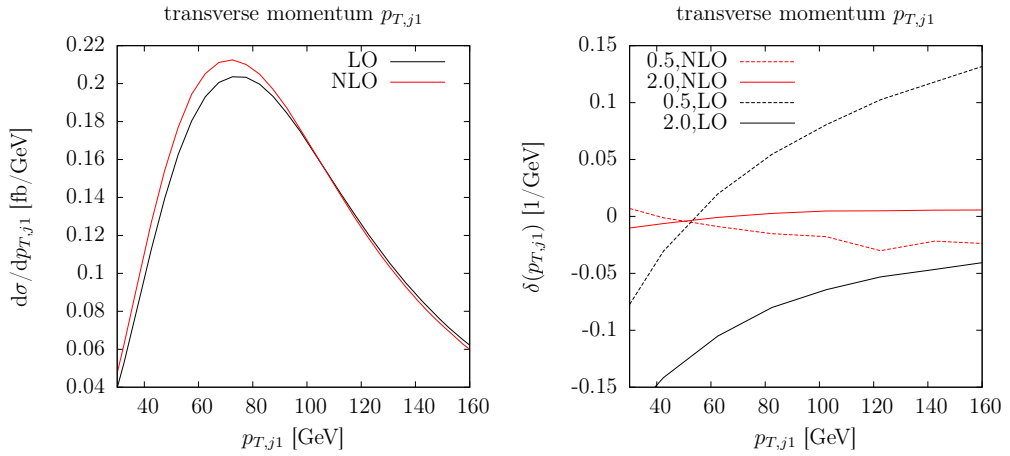

Figure 3.6: Transverse momentum distribution of the hardest jet and corresponding distribution of the δ function for VBF cuts.

is of avail. $\mathrm{d}\sigma(\xi)/\mathrm{d}\mathcal{O}$ in the numerator can be either the LO or NLO differential cross section, which is normalised to the NLO distribution with the same scale parameter choice μ_0 and a fixed scale parameter $\xi = 1$. In the case at hand, the scale factors ξ_F and ξ_R are set to equal values which are varied from 0.5 to 2.0.

Plots for the transverse momenta of the two hardest jets and the corresponding distribution $\delta(p_{Tj1/2})$ are shown in Figures 3.6 and 3.7. It can be observed that the NLO QCD corrections are positive and in particular considerable in the lower end of the distribution. For high transverse momenta above a certain value, which depends on the scale factor, the sign of the corrections changes. The scale uncertainty at LO, which can be inferred as the bands in between the two LO curves for $\xi = 0.5$ and $\xi = 2.0$, increases with the transverse momentum, reaching almost 20% at $p_{Tj1} = 200\,\mathrm{GeV}$.

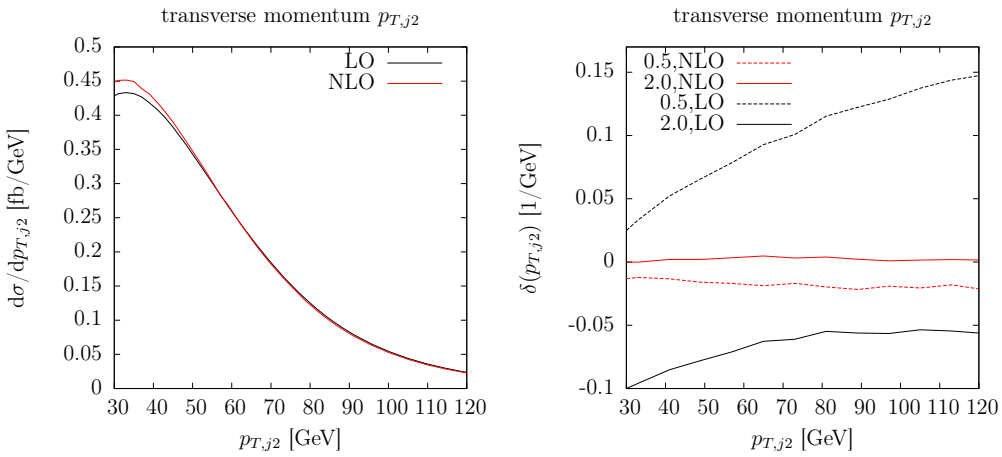

Figure 3.7: Transverse momentum distribution of the second hardest jet and corresponding distribution of the δ function within the VBF cuts scenario.

The remaining scale uncertainties for the NLO approximation, on the other hand, are very stable. The width of the envelope increases with higher transverse momenta. Over the whole plotted range, the scale uncertainties stay well below 5%.

The rapidities of the tagging jets are depicted in Figure 3.8 and Figure 3.9. Everywhere but in the central region, the NLO corrections are positive. This is also the region where the scale uncertainty at NLO attains its highest value of around 8%.

Another experimentally interesting distribution is the azimuthal angle difference of the tagging jets $\Delta\Phi_{jj}$. Although generally taken between 0 and π, its definition can be extended to an interval from $-\pi$ to π [87] by

$$\Delta\Phi_{jj} = \Phi_{j\eta_{max}} - \Phi_{j\eta_{min}}. \tag{3.19}$$

Here, $\Phi_{j\eta_{max/min}}$ is the azimuthal angle of the tagging jet with the larger/smaller pseudorapidity. This definition is manifestly invariant under the mirroring of the z-axis, as the sign of the pseudorapidity also changes under this transformation. The benefit of this modified definition is to distinguish between different $\mathcal{CP}$-mixed couplings in models beyond the SM [88,89]. In a multi-particle environment beyond the NLO approximation, even the definition of $\Delta\Phi_{jj}$ needs to be adapted, as additional splittings conceal the tensor structure of the underlying coupling [90].

In Figure 3.10, the azimuthal angle separation of the tagging jets in $H\gamma jj$ production is depicted. The shape is rather insensitive to NLO corrections, although the corrections are slightly larger for back-to-back situations. At NLO, the dependence of the scale uncertainties on the value of $\Delta\Phi_{j1j2}$ decreases. The remaining uncertainty is about 2% over the whole observable range.

To illustrate the position of a final-state particle or jet X in relation to the tagging jets without being biased by the boost of the centre-of-mass system, in

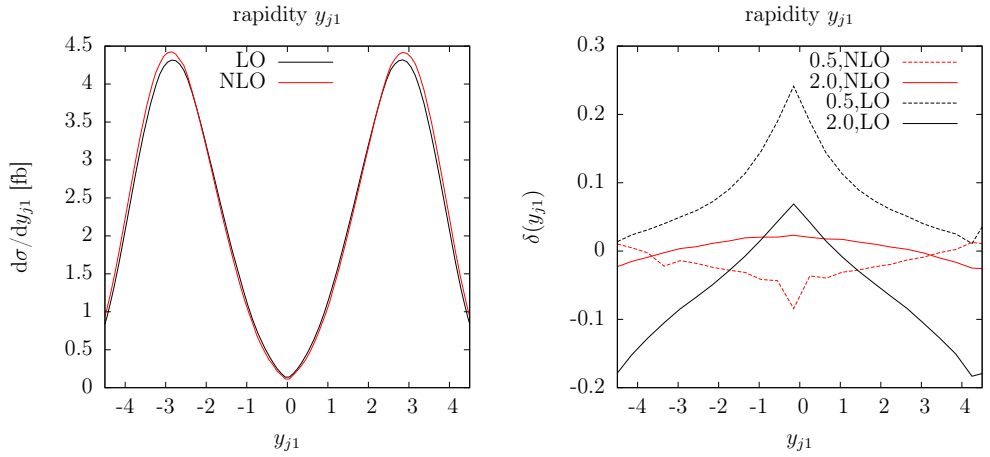

Figure 3.8: Rapidity distribution of the hardest tagging jet and corresponding distribution of the δ function for VBF cuts.

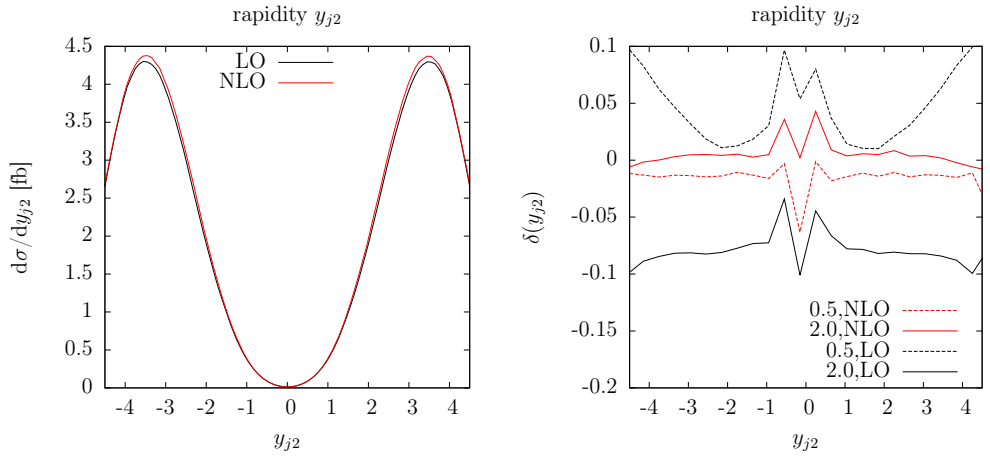

Figure 3.9: Rapidity distribution of the second hardest tagging jet and corresponding distribution of the δ function for VBF cuts. In the central region, the results are numerically unstable as the cross section decreases to zero here.

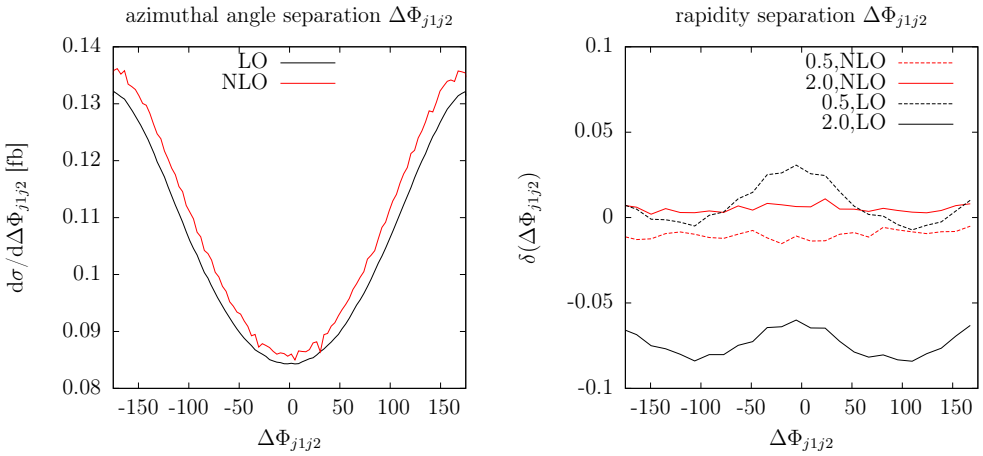

Figure 3.10: Azimuthal angle separation distribution of the tagging jets and corresponding distribution of the δ function as defined in (3.18).

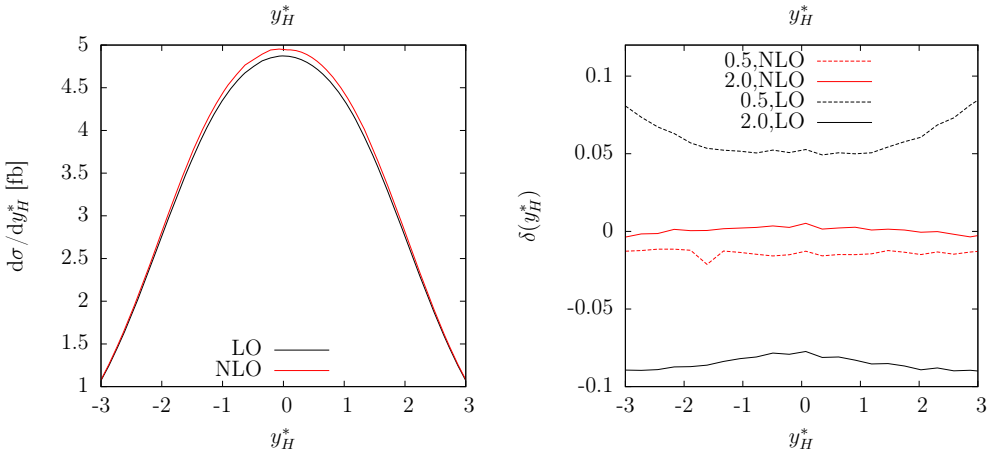

Figure 3.11: y_H^* distribution as defined in (3.20). The distribution shows a clear preference for central emission of the Higgs boson.

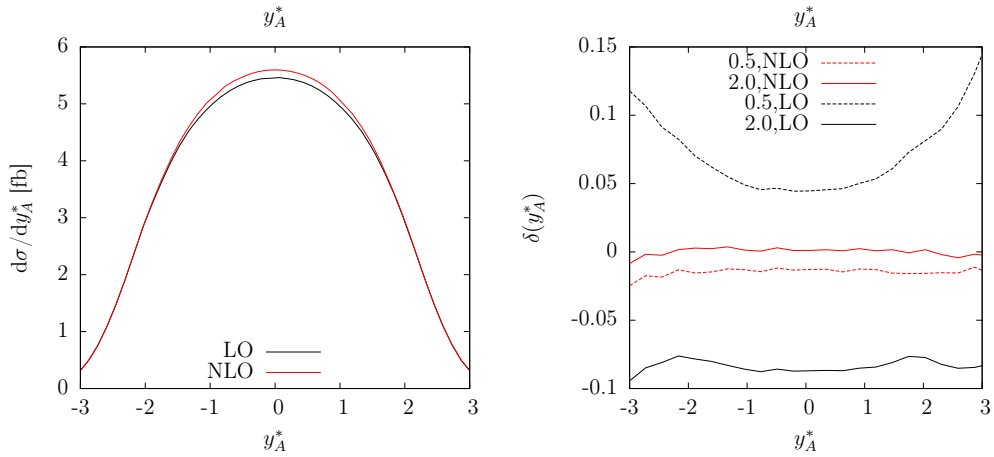

Figure 3.12: y_A^* distribution as defined in (3.20). Due to the enhancement of the charged current subprocesses, the photon, just like the Higgs boson, shows a broad peak in the central region.

VBF-like reactions often the variable

$$y_X^* = y_X - \frac{|y_{j1} - y_{j2}|}{2} \tag{3.20}$$

is considered. X is taken to be either the Higgs boson or the photon in Figure 3.11 and Figure 3.12 respectively. Both distributions peak at 0, which is expected in VBF-like reactions, as they favour this topology. At LO, the scale uncertainties are largely dependent on the values of $y_{H/A}^*$. This dependence decreases vastly at NLO, where the remaining uncertainties appear flat and add up to about 2%.

Summary of part II

As part of the work for this thesis, the cross section for $H\gamma jj$ production via vector boson fusion was calculated at NLO QCD. The code of the author was released publicly as part of the parton-level Monte-Carlo program VBFNLO. It allows the calculation of cross sections and kinematical distributions within flexible cuts settings. The VBF approximation made for the implementation is valid if a large rapidity separation of the tagging jets is required.

Results were shown for two different sets of cuts, one being an inclusive set and the other requiring realistic VBF selection cuts. In order to estimate the PDF uncertainty, two different PDF choices were made, namely CTEQ and MSTW. The calculation has shown that the impact of the PDF choice on the cross section is small and around 2%. In addition, the program was run with different scale choices and the scale factors were varied to determine the remaining scale uncertainties of the total cross section. These have shown to be small and of the order of the PDF uncertainties.

Different kinematical distributions were examined to gain information about the differential influence of the NLO corrections. Depending on the observable and the region of phase space, corrections can be substantial. The differential scale uncertainties were also investigated and are reduced drastically compared to the LO results.

The next part of this thesis is dealing with effects that arise when going beyond a fixed order calculation. For this purpose, parton showers are applied to Hjj production via VBF. New sources of uncertainties show up by the shower implementations and, when going to NLO, also by the matching scheme that is used.

Part III

NLO matched Higgs boson production via vector boson fusion

Chapter 4

Herwig++ generalities

4.1 Matchbox

Matchbox is an addon to Herwig++. Its main purpose is to deliver a framework for automated NLO matchings. Within Matchbox, both MC@NLO-type and POWHEG-type matchings can be computed once the matrix elements are set up. For a convenient implementation of new matrix elements, the generation of Catani-Seymour dipole subtraction terms is also fully automated within the framework.

To implement a new process, the user has to supply spin and colour correlated matrix elements as defined in [66] and Born, virtual and real-emission contributions. The event generator needs to be given information about the Feynman diagrams of the process and colour flows in the large-N_C limit. In its current version, both can be generated automatically.

Matchbox implements two different ways of interfacing external parton-level Monte Carlos. First, the user can supply squared matrix elements. The other option is handing over colour ordered amplitudes, which can be more convenient depending on the structure of the parton-level Monte Carlo. In the calculation presented in this study, the first option is chosen and VBFNLO is used to supply the squared matrix elements.

Within this study, an interface between Matchbox and the parton-level Monte-Carlo program VBFNLO was established in order to calculate Hjj production via VBF within different setups. As VBFNLO is written in FORTRAN77 and Herwig++ in C++, a mixed language interface had to be established. This was achieved using the framework provided by `cfortran.h` [91]. Details on the implementation of the interface are given in Appendix B.

During the work on the project, Matchbox could be tested thoroughly. The need for many new features such as automatic phase space generation and different samplers arose during the implementation of Hjj production. As Hjj was one of the first external matrix elements that were interfaced with Matchbox, several issues had to be identified and fixed. In that way, the project at hand also served as a good debugging environment for Matchbox.

4.2 Samplers

Matchbox comes with an adaptive sampler for Sudakov-type distributions, ExSample [40]. For cross-checks, two more random number samplers are implemented. The FlatBinSampler does as the name implies and returns evenly distributed random numbers. The third built-in sampler is called ProjectingBinSampler and incorporates a VEGAS-like adaption to the integrand. However, the boundaries of the individual grid cells are not shifted after each iteration. Instead, each cell is evenly split into two or more new ones to refine the probability distribution.

4.3 Phase space generation

Matchbox also features an automated phase space generator, the TreePhasespace, based on the phase space decomposition described in Section 2.3. To avoid biases introduced with the numerical safety cuts, the momenta are not always generated in a tree-like structure starting from the same incoming parton, but the starting parton is chosen randomly. The information on the Feynman diagrams of the process is taken from the Herwig++ internal Tree2toNDiagram class, which every process has to supply. For processes featuring more than one diagram, more than one phase space mapping is possible, leading to a multi-channel approach. The random number density relevant for the channel selection can be adapted by the sampler, so that for each phase space region, the most contributing channels can be selected with a higher chance. For debugging purposes, an implementation of the flat phase space generator RAMBO [92] is also supplied.

As the peak structure of a matrix element changes with the involved particle masses, the TreePhasespace implementation features different kinds of mappings for different types of propagators. Always, each dimensionful quantity is given in units of the partonic center-of-mass energy of the process $\hat{S}$.

The invariant m for a particle with a non-zero decay width Γ and on-shell mass M can be calculated with a Breit-Wigner mapping. The probability distribution of the invariant is

$$p^{\mathrm{BW}}(x) = \frac{1}{(x-z)^2 + |wz|} \tag{4.1}$$

where z is the pole and w the width of the resonance. For the mapping,

$$I_r^{\mathrm{BW}} = \frac{1}{\sqrt{wz}} \left[\arctan \frac{u-z}{\sqrt{wz}} - \arctan \frac{l-z}{\sqrt{wz}} \right] \tag{4.2}$$

and

$$I_0^{\mathrm{BW}} = \frac{1}{\sqrt{wz}} \arctan \frac{l-z}{\sqrt{wz}}, \tag{4.3}$$

are defined with u and l as upper and lower bounds on the invariant to be mapped. Each parameter is expressed in units of $\hat{S}$,

$$\begin{aligned} z &= \frac{M^2}{\hat{S}}, \\ w &= \frac{\Gamma^2}{\hat{S}}, \\ u &= \frac{m_{max}^2}{\hat{S}}, \\ l &= \frac{m_{min}^2}{\hat{S}}. \end{aligned} \tag{4.4}$$

Then, the invariant can be generated as

$$\frac{m^2}{\hat{S}} = x = z + \sqrt{w}\tan\left[\sqrt{w}\left(\mathcal{R}I_r^{BW} + I_0^{BW}\right)\right], \tag{4.5}$$

using a random number $\mathcal{R}$.

For propagators with vanishing decay width, the situation is slightly more complicated as there can be a singularity involved in the allowed mass range. For massless particles, the amplitude follows a $1/q^2$ shape. However, in practical situations this is behaviour is often softened by gauge cancellations. Therefore, it was opted to map the invariants by a reciprocal function away from the singular region. In the vicinity of the singularity z, two cutoffs x_0 and x_c need to be introduced. The value of both cutoffs can be changed by the user. In the interval $[z-x_c, z+x_c]$, no invariants are generated whereas within the intervals $[z-x_0, z-x_c]$ and $[z+x_c, z+x_0]$, the invariants are mapped using a flat probability distribution

$$p^{\text{flat}}(x) = 1, \tag{4.6}$$

by

$$x = l + \mathcal{R}(u-l). \tag{4.7}$$

In the intervals $(-\infty, z-x_0]$ and $[z+x_0, \infty)$, where the mapping is following an inverse probability distribution

$$p^{\text{flat}}(x) = \frac{1}{|x-z|}, \tag{4.8}$$

the generation of the invariant works as follows. Again, u and l are the boundaries of the interval. Let z be the pole outside the interval with $z < l$, then

$$\begin{aligned} I_r^{\text{inv},+} &= \ln\frac{u-z}{l-z}, \\ I_0^{\text{inv},+} &= \ln(l-z). \end{aligned} \tag{4.9}$$

If the pole is above the interval, $z > u$, then the parameters of the mapping are defined as

$$\begin{aligned} I_r^{\text{inv},-} &= \ln \frac{z-l}{z-u}, \\ I_0^{\text{inv},-} &= \ln (z-u)\,. \end{aligned} \tag{4.10}$$

In both cases, the mapping is carried out by

$$x = z + \text{ sign}\,(u-z) \exp\left[\mathcal{R} I_r^{inv,\pm} + I_0^{inv,\pm}\right]. \tag{4.11}$$

4.4 Herwig++ default shower

The Herwig++ default shower implementation is based on generalised Altarelli-Parisi splitting functions. These allow for $1 \to 2$ splittings of the involved coloured particles. The shower evolution is performed within a Sudakov decomposition of the involved momenta,

$$q_i = \alpha_i p + \beta_i n + q_{\perp i}, \tag{4.12}$$

where p is the momentum of the initiating parton. n is a lightlike vector, chosen anticollinear to p, maximising $n \cdot p$. $q_{\perp i}$ is perpendicular to both p and n. β_i is fixed by the relation

$$\beta_i = \frac{\mathbf{q}_{\perp i}^2 + q_i^2 - \alpha_i^2 m^2}{2\alpha_i p \cdot n}. \tag{4.13}$$

As the participating particles are considered to be massless in the shower stage, momenta cannot be conserved after each splitting. In order to only mildly violate momentum conservation, the shower algorithm starts with the determination of the shower variables which characterise each splitting. These are the light cone momentum fraction z

$$z_i = \frac{\alpha_i}{\alpha_{i-1}} \tag{4.14}$$

and the azimuthal angle of the relative transverse momentum

$$p_{\perp i} = q_{\perp i} - z_i q_{\perp i-1}, \tag{4.15}$$

which is given with respect to the direction of p. The third shower variable involved is the shower evolution scale q. The evolution variable is chosen differently in initial-state radiation than in final state radiation. The choices are described in great detail in [7].

After these are determined, the shower evolution stops and the physical momenta are reconstructed. The outgoing partons are set on shell and the coefficients of the Sudakov basis are calculated iteratively. As this renders the intermediate

partons off shell, all momenta of the particles in the final-state shower undergo a Lorentz transformation which, for final state radiation, is required to leave the centre-of-mass energy untouched by the shower evolution. The rescaling factor determining this Lorentz transformation is defined by

$$\sum_j \sqrt{\mathbf{p}_j^2 + m_j^2} = \sum_J \sqrt{k^2 \mathbf{q}_J^2 + q_J^2} = \sqrt{s}. \tag{4.16}$$

Here, p_j are the momenta of the partons involved in the hard matrix element before the shower, q_J are those after the shower and m_J is the mass of particle J.

For initial-state radiation, the required conditions for the Lorentz boost depend on if the colour-connected partner of the shower-initiating particle is incoming or outgoing. In the former case, the rescaling is chosen in a way to preserve both energy and rapidity of the partonic centre-of-mass system and the boost is applied to all jets emerging from initial-state radiation. If the hard parton starting the shower shares a colour line with an outgoing particle in the hard matrix element, the boost is required to leave the momentum transfer Q^2 of the system invariant.

4.5 Dipole shower

Recently, a new shower algorithm was implemented into Herwig++, based on Catani-Seymour dipoles [62, 93]. It features $2 \to 3$ splittings, so that momenta can be conserved in each step of the shower. With the Catani-Seymour splitting kernels, the MC@NLO matching, described in Section 2.4.2, can be greatly simplified. The dipole shower is ordered in transverse momentum of the emissions, so within an implementation of the POWHEG matching scheme no truncated showers are needed to model soft wide-angle emissions. As an additional benefit, the structure of the dipole splitting kernels allows for an almost complete phase space coverage, unlike in the default shower implementation.

In any implemented process, information about the involved colour lines in the large N_C limit is given to Herwig++. The dipole shower first starts to order particles connected by the same colour line and their anticolour line into singlet objects called dipole chains. To achieve this, the process $x + y \to a + b + c + \cdots$ is crossed to $x + y + \bar{a} + \bar{b} + \bar{c} + \cdots = 0$, i.e. an outgoing colour line is interpreted as an incoming anticolour line.

For each of those dipole chains, all possible dipole splittings together with all possible emitter-spectator assignments are considered. The algorithm determines which of the competing splittings is carried to execution by assigning a splitting scale to each of them with a probability deduced from the relevant Sudakov form factor. The splitting with the highest splitting scale is actioned, leading to a modification of the dipole chain it is emitted from. Among the possible modifications is also the breakup of a chain, in which case both parts of the chain undergo separate evolution from this point on.

The dipole shower proceeds on the same chain until the chosen splitting scale is below the infrared cutoff, typically around 1 GeV. Another dipole chain is chosen

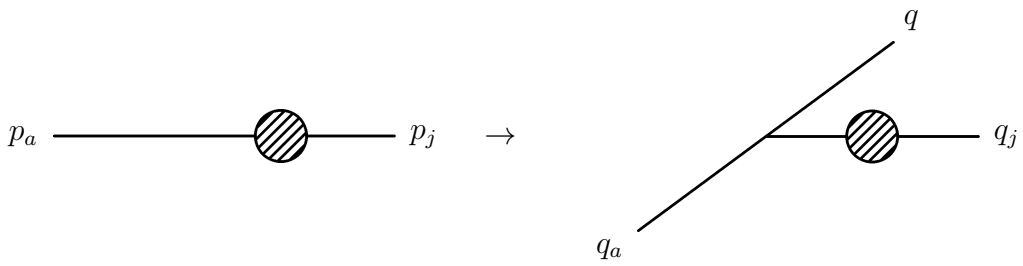

Figure 4.1: Initial-final state splitting in the non-collinear scheme. Both emitter and emission pick up transverse momentum.

then and undergoes the shower evolution until no more splittings above the cutoff are found. This is pursued until all dipole chains were processed and the algorithm is terminated.

4.5.1 Splitting schemes

There are different roads that can be chosen to implement Catani-Seymour splittings with an initial state emitter a and final state spectator j. Reviewing the kinematics in [66], the generated momenta can be partitioned in multiple ways which differ by Lorentz transformations. One of the possibilities is to assign no transverse momentum to the spectator at all. Then, the transverse momentum has to be balanced by the emitter and its emission. This option shall be called non-collinear scheme in the following and is sketched in Figure 4.1. In this case, the kinematics of the splitting $(p_a, p_j) \to (q_a, q, q_j)$ can be parameterised with

$$x = \frac{p_a \cdot p_j}{(p_a - p_j) \cdot q_a}, \qquad u = \frac{q_j \cdot q_a}{(p_a - p_j) \cdot q_a} \tag{4.17}$$

as

$$q_a = \frac{1-u}{x-u} p_a + \frac{u}{x}\frac{1-x}{x-u} p_j + \frac{1}{u-x} k_\perp, \tag{4.18}$$

$$q = \frac{1-x}{x-u} p_a + \frac{u}{x}\frac{1-u}{x-u} p_j + \frac{1}{u-x} k_\perp, \tag{4.19}$$

$$q_j = \left(1 - \frac{u}{x}\right) p_j. \tag{4.20}$$

The other extreme of distributing the generated transverse momentum is to assign it to the spectator solely. This situation is depicted in Figure 4.2. The emitter's momentum stays collinear to its momentum before the emission in this case. This is what will be called collinear scheme from now on. It can be parame-

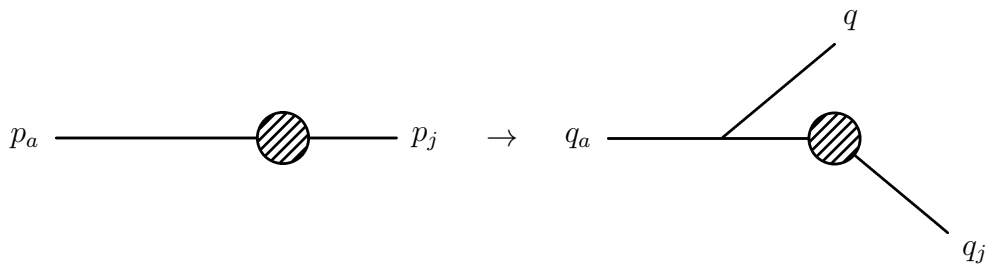

Figure 4.2: Initial-final state splitting in the collinear scheme. The emitter stays collinear after the emission.

terised by x and u as defined in (4.17), leading to the momenta

$$q_a = \frac{1}{x} p_a, \tag{4.21}$$

$$q = \frac{(1-x)(1-u)}{x} p_a + u p_j + k_\perp, \tag{4.22}$$

$$q_j = \frac{(1-x)u}{x} p_a + (1-u) p_j - k_\perp, \tag{4.23}$$

after splitting. Here, the indexing is kept the same as in the non-collinear scheme described above.

In the non-collinear scheme, the initial-state parton picks up transverse momentum and is no longer on the beamline. The event needs to be realigned to render the incoming momenta on the z-axis. To this end, the whole event is Lorentz transformed. The required transformation consists of a boost into the centre-of-mass system of the incoming partons after termination of the shower, which yields them to be anticollinear to each other, but not necessarily along the beamline. To provide that, an additional rotation of the event needs to be performed. Lorentz transformations involved in the realignment are not necessarily small.

For one splitting of an initial-final dipole, the collinear and non-collinear scheme produce identical results. For a realistic setting, they differ as the realignment in the non-collinear scheme is applied to the whole event only once after the termination of the shower. The situation in the collinear scheme can be interpreted as boosting the involved momenta in each splitting.

Chapter 5

Preliminaries

During the past decades, many processes were examined to find ideal potential signals for a Higgs boson at the LHC. Vector boson fusion is one of the keystones in both ATLAS [94] and CMS Higgs searches [95].

The basic principles that make the VBF processes promising for Higgs searches, namely the large rapidity separation between the tagging jets and the restricted colour flows leading to suppressed radiation in the rapidity gap, are the ones that are also interesting from a theorists point of view when it comes to parton showers. The colour flows in the matrix elements result in a challenging environment, therefore Hjj production is a good starting point for a comparison of the Herwig++ default and dipole shower implementations as well as the two matching schemes supplied by the Matchbox addon, MC@NLO and POWHEG.

5.1 Setup of the analysis

In the simulation of a parton shower, two different stages of cuts appear. Before an event is showered, *generation cuts* are applied to the partons in the hard matrix element which is evaluated. For an NLO matrix element, the generation cuts are of course applied to already recombined jets, as the Catani-Seymour algorithm requires an infrared and collinear safe definition of final state objects. Generation cuts decide if the event even enters the shower algorithm at all or gets sorted out beforehand. Another set of cuts can be applied after the event generation and works on recombined jets. These are called *analysis cuts* as they need to be fulfilled by an event to enter the analysis routines.

For a realistic analysis, generation cuts should always be looser than the analysis cuts as events might migrate over the cut borders in both ways. Too soft generation cuts, on the other side, lead to an increasing need for computing power, as the time consuming event generation needs to be run for many events which are discarded.

In the following analyses, wherever "results after shower" are mentioned, no effects of hadronisation, decays of instable particles or underlying event simulation enter the results, as this is beyond the scope of this study. All parts of the simulation but the shower were switched off.

After the simulation, a jet algorithm is run on the particles in the final state. The default that is used here is the k_T-jet algorithm, as implemented by the FastJet package [96, 97]. The jet resolution parameter is set to $D_{\text{cone}} = 0.7$. The recombination of momenta takes place in the E-scheme, which means simply adding the four momenta.

5.1.1 Analysis cuts

A recombined object is called a jet if it features a transverse momentum of

$$p_{T,j} > 20\,\text{GeV} \tag{5.1}$$

and lies within the rapidity range

$$-5 > y_j > 5. \tag{5.2}$$

An event needs to feature at least two jets to be analysed.

The matrix element for Hjj production via vector boson fusion that is employed for this study makes use of the VBF approximation, which neglects t- and u-channel interferences. Therefore, the tagging jets are required to be separated in pseudorapidity by at least

$$|\eta_{j1} - \eta_{j2}| > 4.0. \tag{5.3}$$

In addition, they need to reside in different detector hemispheres

$$\eta_{j1} \cdot \eta_{j2} < 0 \tag{5.4}$$

and exhibit a large invariant mass

$$m_{j1j2} > 600\,\text{GeV}. \tag{5.5}$$

5.1.2 Generation cuts

For NLO matrix elements, the generation cuts are not applied to partons but to already recombined objects, as a jet algorithm is involved. To avoid confusion, these (possibly) recombined objects are subsumed under the term recombined partons in this section. The generation cuts are as follows. The matrix element is required to feature at least two recombined partons with transverse momenta larger than

$$p_{T,p} > 15\,\text{GeV} \tag{5.6}$$

and reside in the rapidity range between

$$-5.5 < y_p < 5.5, \tag{5.7}$$

which both are slightly weaker requirements as in the analysis cuts. The only additional property that has to be met is a pseudorapidity separation of

$$|\eta_{p1} - \eta_{p2}| > 2.0. \tag{5.8}$$

Both the requirements for different detector hemispheres and for a minimum invariant mass of the tagging jets are dropped at this stage of the simulation.

5.1.3 PDFs and other parameters

A hadronic centre-of-mass energy of 8 TeV is assumed throughout the analysis. For LO runs, the CTEQ6L1 [82] PDFs were employed. Wherever NLO results are shown, the CTEQ10 PDF set was used [83]. Cross sections and distributions were calculated using weighted events with the FlatBinSampler without any adaption to the integrand in order to increase stability. The phase space generation was carried out within Matchbox by the TreePhasespace generator. The cutoff parameters were chosen as $x_c = 10^{-6}$ and $x_0 = 10^{-2}$.

The factorisation and renormalisation scales are given as products of a basic scale parameter μ_0 and scale factors $\xi_{F/R}$,

$$\mu_F^2 = \xi_F \mu_0^2, \qquad \mu_R^2 = \xi_R \mu_0^2. \tag{5.9}$$

The scale factors were set to unity unless stated otherwise. The basic scale parameter μ_0 was chosen as the maximum transverse momentum of the recombined partons in the matrix element,

$$\mu_0 = \max(p_{pj}). \tag{5.10}$$

All results in the following section show the production of a real Higgs boson. Its decay was not simulated, neither was a branching ratio included in any of the cross sections or plots. Wherever results employing the dipole shower are presented, the non-collinear emission scheme was used as defined in Section 4.5, unless stated otherwise.

5.2 Validation

The implementation of the matrix element interface was tested by comparing the interfaced calculation within Matchbox against the results obtained from the VBFNLO standalone program. The leading-order integrands were compared for a representative set of phase space points with full agreement.

Both programs were also compared at the level of total cross sections. They agree within the numerical errors of a few permille. Distributions calculated with the two programs are also in agreement (see Figures 5.1-5.3).

As an important part of this work consisted of the usage of the automated dipole subtraction procedure in Matchbox, which constructs the needed insertion operators as described in Section 2.4.2, the relevant subtraction terms had to be validated as well. For two of the included subprocesses and representative observables, $\sum \sigma_{\text{Dipole}}/\sigma_{\text{Real}}$ is plotted in Figure 5.4 against relevant observables in which the real emission contribution becomes singular. These are the energy of the gluon and the invariant mass of the gluon and one of the outgoing quarks. For small values on the x-axis, $\sum \sigma_{\text{Dipole}}/\sigma_{\text{Real}}$ is expected to converge to unity, as the dipole contribution should equal the real emission contribution in the singular region. Figure 5.4 shows that this is indeed the case. The convergence behaviour is

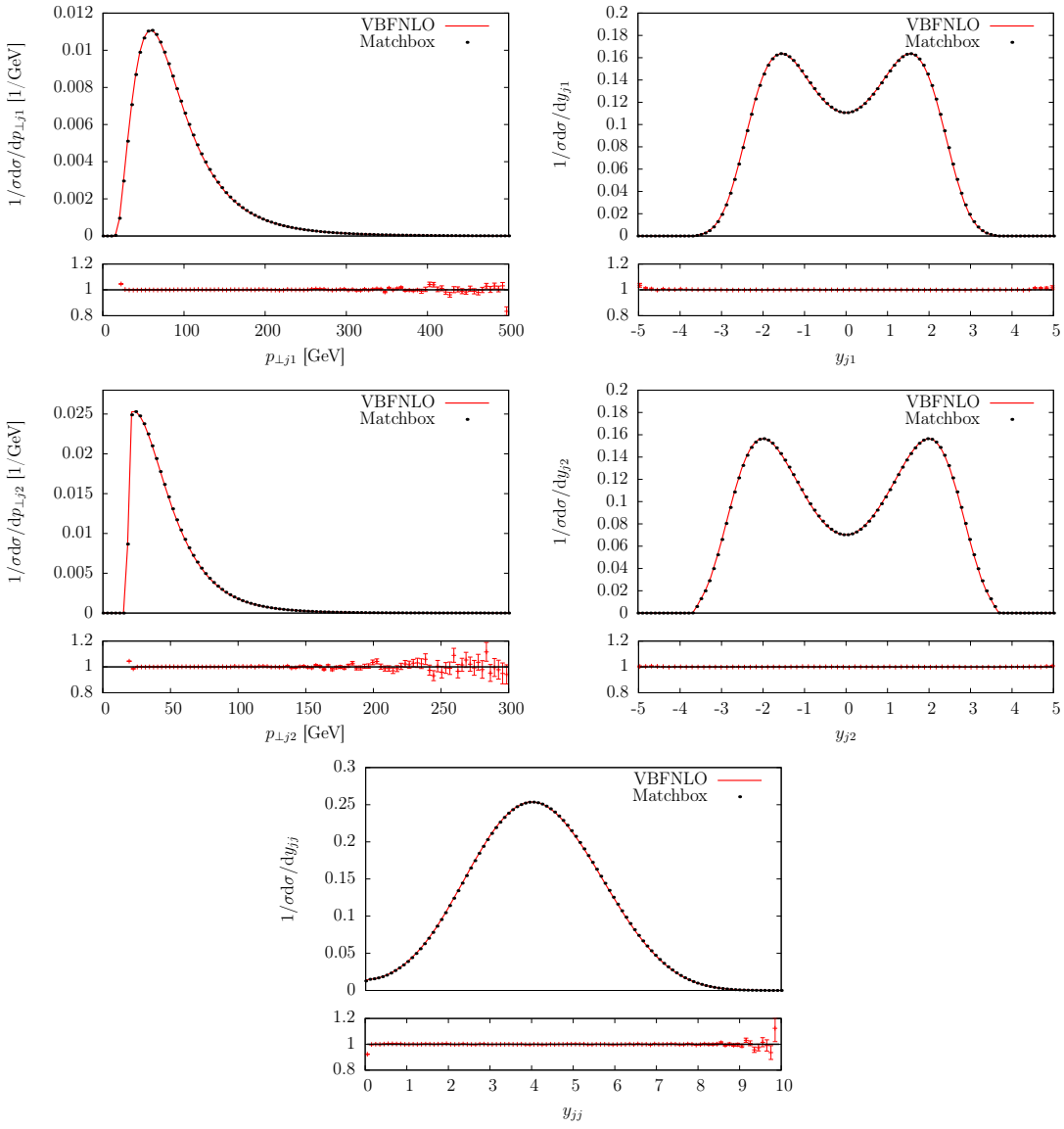

Figure 5.1: Comparison of Matchbox and VBFNLO for Hjj production at leading order. For each of the observables, the ratio $\mathrm{d}\sigma^{\mathrm{Matchbox}}/\mathrm{d}\sigma^{\mathrm{VBFNLO}}$ is plotted.

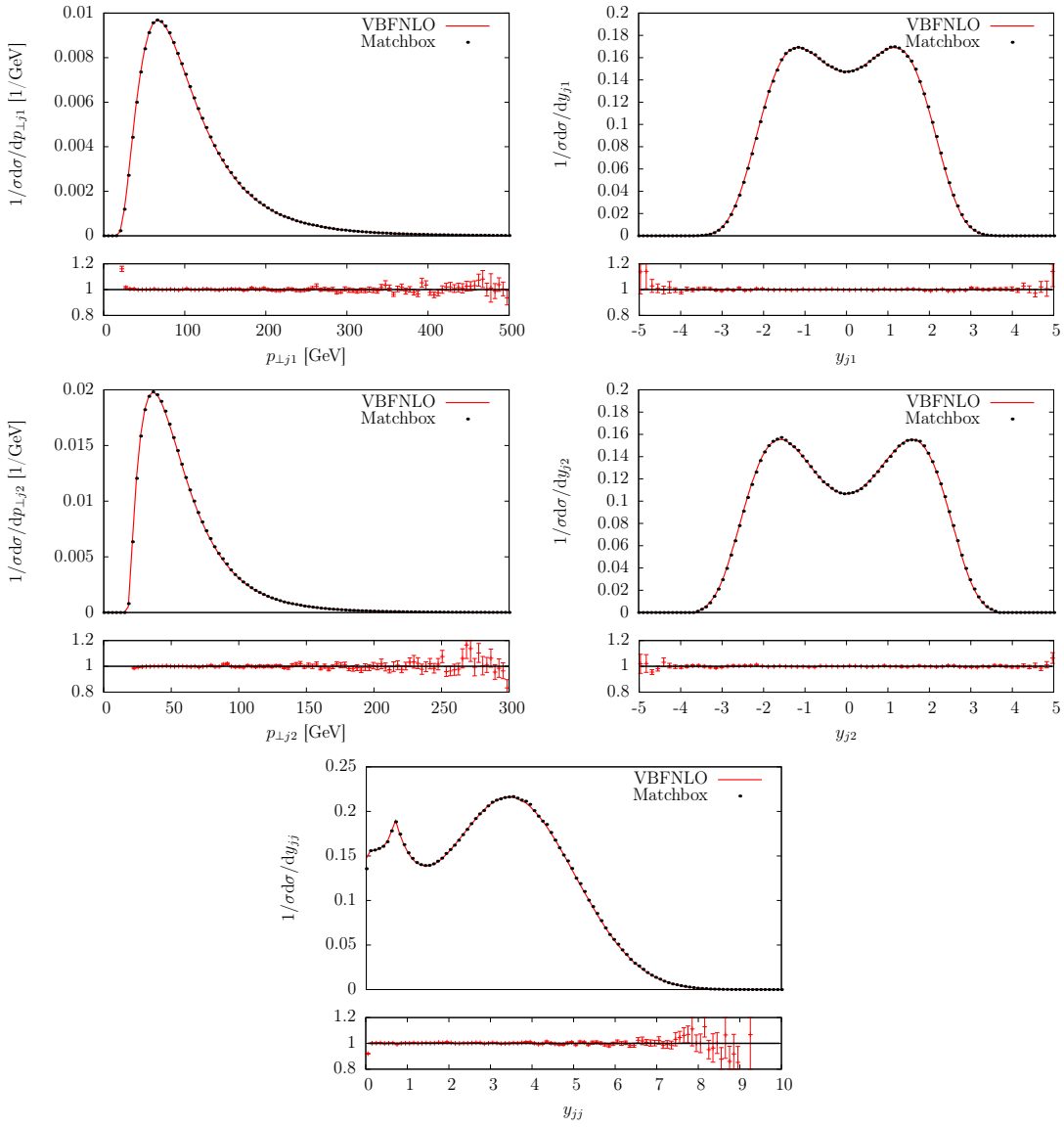

Figure 5.2: Comparison of Matchbox and VBFNLO for $Hjjj$ production at leading order. For each of the observables, the ratio $\mathrm{d}\sigma^{\mathrm{Matchbox}}/\mathrm{d}\sigma^{\mathrm{VBFNLO}}$ is plotted.

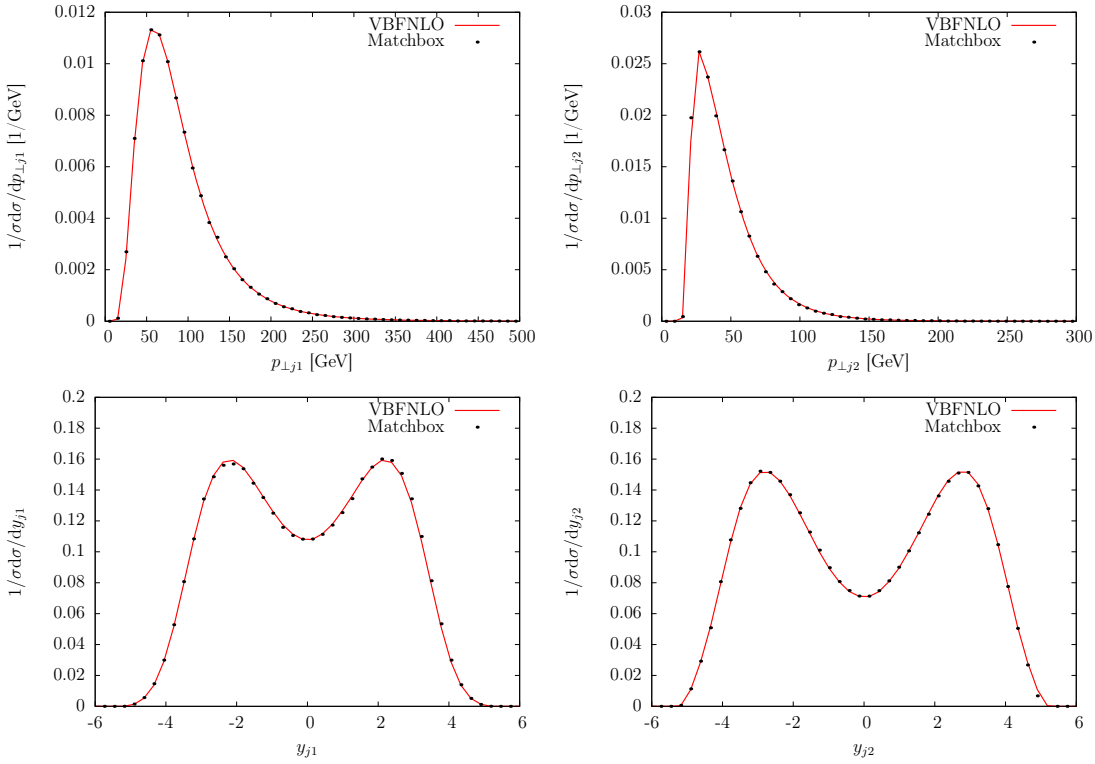

Figure 5.3: Comparison of Matchbox and VBFNLO for Hjj production at NLO. The binwise statistical errors are not handled properly at NLO, so they were left out. The convergence behaviour for a plain NLO calculation within Matchbox is worse than within VBFNLO, as Matchbox evaluates each subprocess separately, which makes it harder to obtain the required accuracy.

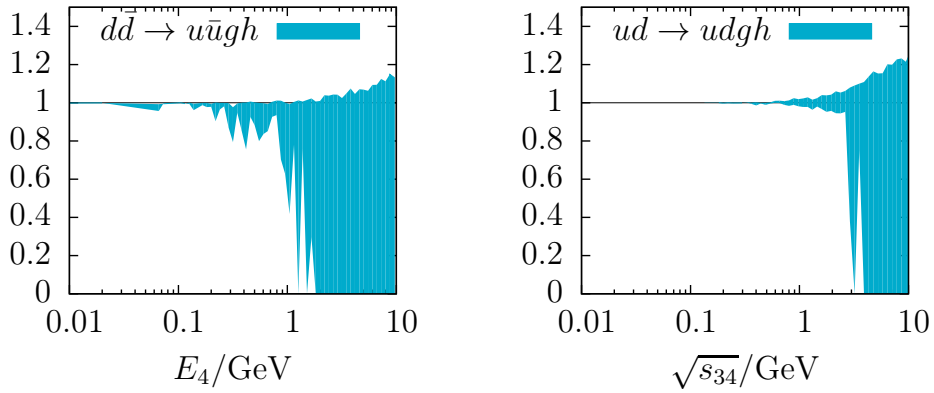

Figure 5.4: $\sum \sigma_{\mathrm{Dipole}}/\sigma_{\mathrm{Real}}$ for some of the subprocesses. In the left panel, the energy of the emitted gluon is plotted on the horizontal axis. The right panel shows the convergence behaviour as a function of the invariant mass of the outgoing d quark and the gluon. The filled area is the area between the minimum and maximum value of $\sum \sigma_{\mathrm{Dipole}}/\sigma_{\mathrm{Real}}$ in each bin.

equally good for hundreds of other subprocesses and observables, which were also checked.

The newly implemented phase space generator TreePhasespace was tested by integrating a matrix element which was set to a constant value. Within the acquired accuracy, it delivered the same phase space volume as the implementation of RAMBO. As RAMBO generates physical momenta with a flat distribution in phase space and uses a higher-dimensional random number space for this, it is considerably slower than other phase space generators.

The comparison of cross sections obtained with the TreePhasespace against RAMBO was not possible in a reliable way. The central-limit theorem states that Monte Carlo estimates converge to a normal distribution around the true value. In this way, the uncertainty of the calculation can be estimated. When using RAMBO however, the convergence was so slow that a robust error estimate of the result was not achievable in a feasible time. As the results acquired with Matchbox, which uses the TreePhasespace generator, agree with the ones obtained from VBFNLO, which uses its own phase space generator, TreePhasespace was already checked with the comparison against VBFNLO. In Figure 5.5, results from 1000 runs are plotted. The histograms represent the frequency with which a cross section in the respective bin is obtained. It is clearly visible that for a flat sampling, the TreePhasespace shows the best convergence behaviour of the three phase space generators.

It can also be noticed that RAMBO is far away from being normally distributed for the case of 2^{25} phase space points. Obviously, the central-limit theorem cannot be applied in this case because the integration with RAMBO converges too slow. A side effect is that the error estimates gained within the calculation cannot be trusted. For the case at hand, they were largely underestimated. The lesson that can be learned from this is a very general one that can be extended to other processes: Care has to be taken when doing a Monte-Carlo integration. The applicability of the central-limit theorem and the validity of the error estimation are sometimes taken for granted, but one has to keep in mind that they either need a sufficiently large number of phase space points or a good integrator.

In the current section, it was shown that the established interface between Matchbox and VBFNLO is working and that cross sections and distributions obtained within the two programs match. The Catani-Seymour dipole subtraction, which is carried out within Matchbox, converges and the subtracted results are finite. It was shown that TreePhasespace, the phase space generator of Matchbox, delivers the same cross sections as the VBFNLO-internal phase space generator. In the case of a flat sampling of random number space, TreePhasespace has proven to have the better convergence behaviour. As the validity of the implementation has been evidenced, the next chapter deals with first results and focuses on the comparison of the two shower implementations within Herwig++.

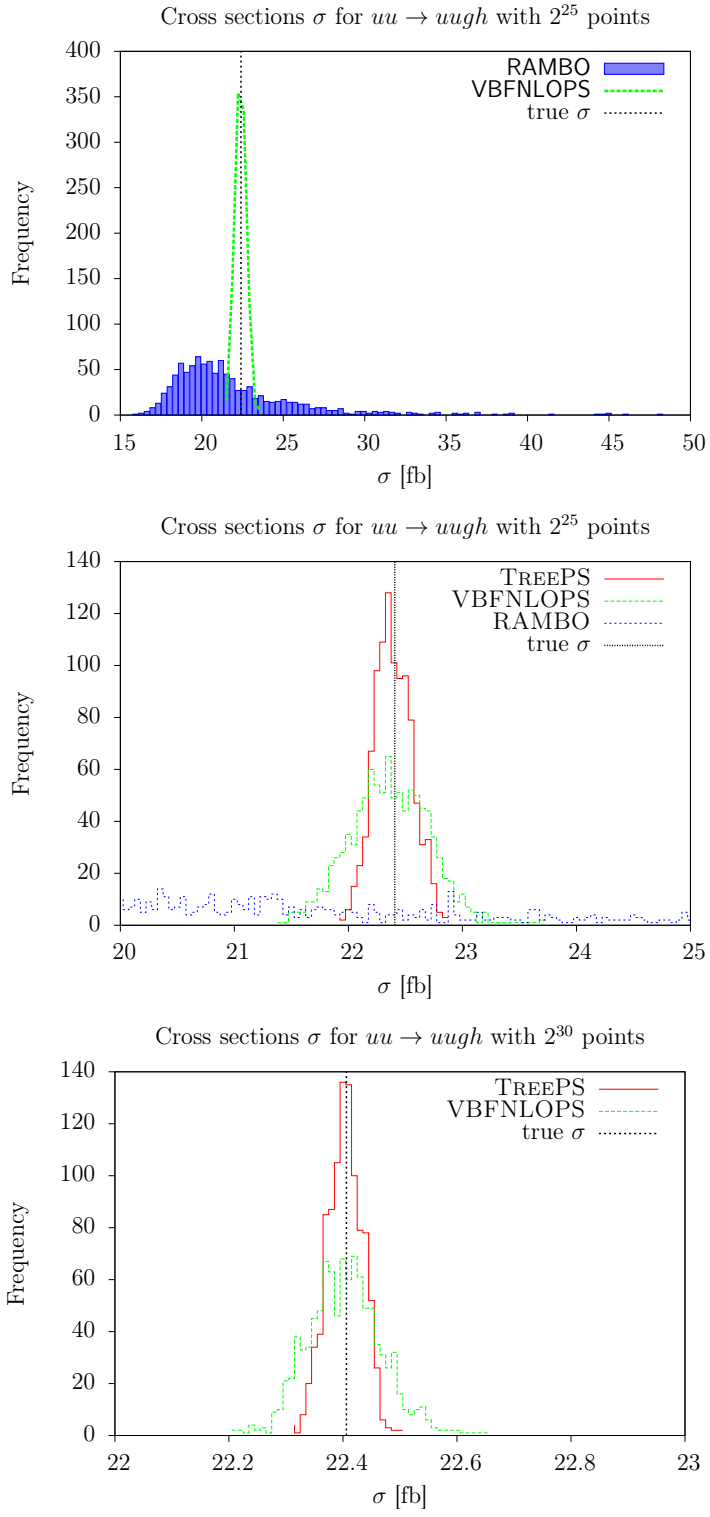

Figure 5.5: Inclusive cross sections for $uu \to uugh$ at a 14 TeV collider. Each graph corresponds to the binned results from 1000 runs with different seeds using a flat sampling of random numbers. The calculations for the upper two plots were running 2^{25} phase space points whereas each run in the lower plot comprises 2^{30} points. TreePhasespace shows a faster convergence towards the true cross section than the VBFNLO phase space. RAMBO is not able to compete with any of them.

Chapter 6

Shower effects on Hjj production at LO

The momenta which are generated within a parton shower depend on the details of its implementation. Different splitting kernels may be used, as the only property that they are bound to is the correctness within the soft and collinear limits. The basic shower properties of the two shower implementations available within Herwig++ were reviewed in Sections 4.4 and 4.5. There, it was explained that within the dipole shower, there is still a freedom in the distribution of the transverse recoil, which has to be observed.

Results for Hjj production in a parton shower approach were already examined before, e.g. in [98]. Therefore, the following chapter focuses on differences between the Herwig++ default shower and the new dipole shower. These disparities may also be interpreted as an estimate of the systematic uncertainties that arise in the LO plus parton shower calculation.

6.1 Tagging jet kinematics

The following results show Hjj production via vector boson fusion in the setup as described in Section 5.1. As a reminder, note that all simulation steps beyond the shower were turned off.

In the LO calculation already two outgoing partons are present. Due to the limited colour structure of the Hjj matrix element, the parton shower emissions are

Shower	Cross section σ[fb]
Dipole shower	400.4
Default shower	401.6

Table 6.1: Cross sections obtained with the two showers.

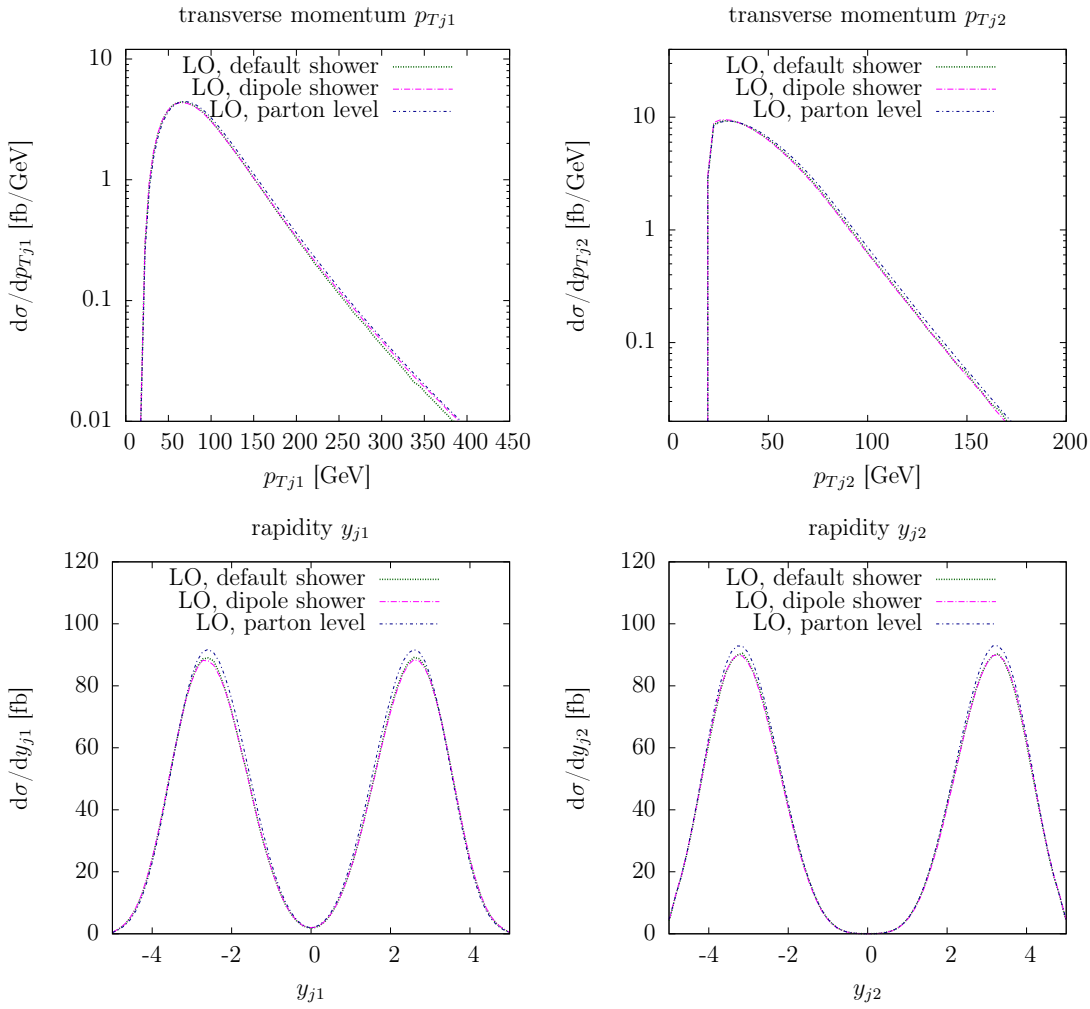

Figure 6.1: Transverse momentum distributions (upper row) and rapidity distributions (lower row) of the two tagging jets.

expected to be close to the shower-initiating partons. Hence, observables regarding the two hardest jets should only experience a minor alteration. That this is indeed the case is depicted in Figure 6.1. There, the transverse momenta and rapidities of the tagging jets are shown. The two shower algorithms both hardly modify the shape of the distributions, but only the cross section, which drops about 3%. This drop arises because events that fulfil the cuts at parton level may radiate in forbidden regions and are rejected. An example for such a behaviour is a parton with a transverse momentum just above the p_T cut resulting in two jets, each below the minimum p_T. Such an event will be rejected with a high probability as it is unlikely that the other remaining parton will produce two jets with the required rapidity separation. The cross sections obtained with the two shower algorithms are given in Table 6.1. The largest difference between the shower algorithms in Figure 6.1 arises in the tail region of the transverse momentum of the hardest jet.

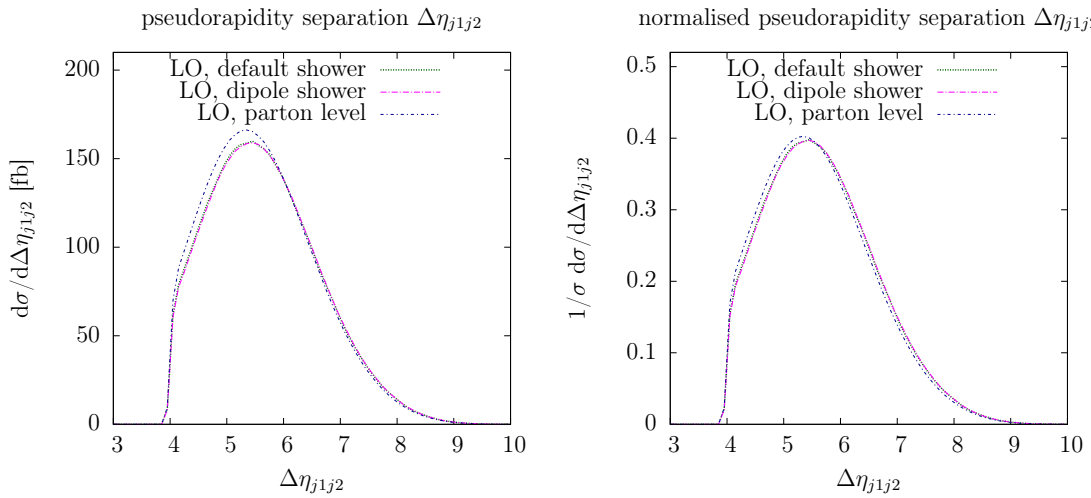

Figure 6.2: Distribution of the absolute value of the pseudorapidity difference of the two hardest jets. In the left plot, all graphs are normalised to their respective cross section while in the plot on the right, the graphs are normalised to unity.

The dipole shower generates harder jets than the default shower, which is especially visible in the tail region. Here, the distribution of the dipole shower complies with the LO parton level result while the default shower lies below.

In the left plot in Figure 6.2, the pseudorapidity separations of the tagging jets are plotted. The right panel shows the same distribution, but here each of the graphs was normalised to unity to enhance the visibility of the shape alteration. Both shower implementations tend to lose more events with lower pseudorapidity separations than with higher ones. The explanation for this behaviour is found within the stringent cut on $\Delta\eta_{j1j2}$: Shower-initiating partons in the hard matrix element which are close to the cut border have a higher probability to result in a situation after the shower, which is cut away.

On the other hand, migrations into the other direction can also happen. An event with a pseudorapidity separation $\Delta\eta_{p1p2} < 4$ of the partons in its matrix element can receive a kick by the shower, leading to an event topology with jets that are allowed to pass the analysis cuts. To assess if the loss or the gain of such migration effects predominates, both effects have to be quantified. The amount of gained events can be enquired by accessing the information of the parton kinematics in a run with cuts as described in Section 5.1. For each event that passes the analysis cuts, not only the post-shower jets are histogrammed but also the corresponding matrix element kinematics. If the partons had not passed the analysis cuts, but the jets do, the event can be considered as gained by the shower.

To quantify the loss of events, another strategy needs to be followed. A new simulation needs to be done with generation cuts set equal to the former analysis cuts (i.e. (5.1) to (5.5) applied to the hard partons). In this run, the analysis cuts are completely inclusive so that every possible post-shower configuration is

	Default shower		Dipole shower	
Observable	Loss	Gain	Loss	Gain
$\eta_{j1} \cdot \eta_{j2}$	2.3%	0.3%	1.6%	0.2%
$\Delta\eta_{j1j2}$	2.6%	2.4%	2.1%	3.2%
m_{j1j2}	7.1%	5.4%	6.5%	6.0%

Table 6.2: Fractions of events that are lost and gained by the shower algorithm. These are defined by normalisation of the respective cross sections in the curves of Figure 6.3 to the cross section present after the shower with cuts as described in Section 5.1.

histogrammed. If the generated jets are outside of the former analysis cuts, the event would have been lost within the normal setup.

Comparing the resulting histograms in regions which are forbidden by the original analysis cuts of (5.1) to (5.5), conclusions concerning the net loss or gain can be drawn differentially in each variable. Especially interesting observables to investigate here are the ones which are related with the VBF selection cuts, namely pseudorapidity separation, pseudorapidity product and invariant mass of the tagging jets, as experience has shown that these are heavily influenced by shower effects.

The results for the observables concerning pseudorapidity characteristics are shown in Figure 6.3 for the default shower. The "gain" curves, as defined above, comprise all hard matrix elements which are found to be in accordance with the applied analysis cuts after the shower. In contrast, the "loss" curves are those where the hard matrix element fulfils the analysis cuts, but which are modified by the shower in a way so that they move out of the allowed kinematical region.

The magnitude of the effect is still small in both cases and of the order of a few percent, depending on the examined observable and shower. The percentage of lost and gained events, defined as lost and gained cross sections normalised to the total cross section after the shower, is shown in Table 6.2.

When examining the distribution of $\eta_{j1} \cdot \eta_{j2}$ in Figure 6.3, it is obvious that an appreciable number of events is lost because it shows jets in the same detector hemisphere after the shower. The distribution of lost events peaks at a value between $2 < \eta_{j1} \cdot \eta_{j2} < 4$, depending on the shower algorithms used. Such a prominent peak away from the cut border is a strong hint for a behaviour which not only moderately modifies the kinematical structure of the underlying hard matrix element but rather reshuffles the event topology. A glance at the pseudorapidity separation $\Delta\eta_{j1j2}$ of the lost events hardens the suspicion. The distribution of $\Delta\eta_{j1j2}$ is split into two distinct regions: A narrow peak towards the cut border of $\Delta\eta_{j1j2} = 4$ and a broader part with a local maximum around $\Delta\eta_{j1j2} = 0.7$, a value which corresponds to the cone parameter in the jet algorithm that was used.

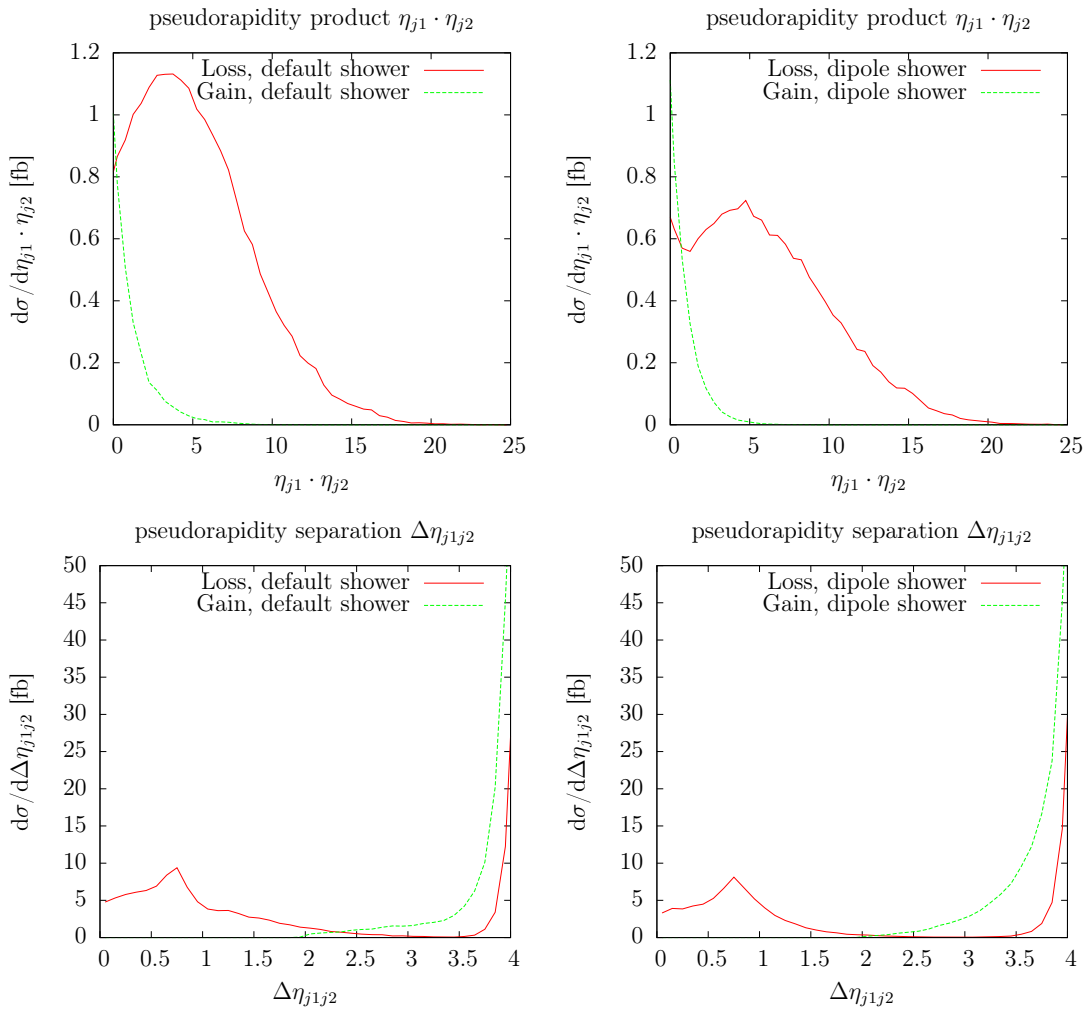

Figure 6.3: Gain and loss of events, plotted differentially in the pseudorapidity related observables $\Delta\eta_{p1p2}$ and $\eta_{j1} \cdot \eta_{j2}$. An event is defined as gained if its hard matrix element would pass the generation cuts, but not the analysis cuts. Contrariwise, an event is defined as lost if its hard matrix element passes the analysis cuts, but its showered state does not. The left row of plots shows results obtained with the default shower implementation while in the right row, dipole shower results are shown.

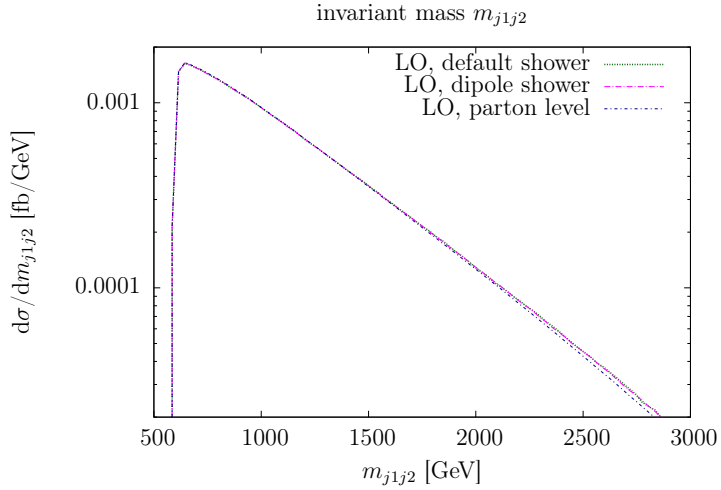

Figure 6.4: Dijet invariant mass distribution of the tagging jets.

The observed behaviour of reshufflings in observables concerning the two tagging jets can be easily explained by the fact that these are observables which are vulnerable to the ordering of the jets in transverse momentum. It is clear that if the two hardest jets emerge from the same parton in the primary matrix element, this ordering is disturbed. The fact that such a situation usually results in two jets close in the legoplot plane also explains the peak at $\Delta\eta_{j1j2} = 0.7$.

In Figure 6.3, both shower implementations show qualitatively the same characteristics, but differ quantitatively. The dipole-showered results suffer less from a reordering of jets, but seem to have a larger possibility to modify the directions of the primary partons. Looking at the $\Delta\eta_{j1j2}$ distributions, the number of gained events by the shower is larger for the dipole shower than for the default shower.

The dijet invariant mass distribution of the tagging jet pair, plotted in Figure 6.4, shows a deviation in the high-mass range. The LO matrix element produces less events in this tail region. The question arises, if the shower itself produces these high mass clusters or if this is a side effect of events migrating over cut borders in another observable, leading to cross correlations.

To clarify this, let us imagine high mass diparton invariant masses would occur strongly peaked in starting configurations with parton pseudorapidity separations just below 4. As we have seen, such a configuration is likely to finish the shower with jets of $\Delta\eta_{j1j2} > 4$. Even if the shower modifies the invariant mass present in the partonic configuration only negligibly, such a correlation would lead to a strong enhancement in the m_{j1j2} distribution.

Figure 6.5 shows that the deviation does not stem from such a cross correlation. There, the dijet invariant mass distribution is depicted as calculated within the leading-order approximation together with the partons in the hard process. The latter were collected as the "gain" graphs described within the previous sections, i.e. for each showered event which passes the analysis cuts, the partonic observable was histogrammed using the kinematics in the underlying hard matrix element. The

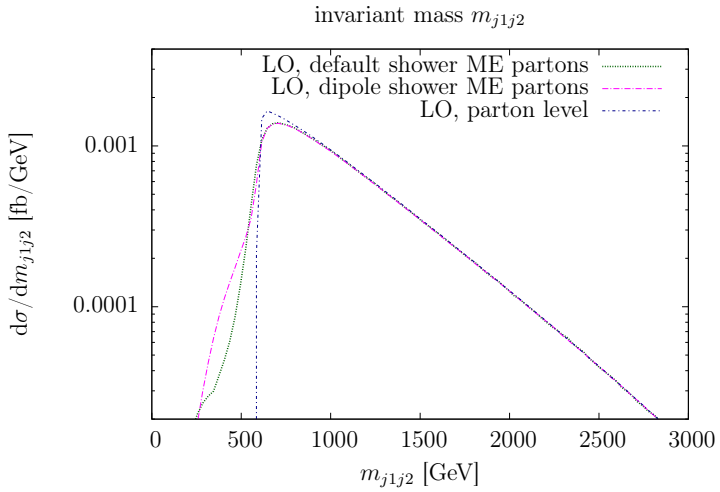

Figure 6.5: Dijet invariant mass distribution for the partons in the hard matrix element.

three graphs are indistinguishable in the high-mass region, indicating that the departure of the showered calculations from the leading-order prediction, at least to some extent, stems from the shower.

Distributions of the gained and lost events in the dijet invariant mass are displayed in Figure 6.6. The graphs exhibit the same characteristics that were already present in the rapidity separation of the tagging jets. The distribution of the lost events is a superposition of two peak structures, the lower one resulting presumably from events where the tagging jets after the shower stem from the same parton. Again, the dipole shower crops up as being somewhat less affected by these kinds of splittings than the default shower implementation.

6.2 Additional jets

In the LO plus parton shower calculation, the third hardest and softer jets are solely generated by the shower algorithm, although the evolution of parton showers is of course heavily influenced by the colour structure of the matrix element. Differences in the shower algorithms show up in these higher order emissions. The quality of shower approximations can be compared by checking their predictions against the results from the parton-level NLO calculation, which includes the possibility of three jets at fixed order.

The first thing that can be noticed when regarding the transverse momentum and rapidity distributions of the third jets in Figure 6.7 is that the three-jet cross sections of the approximations differ considerably. The dipole showered calculation has the largest cross section, followed by the NLO results. The default shower yields the lowest cross section.

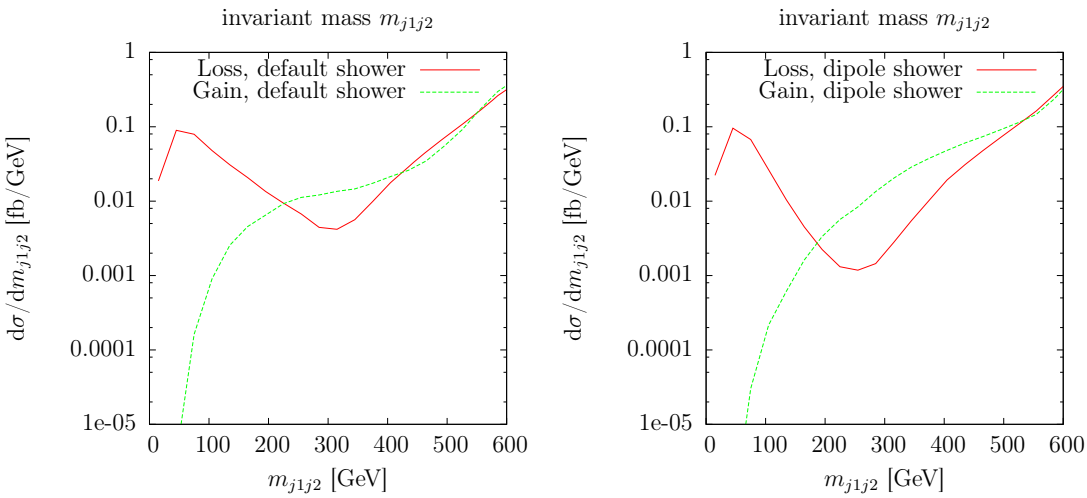

Figure 6.6: Gained and lost events by the cut on a minimum invariant mass of the tagging jets. The left panel shows the results of the default-shower calculation. For the graphs in the right panel, the dipole shower was employed. The default shower loses more events than the dipole shower, especially in the central region with $100\,\text{GeV} < m_{j1j2} < 300\,\text{GeV}$.

Note that in [99], where a similar calculation with the default shower was done, but with a decaying Higgs boson into a $\tau^+\tau^-$ pair, the situation is different. There, additional cuts on the jet-τ legoplot separation influence the calculations unequally, leading to different proportions of the three-jet cross sections.

To explain the different cross sections of the two shower algorithms in the case at hand, the almost complete phase space coverage of the dipole shower has to be noted [62]. This results in a higher chance of hard emissions at a relatively large angle than what can be accomplished by the default shower. As only emissions sufficiently far away from the primary parton can be resolved separately by the jet algorithm, the dipole shower therefore has a larger three-jet cross section than the default implementation.

The different shapes of the rapidity distributions in Figure 6.7 can be explained by the fact that shower emissions tend to fill the phase space regions between colour-connected partons. This behaviour is sketched in Figure 6.8. Together with the distinct topology in weak-boson-fusion events with widely separated tagging jets, this typically results in third jets with large absolute rapidity values.

As the Higgs boson resides in the gap between the tagging jets, the third jets in a shower simulation should end up further away from it than predicted by the NLO calculation. In Figure 6.9, the distribution in the absolute value of this separation

$$\Delta y_{hj3} = |y_h - y_{j3}| \tag{6.1}$$

is plotted. As expected, the shower curves peak at larger rapidity separations. However, in the vicinity of the Higgs boson, the two shower algorithms lead to the same differential cross section. As the Higgs boson is supposed to be central in the

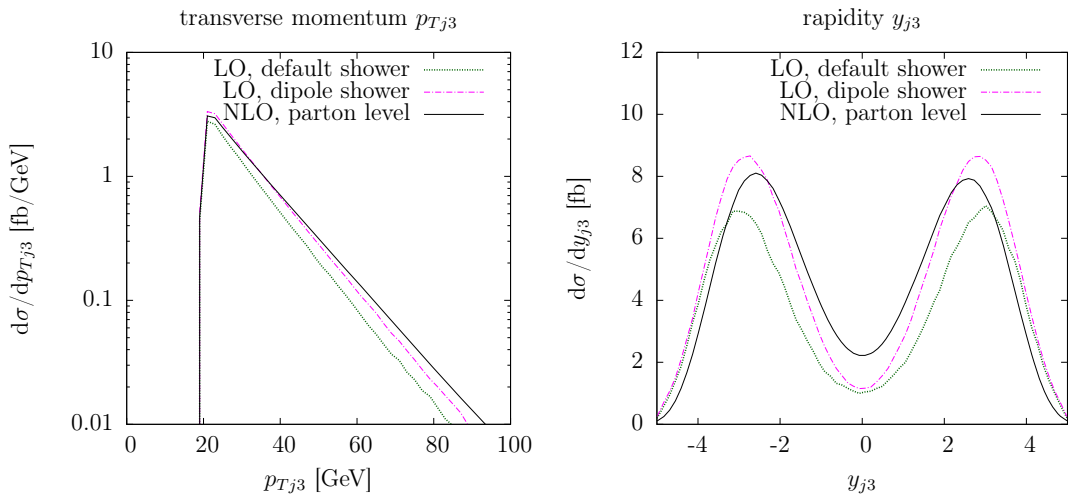

Figure 6.7: Transverse momentum and rapidity distributions of the third hardest jet.

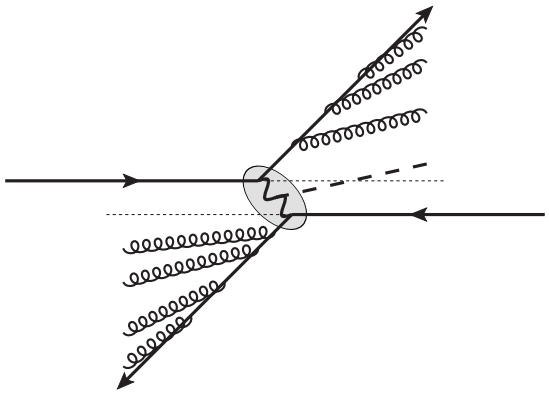

Figure 6.8: Shower emitting into the angles between colour-connected partons. The grey blob delimits the hard matrix element from the shower.

detector, the situation is comparable to the rapidity graph in Figure 6.7, where in the central region the shower algorithms also coincide.

The rapidity offsets of the third jet to the tagging jets in Figure 6.10 reveal that both showers in general react very differently. When employing the default shower, the third jet is slightly more frequently close to the hardest jet. With the dipole shower, the situation is reversed and an abundance of events is generated with the third jet in the proximity to the second hardest jet.

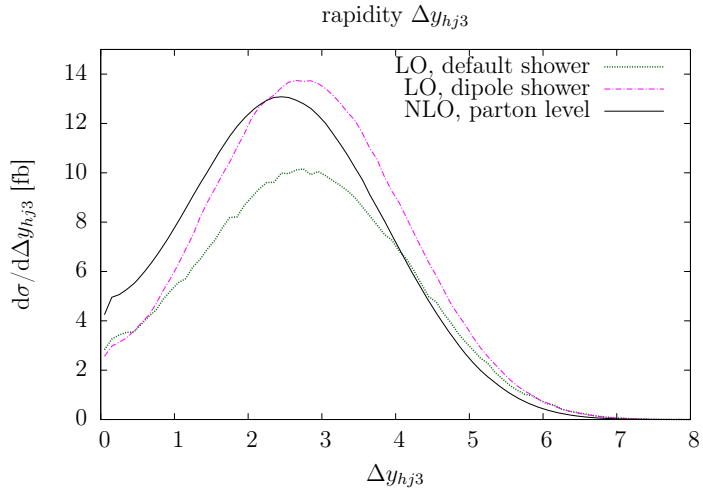

Figure 6.9: Δy_{hj3} distribution of the shower algorithms compared to the NLO result. The NLO approximation produces more partons in the proximity of the Higgs boson than any of the showers.

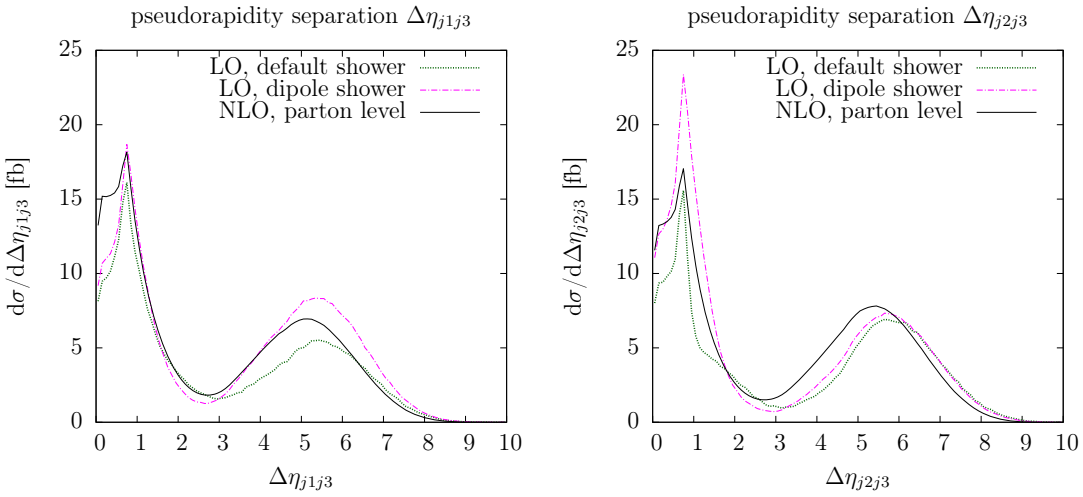

Figure 6.10: Pseudorapidity separation distribution of the tagging jets from a third jet.

6.3 IF splitting schemes

As described in Section 4.5, it is unclear how the transverse momentum generated by initial-final dipole splitting kernels needs to be distributed. There is no first principle that guides this choice. The two options implemented in Herwig++ are

- The non-collinear scheme: The transverse momentum is evened out between the initial-state emitter and the final-state emission. This scheme is used by default.
- The collinear scheme: All transverse momentum is generated in the final-state only and distributed to emission and spectator. The emitter receives no p_T at all.

For a single emission, the collinear and non-collinear schemes only differ by a boost, which is applied after termination of the parton shower during the realignment phase anyway in order to render the incoming hadrons collinear to the beam pipe. For more than one emission, however, the results of the two splitting schemes can differ significantly.

Obviously, the non-collinear scheme generates more transverse momentum for the incoming hadrons than the collinear scheme. This affects the magnitude of the realignment boost and thereby, in principle, also all event observables. However, the distributions are in general very stable when switching between the two schemes. Especially for the two tagging jets, there is no visible difference between the schemes in Figure 6.11, where the transverse momenta and rapidities of the tagging jets are plotted.

Also visible in Figure 6.11 are the rapidity and transverse momentum distribution of the third jet. Note that the three-jet cross sections in the two splitting schemes differ. In the y_{j3} plot, they differ solely in the outer regions, where the third jet is supposed to be close to one of the two tagging jets. A similar behaviour can also be investigated in the legoplot separations of the third jet to the first and second jet in Figure 6.12. Obviously, distributions are modified mostly in regions with adjacent jets.

Depicted in Figure 6.13 are the pseudorapidity separations of the tagging jets and the third jet. There are larger separations within the non-collinear scheme. As there is more transverse momentum produced for the initial-state hadrons when the non-collinear scheme is applied, the realignment boost has a larger magnitude in this case. Examining Figure 6.13, it can be speculated that this boost has the tendency to shift the event topology towards larger rapidity separations.

The result of this behaviour stands out more prominently when looking at the azimuthal angle separations of the third jet to the leading ones in Figure 6.14. In the plots, not only the two different splitting schemes are shown but also the default shower and NLO results are given as a reference. The observable range can be divided into two parts: The outer and inner regions with $|\Delta\phi_{jj}| > D_{\text{cone}}$ and $|\Delta\phi_{jj}| < D_{\text{cone}}$, respectively.

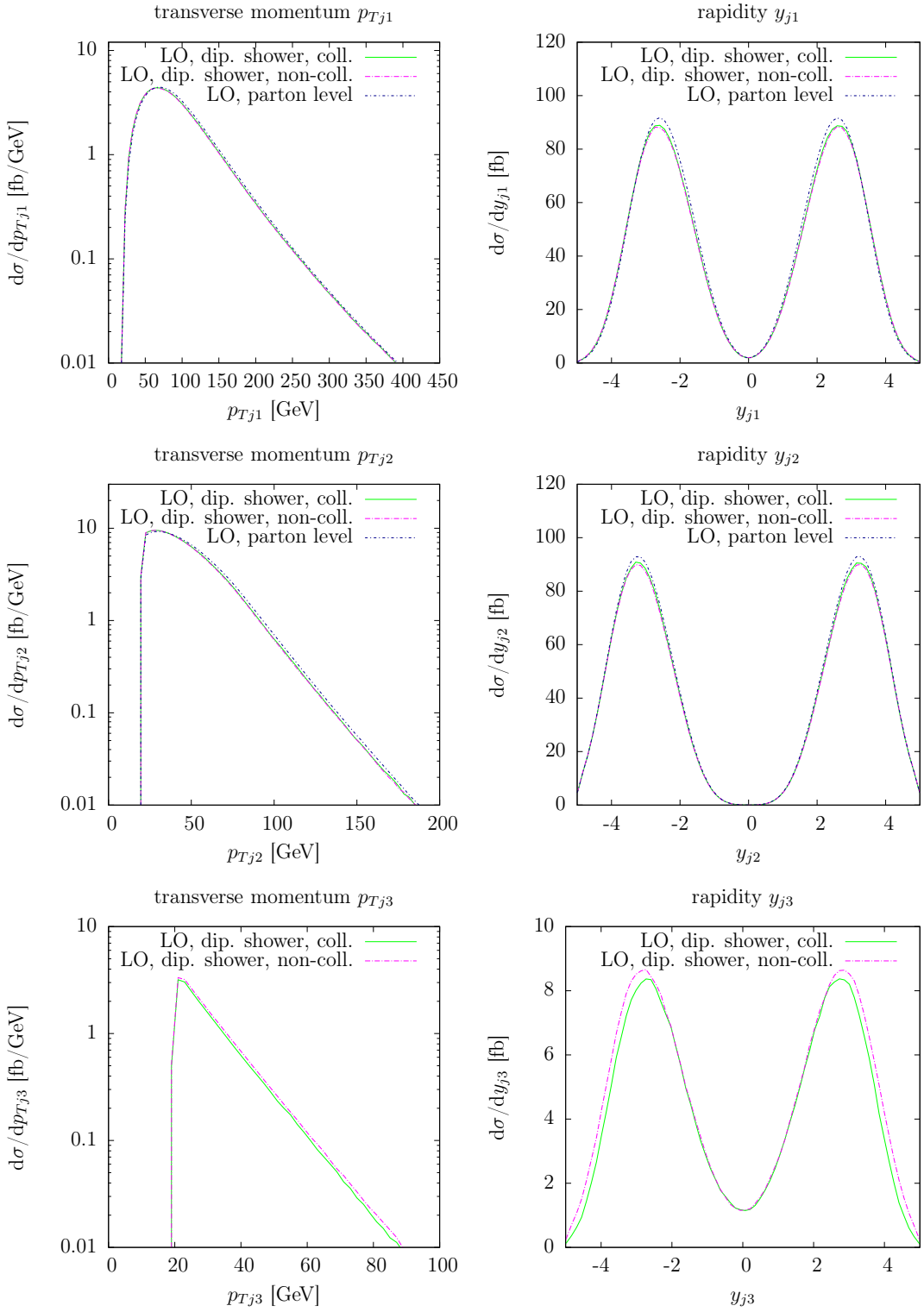

Figure 6.11: Transverse momentum and rapidity distributions of the three hardest jets.

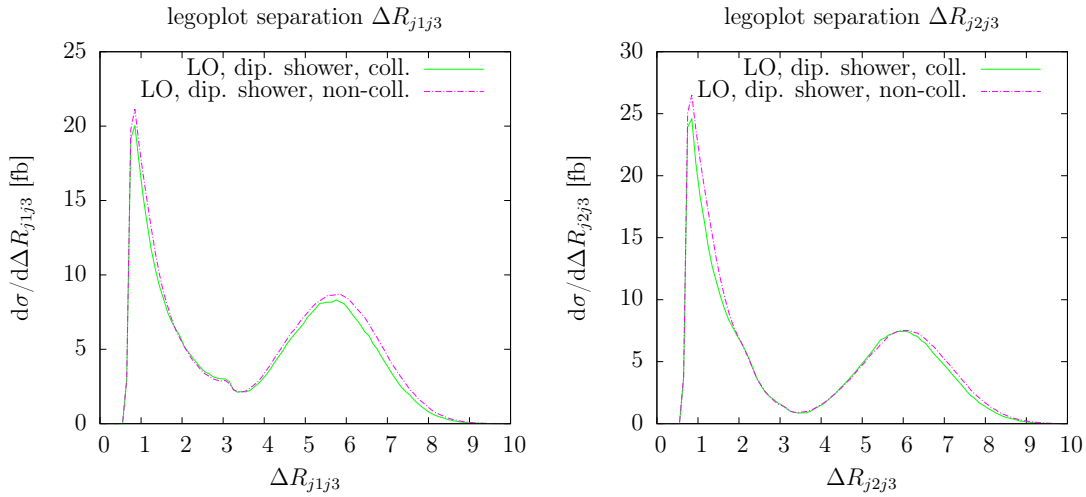

Figure 6.12: Legoplot separation distribution of the third hardest jet and the two tagging jets.

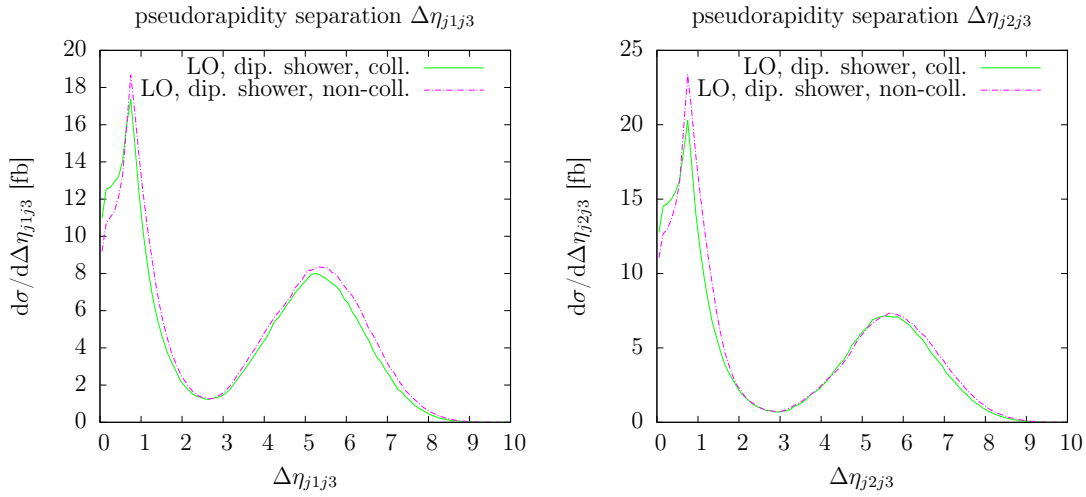

Figure 6.13: Pseudorapidity separation distributions of the third hardest jet and the two tagging jets.

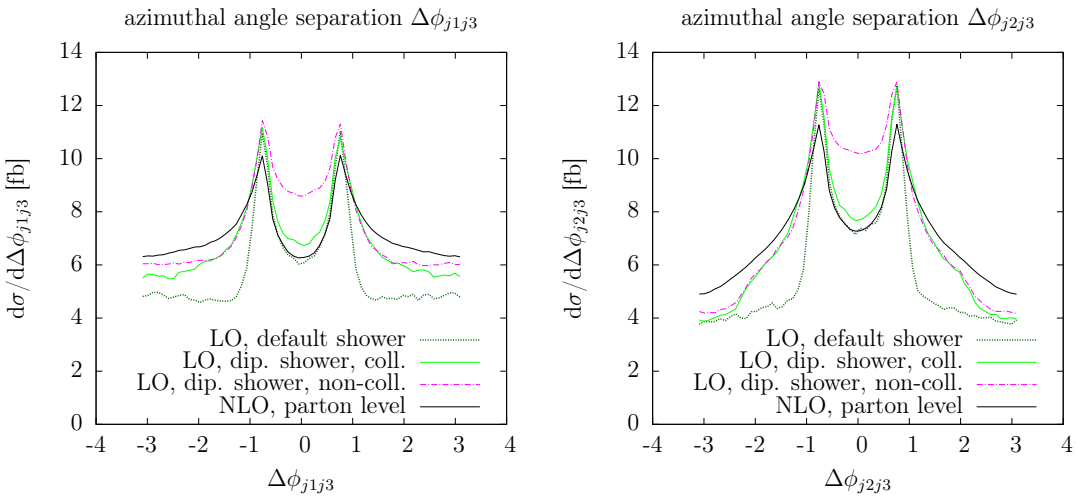

Figure 6.14: Azimuthal angle separation distribution of the tagging jets and the third jet.

In the outer region, the chosen splitting scheme does not show much of an influence. The default shower, however, undershoots the dipole shower by far there. This can be explained by the restricted phase space of the default shower. With an increasing azimuthal angle separation, the kinematics tend to move away from the region where the default shower is allowed to emit into.

In the inner region, default shower and the dipole shower with the collinear scheme lead to almost the same results and are much closer to the NLO curve. Using the dipole shower with the non-collinear splitting scheme deviates much from this expectation and results in substantial more emissions in the central region.

The explanation of this behaviour is tied closely to the jet algorithm. Radiation close to the tagging jets will tend to be assigned to them, while only radiation at wider angles will be defined as a separate jet. The realignment boost does not leave distances in the legoplot plane invariant, so that an emission which would have been absorbed by one of the tagging jets may end up with a larger separation, forming its own jet.

A side effect of this behaviour is a modification of the p_T distributions of the tagging jets in the non-collinear splitting scheme if the third jet lies in the central region of $\Delta\Phi_{jj}$. This is depicted in Figure 6.15. It is clearly visible that there is a tendency in the non-collinear splitting scheme to produce more soft tagging jets if a third jet is nearby, while in the high p_T region, both splitting schemes coincide. These soft jets are just the jets which have lost p_T by radiation that is forming its own jet in the non-collinear scheme. In the collinear scheme on the other hand, the radiation is recombined into the tagging jets so that they do not lose transverse momentum, as the effects of the realignment boost are much smaller.

From Figure 6.14, it looks like the collinear scheme seems to be the correct way to treat initial-final splittings, as it deviates less from the NLO prediction. However, this cannot be concluded without comparison to experimental data.

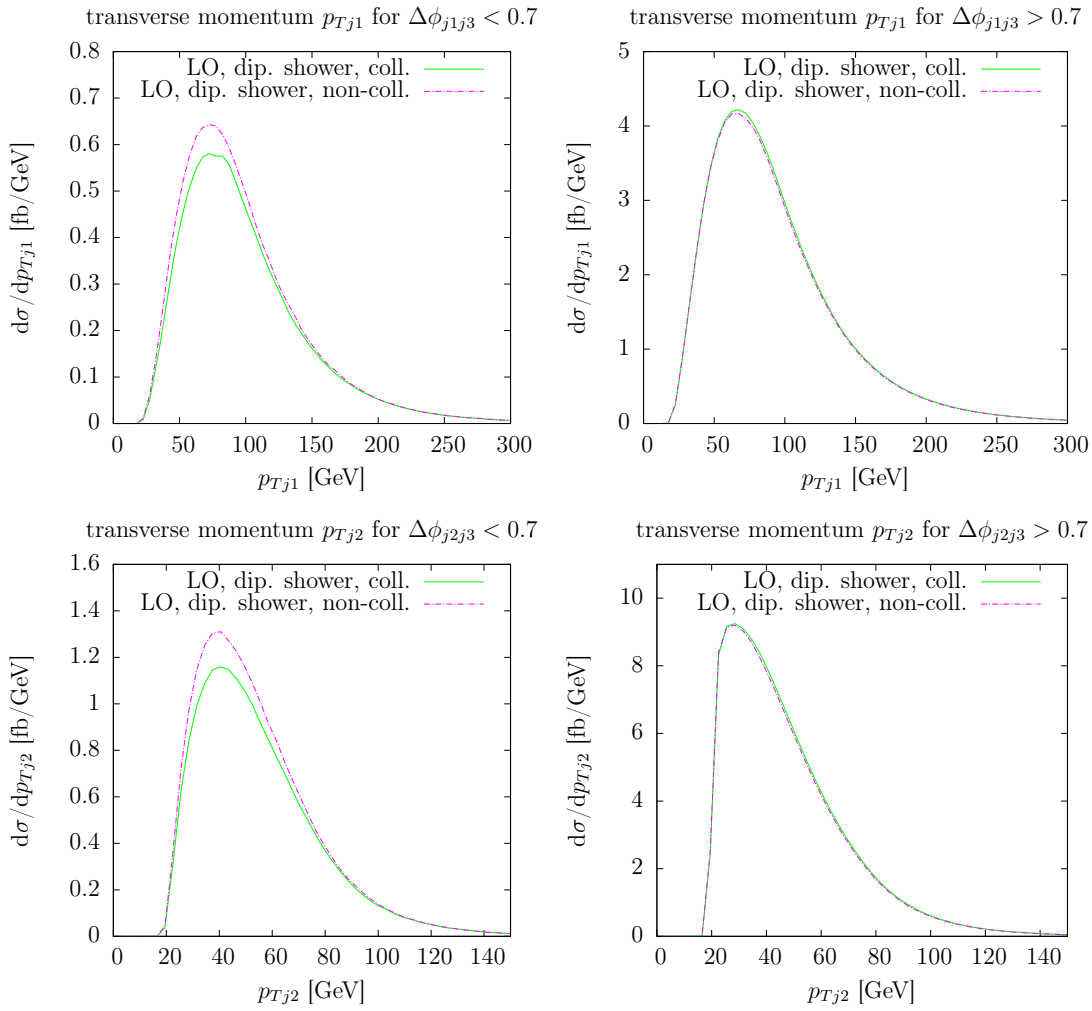

Figure 6.15: Transverse momentum distributions of the tagging jets if the third jet is close (left column) in azimuthal angle separation $\Delta\phi_{jj}$. The right column shows the cases where the third jet is either not existent or has a larger $\Delta\phi_{jj}$ separation to the relevant tagging jet. The shapes are identical if the third jet is far away.

6.4 Summary of leading-order effects

Summarising the shower effects that arise within the LO showered calculation, it has to be mentioned that the jets already present within the matrix element calculation are hardly affected. This is especially true for the dipole shower. The default shower leads to a slight modification of the transverse momentum distribution of the hardest jet. In the high-p_T region, it fell below the fixed order prediction. The total cross section is affected by events migrating over cut borders.

The distributions of the third hardest jet, however, are very dependent on the details of the shower implementation. The dipole shower has proven to result in third jets with a larger transverse momentum than the default shower. In addition, the dipole shower produces a larger three-jet cross section than the default shower, which is closer to the NLO parton level prediction. Due to the better phase space coverage, the distributions of the dipole shower are closer to the NLO curves than the default showered results. However, there are regions where they do not comply completely. This is expected, as both showers are only correct within the regions of soft and collinear singularities, where the NLO calculation lacks predictivity.

The two different splitting schemes of the dipole shower show almost no influence on the most observables that were examined. When investigating the azimuthal angle separations of the tagging jets and the third jet, a prominent discrepancy shows up between the two. The non-collinear scheme leads to strongly increased population of the central regions of $\Delta\Phi_{j1j3}$ and $\Delta\Phi_{j2j3}$. This could be accredited to a combined effect of the realignment boost, leading to larger legoplot separations of the emissions, and the jet algorithm which could then resolve them as separate jets.

Chapter 7

NLO-matched Hjj production

After a discussion of effects occurring within a LO showered calculation in the last chapter, the current chapter focuses on the features arising in NLO matched calculations. Special care will be taken to work out the differences between the MC@NLO and POWHEG matching schemes. The two schemes were described in Section 2.4.2. The basic difference is that in POWHEG, the shower algorithm carries out the real emissions and therefore, only matrix elements with Born kinematics need to be showered. In MC@NLO, both born and real-emission kinematics matrix elements are showered, but no adapted Sudakov form factor is needed to handle the real emissions. Within the Matchbox framework, both schemes can be carried out exactly with the dipole shower. Comparisons with the results from the LO plus dipole shower section will be drawn wherever necessary.

7.1 Tagging-jet properties

The influence of the MC@NLO and POWHEG matching schemes on the tagging jet kinematics is examined within this section. As seen in the previous chapter, the pure shower does not show a large impact here. As the LO approximation already describes the shapes of the observables with a reasonable precision, only minor alterations are expected when incorporating the NLO corrections within the shower.

Transverse momenta and rapidities of the tagging jets are shown in Figure 7.1. The differential distribution of σ/σ_{NLO} is plotted in Figure 7.2. Within MC@NLO,

Matching scheme	Cross section σ[fb]
MC@NLO	422.1
POWHEG	422.4

Table 7.1: Cross sections obtained with the different matching schemes.

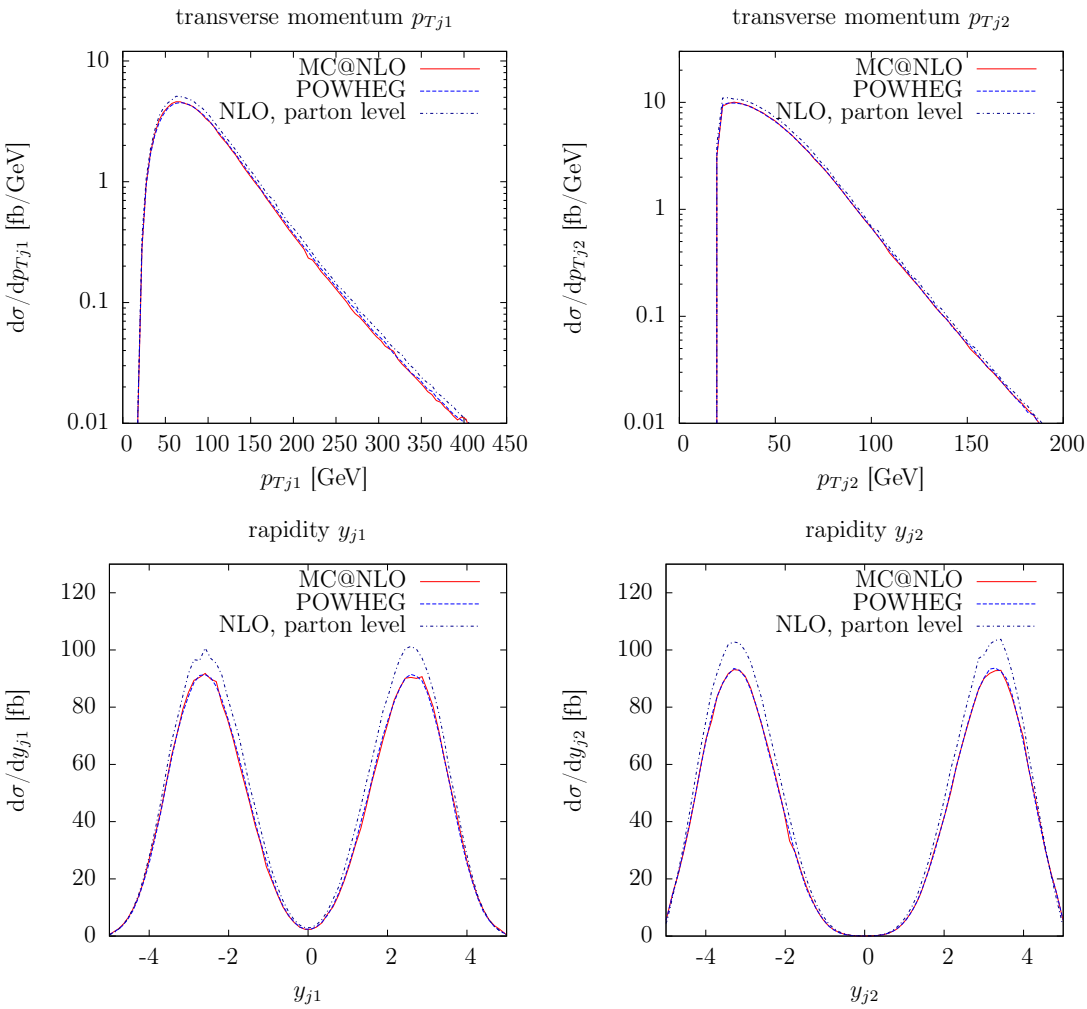

Figure 7.1: Transverse momentum distributions (upper row) and rapidity distributions (lower row) of the two tagging jets.

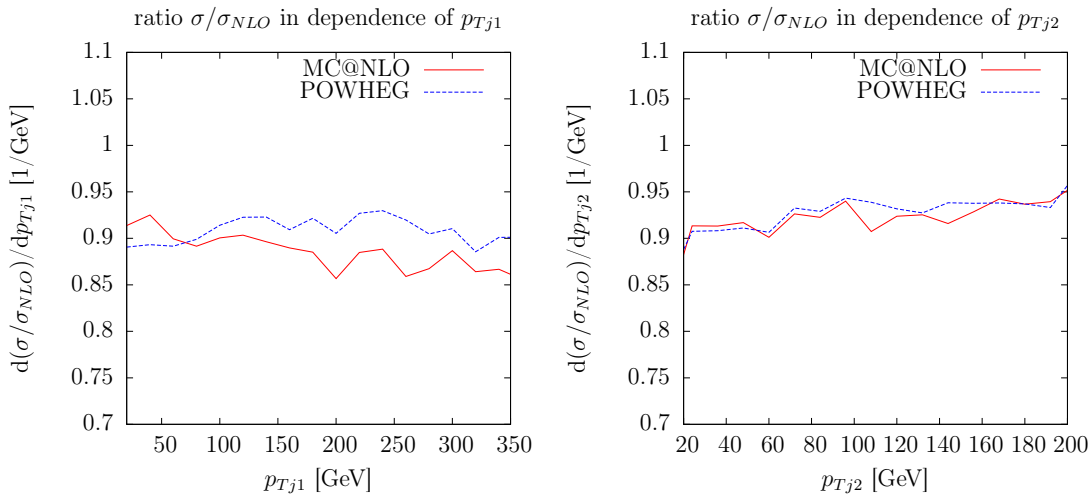

Figure 7.2: Differential distribution of σ/σ_{NLO} in dependence of the tagging jet transverse momenta.

more transverse momentum is drained from the hardest tagging jet than within POWHEG. As with the LO showered results, migration effects lead to a decreasing cross section after the shower. The POWHEG matching scheme shows about the same cross section as MC@NLO for the case at hand (see Table 7.1). As expected, both matching schemes hardly affect the shape of the distributions.

As motivated in Section 6.2, the colour structure of vector boson fusion enforces shower emissions mainly in regions between the beamline and leading partons in the hard matrix element. The result is a marginal shift of the rapidities of the leading jets to larger values as compared to the unshowered calculation in Figure 7.1, where the rapidities of the tagging jets are depicted together with their transverse momenta.

In Figure 7.3, the pseudorapidity separation distribution is plotted. Examining the right panel, where the distributions are normalised to unity, it is noticeable that, for both matching schemes, the peak is shifted to slightly larger values of $\Delta\eta_{j1j2}$ by the parton shower, which is also a consequence of the shower emission topology.

The transverse momentum distribution of the third jet, which is plotted in Figure 7.4 alongside the corresponding rapidity distributions, reveals POWHEG to produce softer and in general less additional radiation than MC@NLO. In W^+W^-jj production via vector boson fusion, the same behaviour was described in [100], where the hard matrix element was interfaced with POWHEG-BOX [101] to PYTHIA. This seems to be a contradiction to some previously published results from other groups [102, 103], which will be reviewed in the following.

In [102], which describes POWHEG matching in Higgs production via gluon fusion together with a DGLAP-based parton shower, the Higgs transverse momentum was examined. At LO, the transverse momentum vanishes due to momentum conservation, but at NLO, the additional jet recoils against the Higgs, leaving it

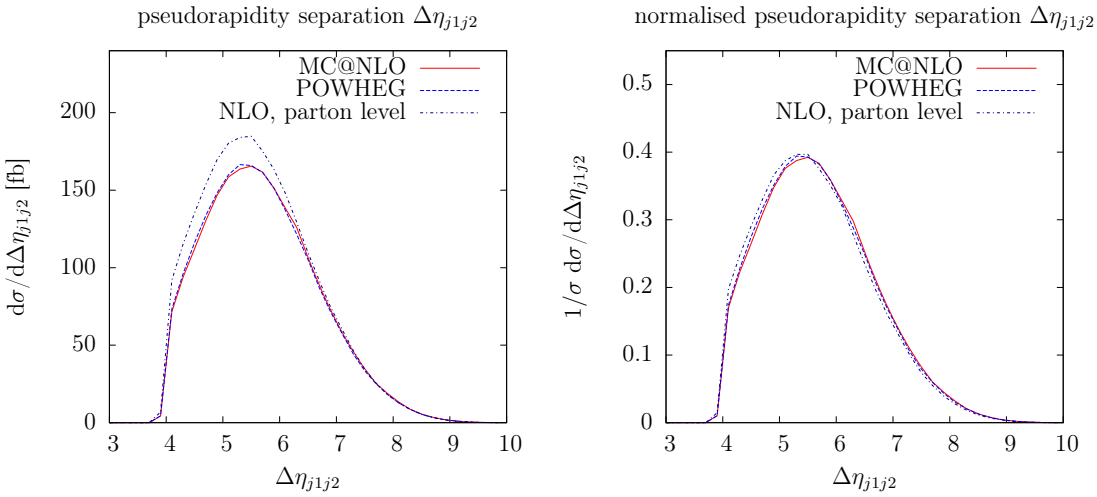

Figure 7.3: Distribution of the absolute value of the pseudorapidity difference of the two hardest jets. In the plot on the right, the graphs are normalised to unity.

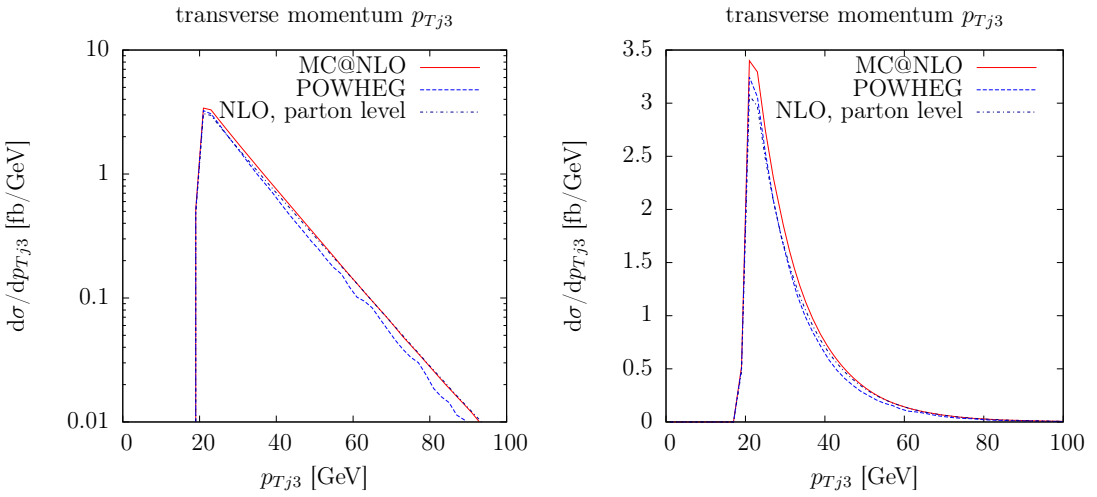

Figure 7.4: Transverse momentum distribution of the third hardest jet. The left and right panel show the same distribution, the former on a logarithmic scale and the latter on a linear scale.

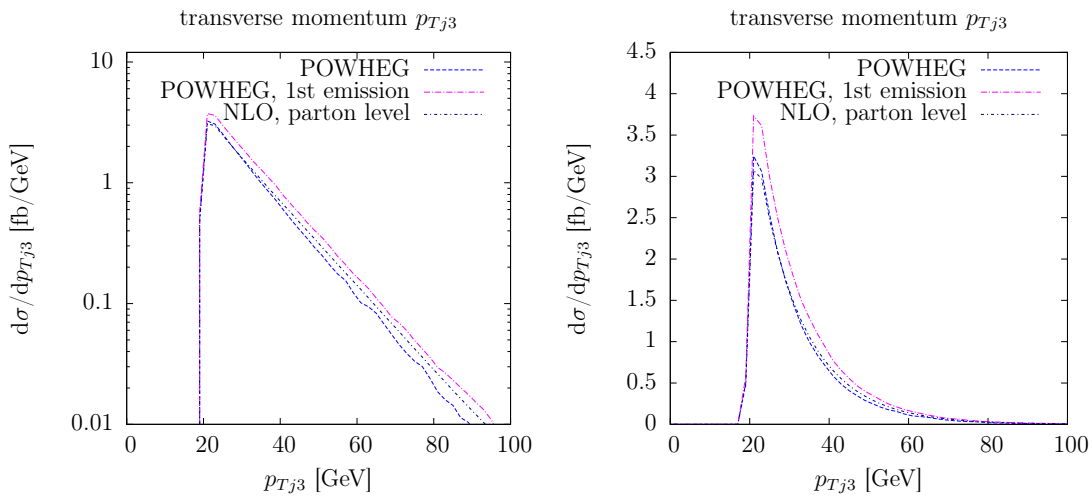

Figure 7.5: Transverse momentum distribution of the third hardest jet. Analysing the curves only with the POWHEG emission reveals that subsequent radiation is responsible for a substantial drop of the differential cross section in the whole p_T range.

with a non-zero p_T. In the publication, it was shown that the generated transverse momentum in the POWHEG scheme was larger than both the MC@NLO and plain NLO results in the high p_T region. It was advocated that this behaviour is a result of NNLO terms that arise when exponentiating the $\bar{B}$ function (2.45) with the parton shower. For large transverse momenta of the Higgs boson, the NLO and matched calculations disagree by terms

$$\frac{\bar{B}(\Phi_{Rad})}{B(\Phi_{Rad})} = 1 + \mathcal{O}(\alpha_S). \tag{7.1}$$

It was also demonstrated in [102] that the NNLO result supports the POWHEG prediction.

The same behaviour was also seen in [103], where, amongst others, also results from gluon fusion processes are shown, which were obtained using a dipole shower. Though, the authors of [103] oppose the previous study [102] in the interpretation, holding the unrestricted phase space of the POWHEG shower responsible.

Reviewing these previous results, the reduced three-jet cross section in the POWHEG matching scheme in W^+W^-jj and the Hjj production case at hand is indeed a surprise at first glance. However, in both previous studies [102] and [103], the observable was an inclusive quantity. In VBF processes on the other hand, additional radiation together with the phase space cuts which are applied to the event may have a large influence just by purely kinematical effects. In Figure 7.5, the p_{Tj3} distribution is plotted in the POWHEG matching scheme without any additional emissions. It shows that the three-jet differential cross section is much larger if only one emission is permitted. The explanation for the fully showered

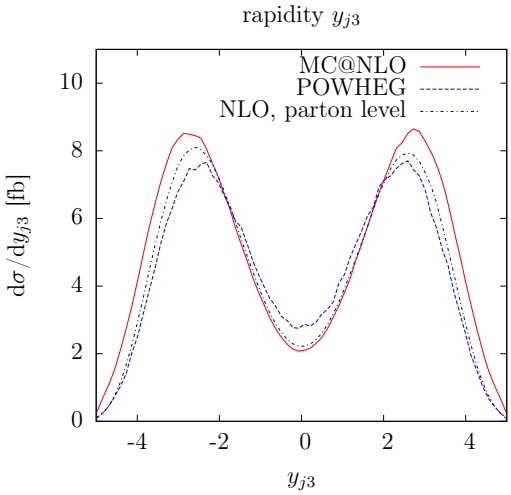

Figure 7.6: Rapidity distribution of the third hardest jet.

POWHEG results undershooting the NLO distribution is then simply found in the interplay of shower radiation and cuts, leading to more events failing the cuts.

The rapidity of the third hardest jet is plotted in Figure 7.6. Within the central rapidity region, the POWHEG prediction overshoots the NLO results. If the third jet is emitted with a rapidity around $y_{j3} = 0$, the situation corresponds to a hard wide-angle splitting and as such, is a realm where the NLO approximation can be trusted. However, the evolution kernel R/B in the POWHEG Sudakov form factor gives rise to non-leading logarithmic terms, which may result in substantial differences when compared to the NLO parton level result.

The MC@NLO matching scheme, on the other hand, is following the predictions of the NLO calculation in the central region. Within MC@NLO, the production of third jets can either happen by starting with a real-emission matrix element or by additional radiation on top of a hard matrix element with Born kinematics. The latter formally also introduces higher order effects away from the soft and collinear regions. In the case of the rapidity of the third hardest jet in the central region, they seem to have little impact however.

Opposed to the central dip regions of y_{j3}, the peak regions correspond to collinear splittings, as the tagging jets also peak in the same rapidity regions. The separation of collinear and hard splitting regions can be accentuated even more by considering the distribution of

$$y^*_{j3} = y_{j3} - \frac{1}{2}\left(y_{j1} + y_{j2}\right), \tag{7.2}$$

which gives the rapidity difference of the third jet relative to the mean rapidity of the tagging jets [104]. This way, the dependence on the longitudinal boost of the centre-of-mass frame of the colliding partons can be circumvented.

For the case at hand, y^*_{j3} is depicted in Figure 7.7. Just as in the y_{j3} distribution in Figure 7.6, the MC@NLO and NLO results agree in the central region

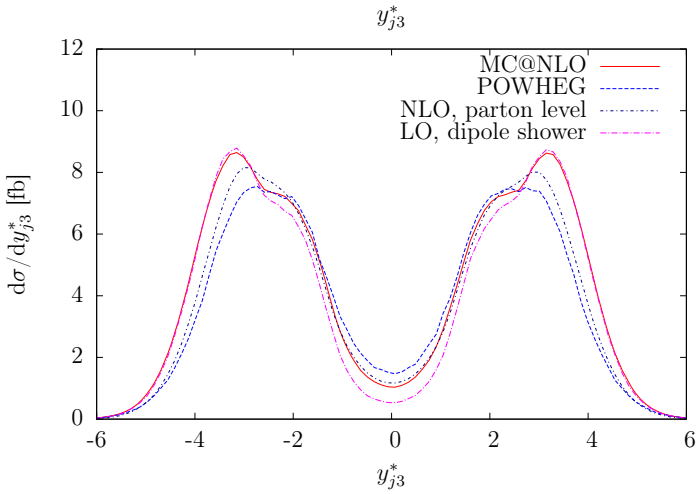

Figure 7.7: Distribution of the y^*_{j3} observable as defined in (7.2).

characterised by hard splittings, while POWHEG shows too much activity. The LO dipole-showered output is also plotted, allowing for a comparison to results gained within the soft/collinear approximation. Apparently, the possibility of starting from real-emission matrix elements within MC@NLO is already a large improvement in the region around $y^*_{j3} = 0$.

As with y_{j3}, also in Figure 7.7 the peak regions and their outward flanks correspond to regions where a collinear splitting occurred. These are regions where higher-order terms become large due to sizeable kinematical effects overcoming the smallness of the coupling constant. Here, the all-order expansion within the parton shower approximation should be trusted more than the fixed-order prediction. The MC@NLO result and the LO showered calculation show an indistinguishable behaviour here.

At the outward flanks of y^*_{j3}, POWHEG undershoots even the NLO prediction. Supposedly, this is the region where an abundance of real-emission partons lose p_T by additional shower emissions, so that they cannot be identified as jets anymore. The assumption is supported by Figure 7.4, where the transverse momentum of the third jet within the POWHEG matching scheme has shown to deviate from the NLO expectation by a steeper slope. POWHEG also exhibits less radiation over the whole p_T range, which is a clear indication of an even drain of transverse momentum by subsequent shower emissions.

In the normalised legoplot separations in Figure 7.8, the collinear splitting regions correspond to the narrow and, *cum grano salis*, also the wide peaks at legoplot separations of around 1 and 6. The depleted region in between is the region which is characterised by hard additional emissions. It is clearly visible that in the regions where the third jet is close to one of the tagging jets, the POWHEG matching scheme leaves the NLO distribution almost invariant. As POWHEG always starts from the three-jet real-emission configuration, the room for an enhancement of this region is expectedly small.

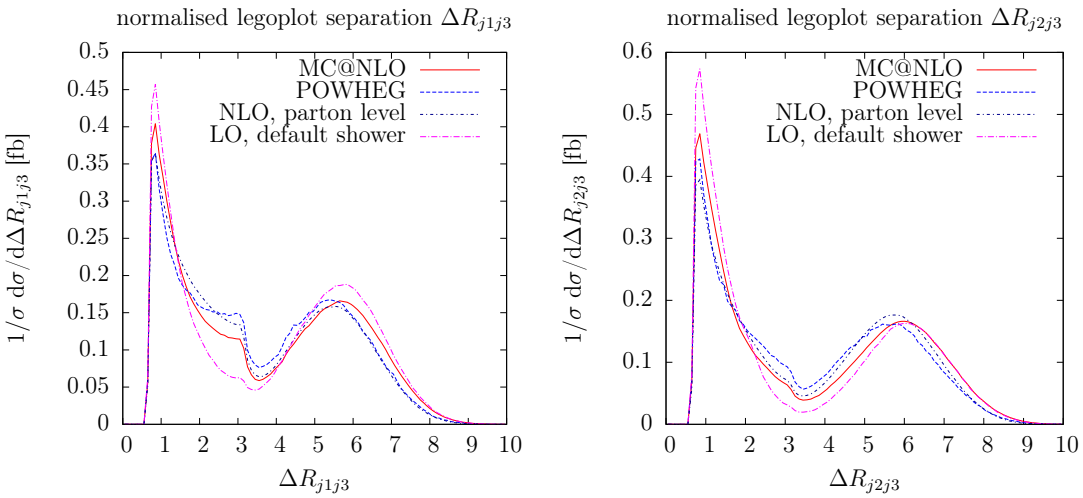

Figure 7.8: Distributions of the legoplot separations of the third jet to the hardest (left panel) and second hardest (right panel) jet. The edge at $\Delta R_{jj} = \pi$ arises because the azimuthal angle separation, which goes into ΔR_{jj}, gives only contributions up to that value.

Another important feature of the distributions in Figure 7.8 is that in the POWHEG scheme, the third jets tend to have larger legoplot separations from the tagging jets.

While Figure 7.8 shows that additional jets produced by the dipole shower are rarely radiated far away from the tagging jets, the MC@NLO matched results again show an intermediate behaviour with results closing in on the NLO predictions. Both within the area of radiation close to one of the tagging jets as well as in the hard wide-angle case, MC@NLO gives predictions much closer to the NLO distributions than the dipole shower alone.

The azimuthal separations in Figure 7.9 of the third jet to each of the tagging jets show a somewhat differing behaviour of the matching schemes especially in the central region. As a reminder, all results within the present section were gained using the non-collinear realignment scheme. The two realignment schemes of the dipole shower have shown very different results here as described in Section 6.3. There, the increase in the central region could be attributed to an increase of emissions which could be identified as separate jets.

In the matched case, POWHEG shows approximately the same activity than the NLO curve over the whole range of azimuthal angle separation. As shown before, the third jets within the POWHEG matching scheme also suffer from a p_T drain that decreases their resolvability. The result is comparable to what happens within the collinear splitting scheme. Also in the POWHEG scheme additional emissions get assigned to the tagging jets or not resolved at all. This then prevents the central regions of $\Delta\Phi_{j1j3}$ and $\Delta\Phi_{j2j3}$ to be filled.

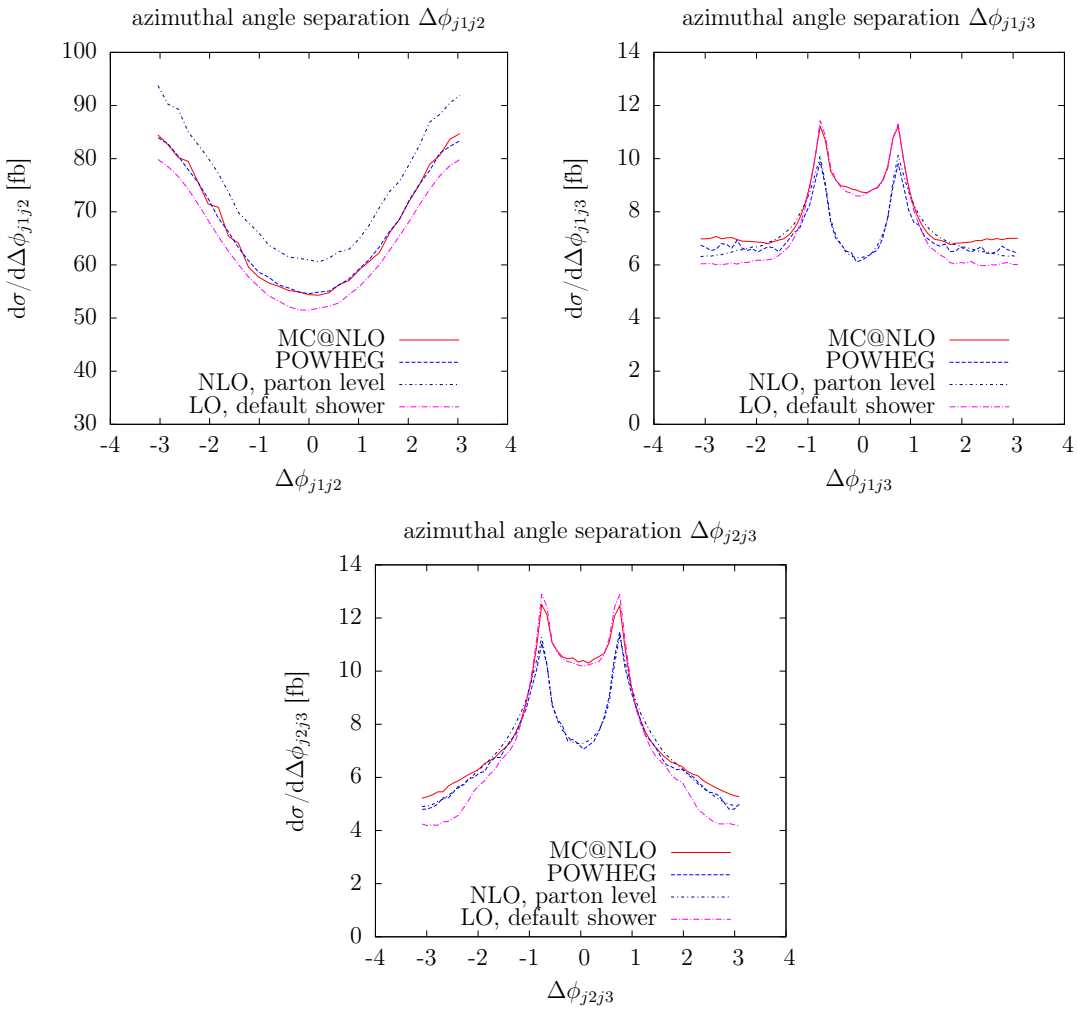

Figure 7.9: Azimuthal angle separation distribution of the tagging jets.

In the NLO case, MC@NLO yields the same distribution in the central region as the LO dipole showered calculation. Obviously, this is a region which is very much governed by shower and jet algorithm effects.

In the outer regions of $\Delta\phi_{j1j3}$ and $\Delta\phi_{j2j3}$, the MC@NLO curve shows an enhancement over the LO dipole showered result and is closer to the NLO prediction. As these outer regions in $\Delta\phi_{j1/2j3}$ are areas which correspond to a back-to-back situation with one of the tagging jets, it is expected to benefit from the matching.

7.2 K-factors

The corrections that arise within the matched calculation depend on the region of phase space that is considered. To bring out the differences of the matching schemes

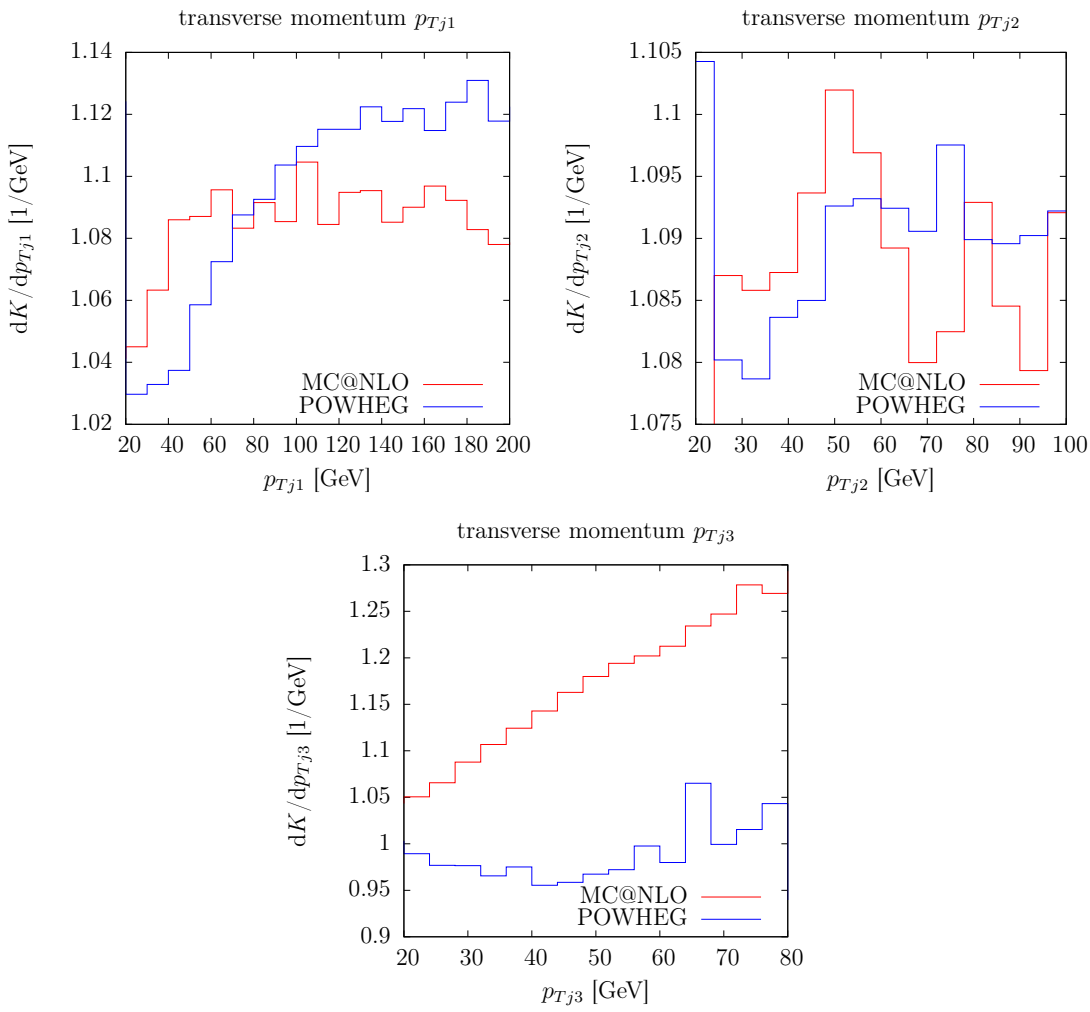

Figure 7.10: Differential K-factor distibution in dependence the transverse momenta of the three hardest jets.

in this context, a differential K-factor over an observable $\mathcal{O}$ can be defined as

$$\frac{\mathrm{d}K}{\mathrm{d}\mathcal{O}} = \frac{\mathrm{d}\left(\sigma^{matched}/\sigma^{LO+PS}\right)}{\mathrm{d}\mathcal{O}}. \tag{7.3}$$

The differential K-factors in dependence of the transverse momenta of the three tagging jets are shown in Figure 7.10. Although the fluctuations are rather large at the statistics that could be acquired, general tendencies can be recognised.

For the two tagging jets, which are already present in the plain LO calculation, the K-factors show a dependence of the matching scheme. For transverse momenta of about $p_{Tj1} \lessapprox 80\,\mathrm{GeV}$ and $p_{Tj2} \lessapprox 60\,\mathrm{GeV}$, the corrections picked up by the MC@NLO matching scheme are larger than those within the POWHEG approach. As we have seen that the formation of a third jet is suppressed within POWHEG, this behaviour is an indication that the POWHEG emissions are picked up by the jet algorithm and assigned to the tagging jets.

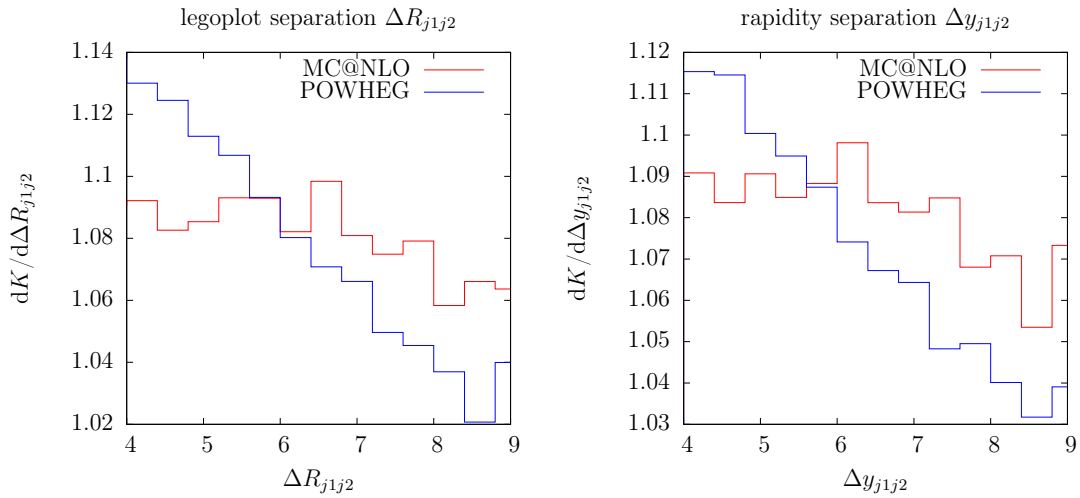

Figure 7.11: Differential K-factor distribution in dependence of the legoplot and rapidty separations.

The K-factor of the p_T of the hardest tagging jet within the MC@NLO matching scheme is increasing steeply on the lower end of the spectrum and reaches approximately 109% at 40 GeV. For increasing transverse momentum, the K-factor stays almost constant. Within the POWHEG matching scheme, the situation is different. Here, the K-factor rises slower than within MC@NLO and reaches its maximum of 112% at $p_{Tj1} = 130\,\mathrm{GeV}$.

The third hardest jet is not present in the LO matrix element. Therefore, predictions concerning it are only accurate up to leading order in the strong coupling constant. As its distribution is unaffected by NLO subtraction terms, its differential K-factor is smoother with the given statistics.

As already shown previously, the third jets emerging within the MC@NLO matching scheme are much harder than the ones emitted within POWHEG. In Figure 7.10, this is visible again. Within the MC@NLO scheme, the differential K-factor for p_{Tj3} shows a constant growth from 105% to over 125% in the plotted range of transverse momenta ranging from 20 GeV to 80 GeV. The POWHEG equivalent on the other hand shows a completely different behaviour. Here, the differential K-factor is decreasing before reaching its minimum of about 96% at $p_{Tj3} \approx 40\,\mathrm{GeV}$. Then, it rises slightly but stays below 100% for transverse momenta of below 65 GeV.

The differential K-factors in dependence of legoplot and rapidity separations of the tagging jets are shown in Figure 7.11. The higher order corrections in both observables are positive all over the plotted range and decrease in size for higher separations in both matching schemes.

Within the POWHEG matching scheme, the differential K-factors of both legoplot and rapidity separations show a steeper slope in the tail regions than within the MC@NLO matched calculation. The shapes of the distributions show that POWHEG emissions tend to be more central and in the direction between the

tagging jets. The same behaviour could be seen in Figure 7.7, where the y^* distribution was plotted and the three-jet cross section was vastly enhanced in the central region.

The corrections that are gained within the NLO matched calculations are sizeable and exceed 10% in some regions of phase space. They depend on the matching scheme which adds a new source of systematical uncertainty that is introduced beyond the fixed order calculation.

7.3 Scale variations

Scale choices introduce unphysical scale dependencies in the simulated observables. In the current section, scale uncertainties that are already present within the LO and NLO calculations will be investigated, as they also have an impact on the matched calculation. These are the uncertainties that are introduced by the choice of the renormalisation and factorisation scales μ_R and μ_F. In order to estimate the scale uncertainties in the LO showered calculation and their remainders in the matched calculation, the choices of the scale factors defined in (5.9) were varied independently in the range of $0.5 < \xi < 2.0$.

Factorisation and renormalisation scales influence both the hard matrix element and the shower evolution. The evolution of the strong coupling constant depends on the chosen renormalisation scale, therefore the whole shower is affected by a change in μ_R. The choice of a factorisation scale, on the other hand, does only affect splittings with an initial state emitter or spectator, as the splitting probabilities comprise PDF ratios in these cases [62].

Figures 7.12 - 7.16 depict the scale uncertainties in different jet observables. Each figure consists of three different plots. In the upper panel, μ_F and mu_R are varied simultaneously. In the middle panel, only μ_F is varied and in the lower panel, only μ_R is varied. The MC@NLO matched results are given by coloured histograms. In each plot, there are also two black histograms which show the LO showered results with the same setups as in the MC@NLO matched results in the same panel.

In the top panels where the scale factors are varied both, it is visible that the scale dependence is smaller within the matched calculation than within the LO showered one. The same holds for the second panel, where only the factorisation scale factor is varied.

When varying the renormalisation scale factors only, a different behaviour shows up when the considered observable is already present in the LO matrix element. As this has no dependence on α_S in the case of Hjj production via VBF, the only renormalisation scale dependence in a LO showered calculation is introduced by the parton shower. It was shown that the enhancements of the tagging jets that can be expected by the shower are small, therefore also the introduced uncertainty is a small effect. In the matched calculation however, already the matrix elements contain a factor of α_S. This contributes to the total renormalisation scale uncertainty, which has about the same magnitude for the LO and matched calculations.

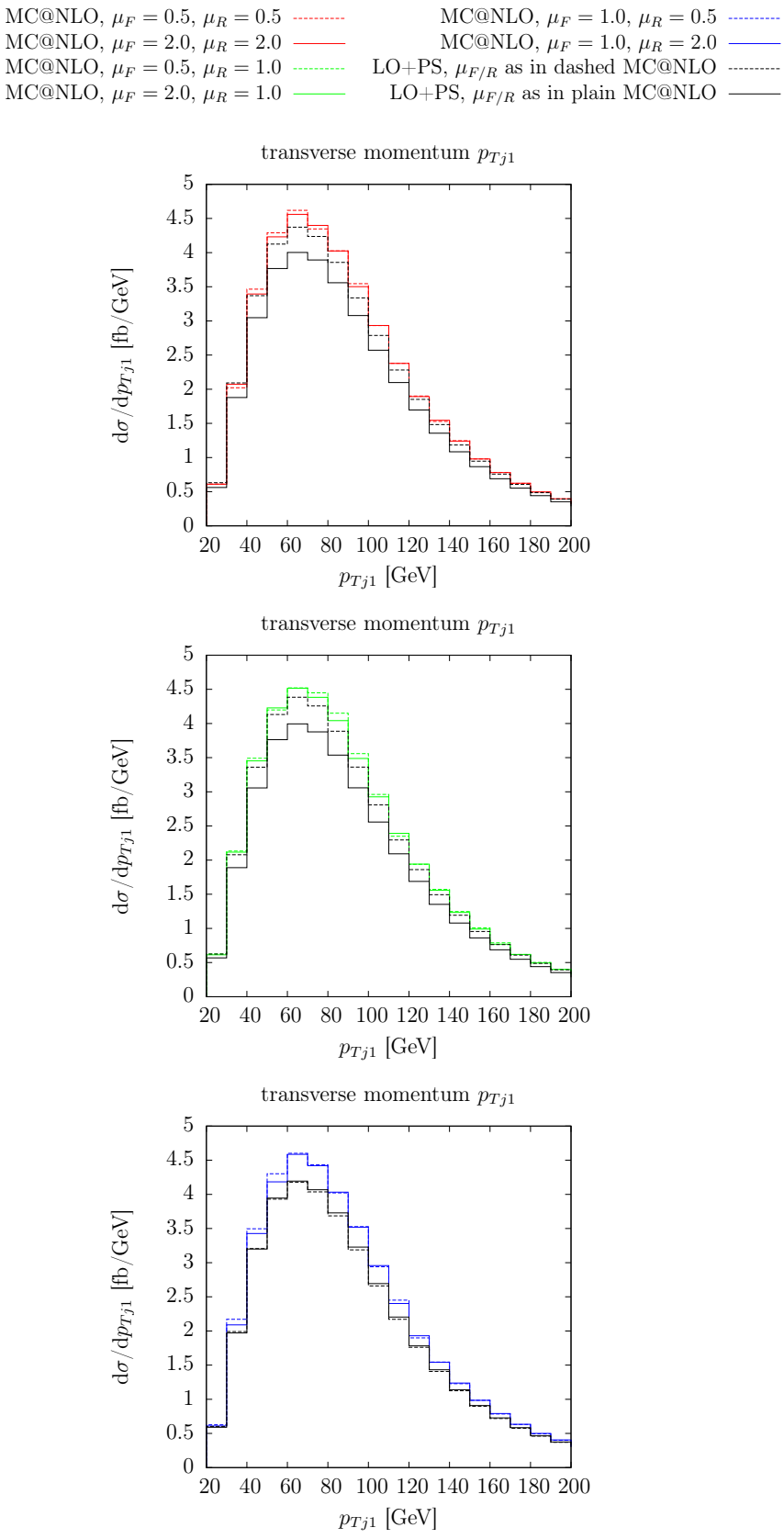

Figure 7.12: Scale dependencies of the transverse momentum distribution of the hardest tagging jet.

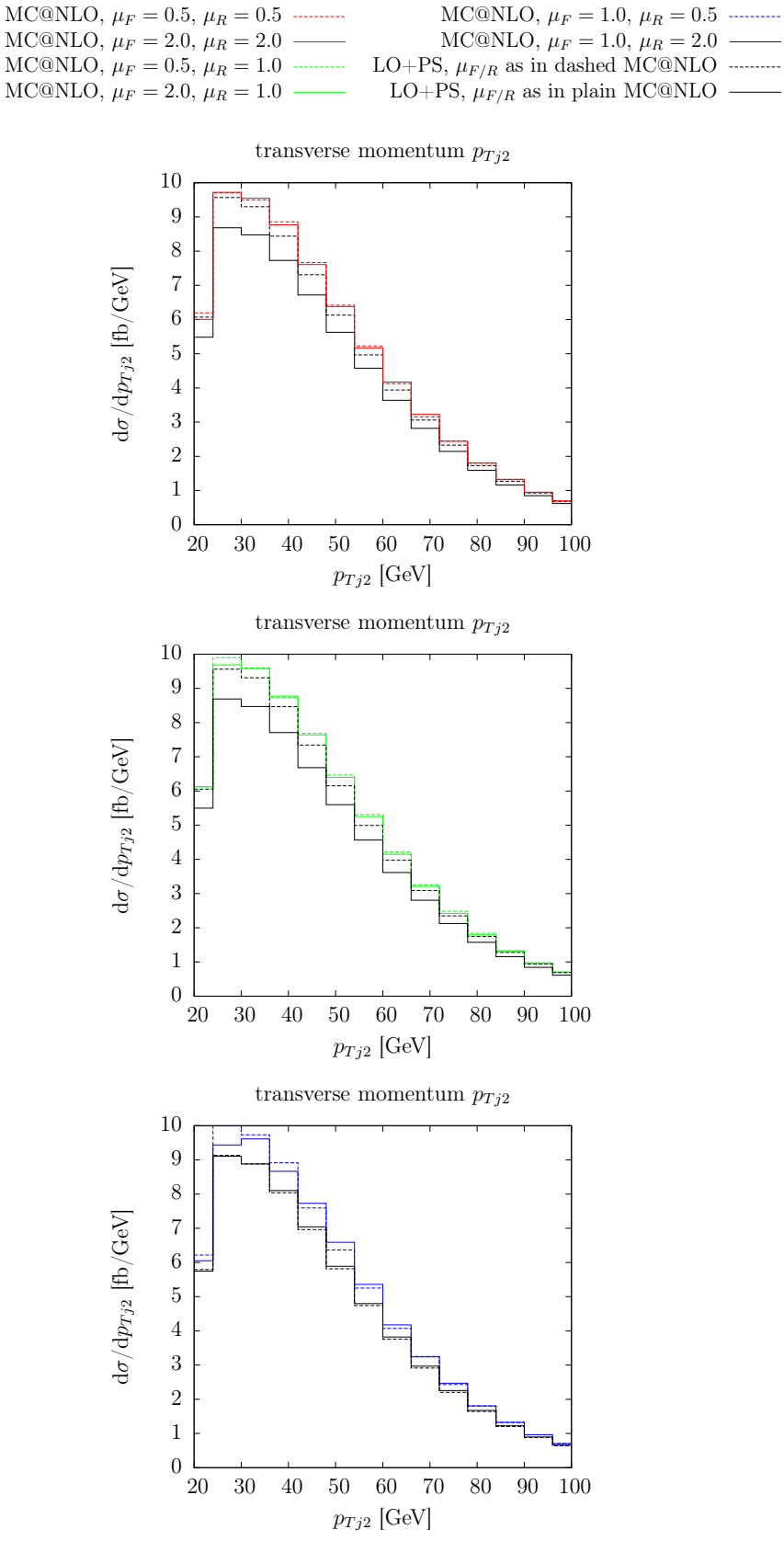

Figure 7.13: Scale dependencies of the transverse momentum distribution of the second hardest tagging jet.

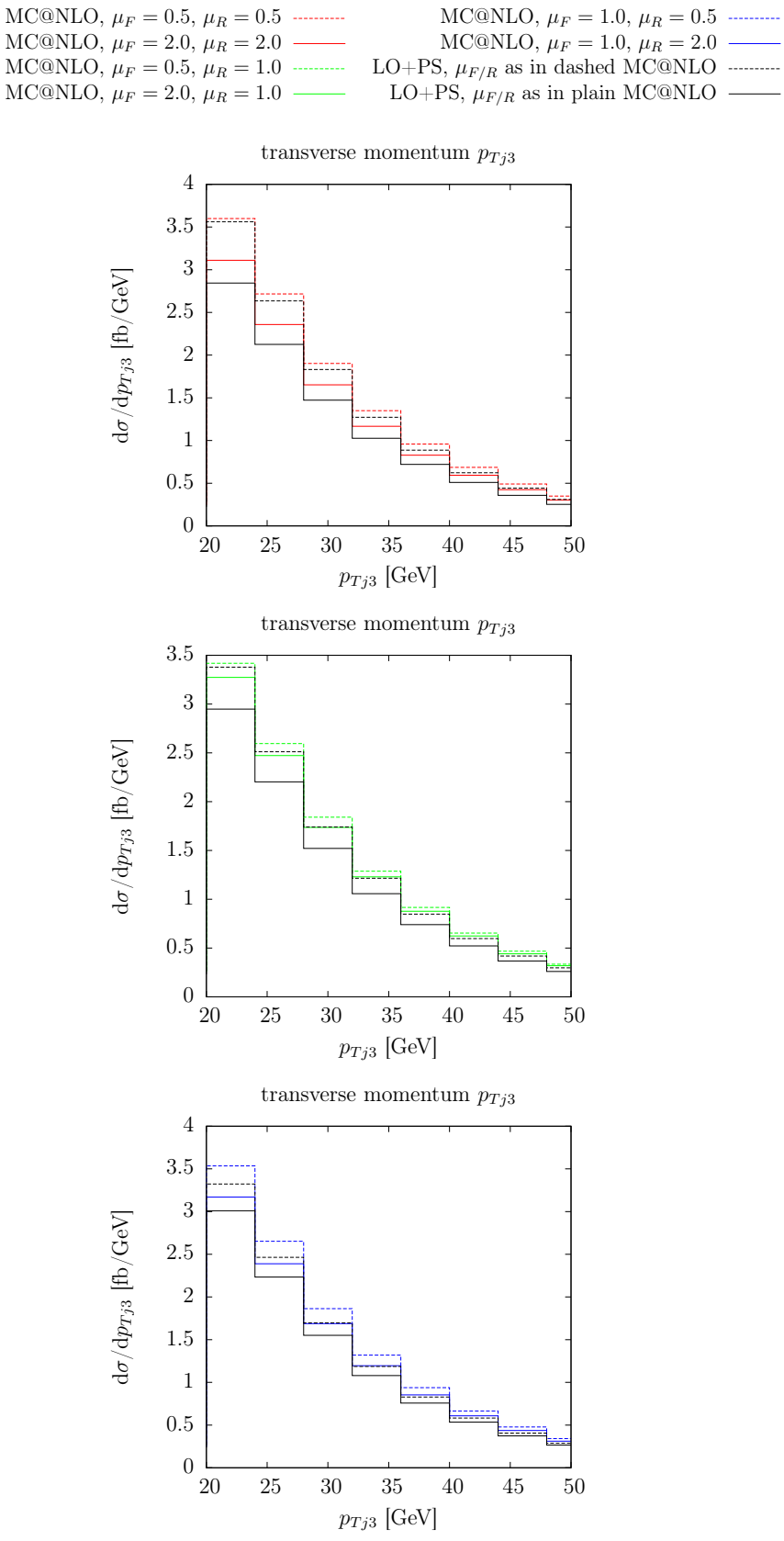

Figure 7.14: Scale dependencies of the transverse momentum distribution of the third hardest jet.

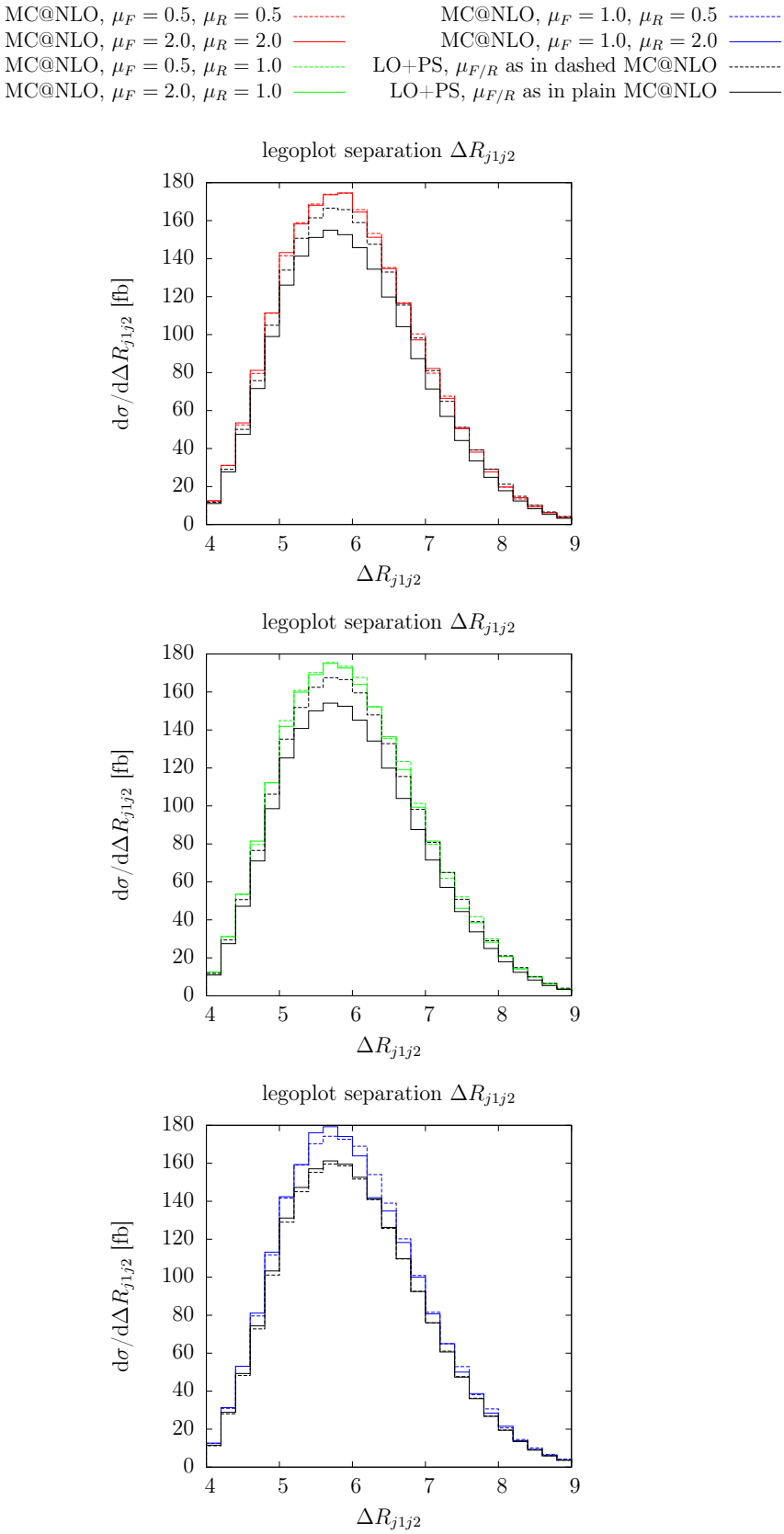

Figure 7.15: Scale dependencies of the legoplot separation distribution of the tagging jets.

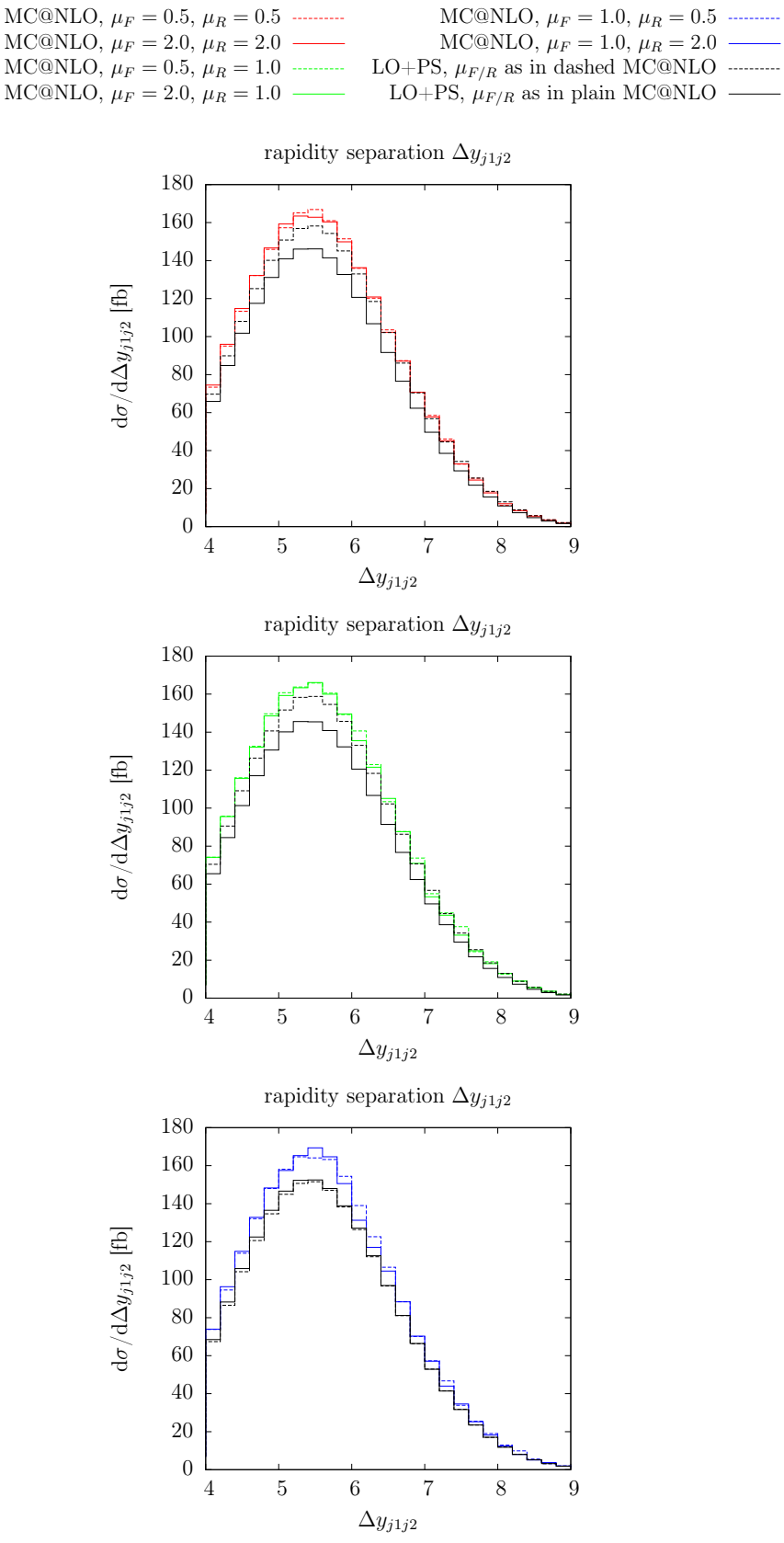

Figure 7.16: Scale dependencies of the rapidity separation distribution of the tagging jets.

7.4 Summary

The POWHEG and MC@NLO matching schemes were compared in the case of Hjj production via vector boson fusion. The two schemes lead a reduced cross section relative to the NLO result. For the tagging jets, the matched results show the same behaviour. The shapes of the distributions are only mildly affected when compared to the NLO predictions.

The three-jet cross sections for the two matching schemes differ. Within POWHEG, the three-jet cross section matches the one predicted by the NLO calculation. The emissions, however, are softer and more central. MC@NLO, on the other hand, has a larger probability to emit third jets than the fixed order calculation. Third jets within MC@NLO tend to be more directed into the forward and backward regions.

It was shown that the differential K-factors within the matched calculation are not only dependent on the considered observable and region of phase space, but also very much on the matching scheme that was used. POWHEG and MC@NLO behave very differently and the corrections that are picked up within the matched calculation exceed 10% for some observables and regions of phase space.

The dependence on the factorisation scale in the matched calculation is smaller than in the LO showered one. The behaviour upon variation of the renormalisation scale factor depends on if the examined observable is already present at LO.

Summary

The Large Hadron Collider is in operation for several years now, covering a wide range of experimental interests. The conclusions that might be drawn from the acquired data do not solely depend on the (already outstanding) quality of the detectors at the experiments. Precise and robust theoretical predictions for signal and background processes are also needed to cope with the highly challenging environment in hadron collisions. This goal can be achieved by higher order corrections, event simulations or a mixture of both within NLO-matched calculations.

The first part of this thesis consisted of an introduction into the field theoretical basics and the techniques that are used within calculations in high-energy physics. The Standard Model and its constituent theories were described. The problems that arise within plain and showered NLO calculations were clarified. A knowledge on their solutions by NLO subtraction and NLO matching was procured.

The second part of the thesis at hand delivered NLO QCD corrections to $H\gamma jj$ production at the LHC. The additional photon is required to improve background suppression within events with $H \to b\bar{b}$ decays. The process was implemented in form of a fully flexible Monte-Carlo program. The code developed within this thesis, which was released as part of the package VBFNLO, was carefully checked against automatically generated code and independent implementations of the same process.

Total cross sections for different PDFs and scale choices were presented. The residual impact of the choice of PDF and scale are small and of the order of 2%. It was shown that the differential K-factors and scale uncertainties are dependent on the observable and region of phase space. When going from LO to NLO, the differential and total scale uncertainties are reduced drastically.

With the third part, the door to showered calculations was opened. Aiming at a NLO-matched calculation of Hjj production, an interface between Matchbox, an addon to Herwig++, and VBFNLO was established as part of this work. This was achieved in a machine independent mixed language approach supported by the `cfortran.h` header file. All VBFNLO subroutines and common blocks that had to be accessed from Matchbox had to be prototyped in C++.

Before discussing the results of NLO-matched Hjj production, a description of some of the internal structure of Herwig++ was given. The relevant chapter focused on the generation of phase space and the two shower implementations that are available within Herwig++, namely the default and the dipole shower.

The analysis setup that was used in the result sections of Hjj production was described. It was shown that the interfaced calculation and the original implementation in VBFNLO give the same results at fixed order. It was validated that the automated dipole subtraction which is carried out within Matchbox gives finite results as the subtraction terms match the real emission contributions in the singular regions.

Results were presented for a showered calculation of Hjj production at leading order. The two tagging jets were only mildly affected by shower emissions. The most prominent feature here was a loss of transverse momentum of the hardest jet when the default shower was applied. The dipole shower, on the other hand, resulted in the same p_T distribution as the leading order matrix element.

The third hardest jets, being produced only by shower emissions, show a large dependence on the parton shower implementation in all observables that were investigated. In general, the dipole shower has a larger phase space available for emissions, which gives rise to major differences in higher order observables.

Results for NLO-matched Hjj production were also shown, both for MC@NLO and POWHEG matching schemes. The matching schemes could easily be switched within the unified framework provided by Matchbox. The presented results were obtained with the dipole shower. Observables concerning the tagging jets show only negligible modifications of shapes. Concerning predictions of observables influenced by third jets, the two matching schemes have shown to differ both in shape and normalisation.

The present work is an attempt to improve predictions for hadron collisions and understand their systematical uncertainties. It is a contribution to the striving for knowledge about the most fundamental properties of nature. To this end, tools for NLO corrections and parton showers were written and made publicly available, which are expected to be relevant for analyses of data acquired at the LHC.

Appendix A

Structure of the implementation of $H\gamma jj$ in VBFNLO

As the implementation of $H\gamma jj$ in VBFNLO deviates from the style of most other processes, the following shall serve as a documentation. The basic idea of the implementation is to calculate bi-spinor currents `JIOXXX` in the HELAS framework once per phase space point. As they are needed for several processes, they are stored in common blocks. The definitions for the HELAS currents and spinors can be found in [77]. Before the matrix elements are calculated in the subroutines `HAjj(j)_ME` (`HAjj_subtr_ME` for the subtraction terms), the bi-spinor currents are evaluated once for all crossing-related subprocesses within the subroutines `Get_HAjj(j)_currents` (`Get_HAjj_subtr_currents` for the subtraction terms).

In the subroutine `Get_HAjj_couplings`, the common block

```
COMMON /HAJJCOUPL/ GBF
```

is filled. In `GBF`, all couplings for the $H\gamma jj$ process are stored.

`Get_HAjj_currents` fills the following common blocks.

```
 COMMON /HAJJCURRENTS/ Curr12,Curr21,Curr34,Curr43,
$     Curr1A2,Curr2A1,Curr3A4,Curr4A3,
$     Curr12tbv,Curr21tbv,Curr34tbv,Curr43tbv,
$     Higgs,fac

 COMMON /HAJJCURRENTSVIRT/ SpinorI,SpinorO,Photon,
$     Curr12H,Curr21H,Curr34H,Curr43H,
$     pIntBosU,pIntBosL,scale,
$     alsUpperc2o4pi,alsLowerc2o4pi,alsULcvirtc2o4pi
```

The variables needed for the LO calculation are defined as follows:

- `CurrXY(6,3:4,-1:1,2:3)`: Bi-spinor current with attached weak boson propagator, as sketched in Figure A.1. Arguments: Current (four-momentum and spinor components), incoming flavour type (up- or down-type), helicity (positive or negative), attached weak boson type (Z or W).

- `CurrXAY(6,3:4,-1:1,2,-1:1,2:3)`: Bi-spinor current with attached photon and weak boson propagator, as sketched in Figure A.2. Arguments: Current, incoming flavour type, fermion helicity, photon insertion leg (1 to 2 for upper line, 3 to 4 for lower line), photon helicity, attached weak boson type.
- `CurrXYtbv(6,3:4,-1:1,-1:1)`: Bi-spinor current with attached triple gauge boson vertex, as sketched in Figure A.3. Arguments: Current, incoming flavour type, fermion helicity, photon helicity.
- `Higgs(6)`: Higgs spinor.
- `fac`: Phase space and colour factor.

For the virtual corrections, another common block is defined containing:

- `SpinorI/O(6,4,-1:1)`: Incoming/outgoing spinor. Arguments: Spinor, particle number, particle helicity.
- `Photon(6,-1:1)`: Photon spinor. Arguments: Spinor, photon helicity.
- `CurrXYH(6,3:4,-1:1,2:3)`: Bi-spinor current with attached Higgs boson and weak boson propagator, as sketched in Figure A.4. Arguments: Current, incoming flavour type, fermion helicity, attached weak boson type.
- `pIntBosU/L(0:4)`: Momentum and invariant mass of the weak boson propagator attached to the upper/lower fermion line.
- `scale`: Scale of the process.
- `alsUpperc2o4pi`, `alsLowerc2o4pi`: $\alpha_s \frac{C_2}{4\pi}$ with α_s of the upper or lower line and $C_2 = 4/3$.
- `alsULcvirtc2o4pi`: $\left(\alpha_s^{\text{Upper}} + \alpha_s^{\text{Lower}}\right) \frac{C_2}{4\pi} c_{\text{virt}}$ with c_{virt} as a finite remainder of the CS subtraction.

As there are two different $\tilde{p}$-kinematics involved in the subtraction, the currents which are needed for the dipole subtraction matrix elements have an additional index. They are stored in a separate common block, which is filled by the subroutine `Get_HAjj_subtr_currents`.

```
      COMMON /HAJJSUBTRCURRENTS/ Curr12,Curr21,Curr34,Curr43,
     $     Curr1A2,Curr2A1,Curr3A4,Curr4A3,
     $     Curr12tbv,Curr21tbv,Curr34tbv,Curr43tbv,
     $     Higgs,fac
```

To the list of arguments, a new entry is inserted in the second place defining the kinematics. That results in the following changes:

- `CurrXY(6,2:3,3:4,-1:1,2:3)`: Arguments: Current, $\tilde{p}$-kinematics, incoming flavour type, helicity, attached weak boson type.

- `CurrXAY(6,2:3,3:4,-1:1,2,-1:1,2:3)`: Arguments: Current, $\tilde{p}$-kinematics, incoming flavour type, fermion helicity, photon insertion leg (1 to 2 for upper line, 3 to 4 for lower line), photon helicity, attached weak boson type.

- `CurrXYtbv(6,2:3,3:4,-1:1,-1:1)`: Arguments: Current, $\tilde{p}$-kinematics, incoming flavour type, fermion helicity, photon helicity.

For the real-emission part, a larger common block is needed as more currents need to be stored. Its variables are calculated in `Get_HAjjj_currents`.

```
 COMMON /HAJJJCURRENTS/ fac,Higgs,Curr12,Curr21,Curr34,Curr43,
$     Curr12A,Curr21A,Curr34A,Curr43A,
$     Curr12GO,Curr21GO,Curr34GO,Curr43GO,Curr21GI,Curr43GI,
$     Curr12GOt1Z,Curr21GOt1Z,Curr34GOt1Z,Curr43GOt1Z,
$     Curr21GIt1Z,Curr43GIt1Z,Curr12GOt2Z,Curr21GOt2Z,
$     Curr34GOt2Z,Curr43GOt2Z,Curr21GIt2Z,Curr43GIt2Z,
$     Curr12GOt1W,Curr21GOt1W,Curr34GOt1W,Curr43GOt1W,
$     Curr21GIt1W,Curr43GIt1W,Curr12GOt2W,Curr21GOt2W,
$     Curr34GOt2W,Curr43GOt2W,Curr21GIt2W,Curr43GIt2W,
$     Curr12tbv,Curr21tbv,Curr34tbv,Curr43tbv,
$     Curr12GOtbv,Curr21GOtbv,Curr34GOtbv,Curr43GOtbv,
$     Curr21GItbv,Curr43GItbv
```

The arrays are indexed as defined below.

- `CurrXY(6,3:4,-1:1,2:3)`: Bi-spinor current with attached weak boson propagator, as sketched in Figure A.1. Arguments: Current, fermion type, fermion helicity, weak boson type.

- `CurrXYA(6,3:4,-1:1,2,-1:1,2:3)`: Bi-spinor current with attached weak boson propagator and photon, as sketched in Figure A.2. Arguments: Current, flavour type, fermion helicity, photon insertion leg (1 to 2 for upper line, 3 to 4 for lower line), photon helicity, weak boson type.

- `CurrXYGO(6,3:4,-1:1,4,-1:1,2:3)`: Bi-spinor current with attached weak boson propagator and outgoing gluon, as sketched in Figure A.5. Arguments: Current, flavour type, fermion helicity, gluon insertion leg (1 to 2 for upper line, 3 to 4 for lower line), gluon helicity, weak boson type.

- `CurrXYGI(6,3:4,-1:1,4,-1:1,2:3)`: Bi-spinor current with attached weak boson propagator and incoming gluon, as sketched in Figure A.6. Arguments: Current, flavour type, fermion helicity, gluon insertion leg, gluon helicity, weak boson type.

- `CurrXYGIt1W/Z(6,3:4,-1:1,-1:1,-1:1,2,2)`: Bi-spinor current with attached W/Z-boson propagator and photon plus an incoming gluon, as

sketched in Figure A.7. Along the fermion line, one massless boson is emitted on each side of the weak boson propagator. Arguments: Current, flavour type, fermion heliciy, photon helicity, gluon helicity, photon insertion leg referring to the uncrossed diagram, gluon insertion leg referring to the uncrossed diagram (for the last two arguments: 1 to 2 for upper line, 3 to 4 for lower line).

- `CurrXYGIt2W/Z(6,3:4,-1:1,-1:1,-1:1,2,2)`: Bi-spinor current with attached W/Z-boson propagator and photon plus an incoming gluon, as sketched in Figure A.8. Along the fermion line, both massless bosons are emitted on the same side of the weak boson propagator. Arguments: Current, flavour type, fermion helicity, photon helicity, gluon helicity, insertion leg referring to the uncrossed diagram (1 to 2 for upper line, 3 to 4 for lower line), insertion order (1 for photon emission prior to gluon emission, 2 else).

- `CurrXYGOt1W/Z(6,3:4,-1:1,-1:1,-1:1,2,2)`: Bi-spinor current with attached W/Z-boson propagator and photon plus an outgoing gluon, as sketched in Figure A.9. Along the fermion line, one massless boson is emitted on each side of the weak boson propagator. Arguments: Current, flavour type, fermion helicity, photon helicity, gluon helicity, photon insertion leg (1 to 2 for upper line, 3 to 4 for lower line), gluon insertion leg.

- `CurrXYGOt2W/Z(6,3:4,-1:1,-1:1,-1:1,2,2)`: Bi-spinor current with attached W/Z-boson propagator and photon plus an outgoing gluon, as sketched in Figure A.10. Along the fermion line, both massless bosons are emitted on the same side of the weak boson propagator. Arguments: Current, flavour type, fermion helicity, photon helicity, gluon helicity, insertion leg (1 to 2 for upper line, 3 to 4 for lower line), insertion order (1 for photon emission prior to gluon emission, 2 else).

- `CurrXYtbv(6,3:4,-1:1,-1:1)`: Bi-spinor current with attached triple gauge boson vertex, as sketched in Figure A.3. Arguments: Current, flavour type, fermion helicity, photon helicity

- `CurrXYGOtbv(6,3:4,-1:1,-1:1,2,-1:1)`: Bi-spinor current with attached triple gauge boson vertex and outgoing gluon, as sketched in Figure A.11. Arguments: Current, flavour type, fermion helicity, photon helicity, gluon insertion leg (1 to 2 for upper line, 3 to 4 for lower line), gluon helicity.

- `CurrXYGItbv(6,3:4,-1:1,-1:1,2,-1:1)`: Bi-spinor current with attached triple gauge boson vertex and incoming gluon, as sketched in Figure A.12. Arguments: Current, flavour type, fermion helicity, photon helicity, gluon insertion leg (1 to 2 for upper line, 3 to 4 for lower line), gluon helicity.

- `Higgs(6)`: Higgs spinor.

- `fac`: Phase space and colour factor.

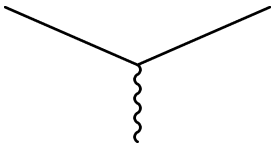

Figure A.1: `CurrXY`

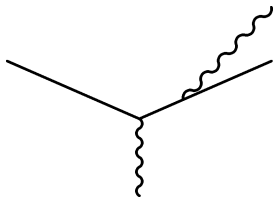

Figure A.2: `CurrXYA`

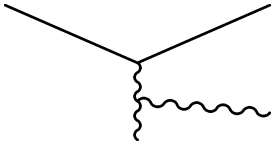

Figure A.3: `CurrXYtbv`

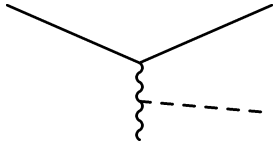

Figure A.4: `CurrXYH`

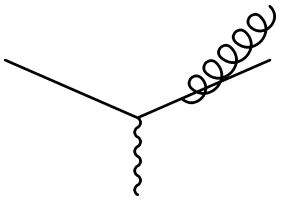

Figure A.5: `CurrXYGO`

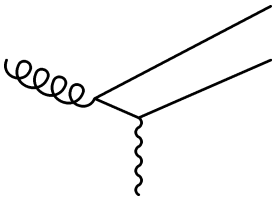

Figure A.6: `CurrXYGI`

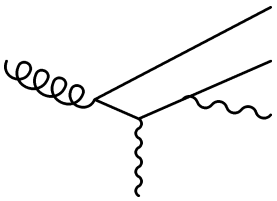

Figure A.7: `CurrXYGIt1W/Z`

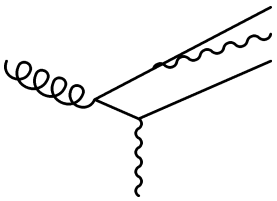

Figure A.8: `CurrXYGIt2W/Z`

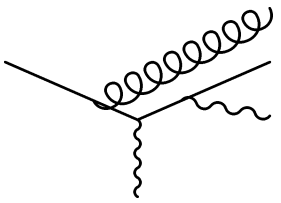

Figure A.9: `CurrXYGOt1W/Z`

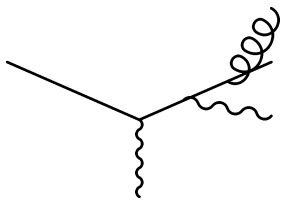

Figure A.10: `CurrXYGOt2W/Z`

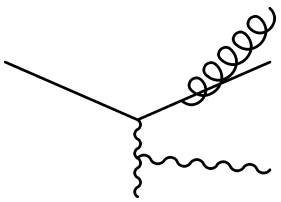

Figure A.11: `CurrXYGOtbv`

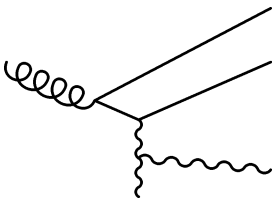

Figure A.12: `CurrXYGItbv`

Appendix B

Interface between Herwig++ and VBFNLO

For the NLO matched Hjj production via VBF, an interface was established between VBFNLO and Herwig++. As VBFNLO is coded in FORTRAN77, some difficulties arise. The definitions of arrays are handled differently in FORTRAN77 and C++. While in FORTRAN77, array indices start by default with 1 but can be defined differently, the definition in C++ is that 0 always indexes the first element of an array. Further complications arise by the fact that for multidimensional arrays, the order of indices is inverted when accessed from the other language. As there is no check at compile time whether the definitions match, these and other differences make the interface very prone to errors. The purpose of this chapter is to give a complete overview of the definitions that were made inside Herwig++, which might be helpful for future adaptions of the code, as the work on both programs is ongoing.

The interface to VBFNLO was established using the framework provided by `cfortran.h` [91]. All functions and common blocks that needed to be interfaced are prototyped in one single file `VBFNLOPrototypes.h`. The definition of the common blocks takes place in `VBFNLOCommonBlocks.h`, which needs to be included in every class accessing VBFNLO.

The implemented classes show a twofold structure. The `Amplitude` objects contain every information needed for the evaluation of the squared matrix element. In the `ME` objects, only the initialisation of diagrams and colour lines takes place. The following classes were implemented in Herwig++:

- `VBFNLOAmplitudeBase`, `VBFNLOMEBase`: Initialise process independent SM parameters in VBFNLO, such as quark masses and electroweak parameters. Call `SETEWPARA`, `CTRANS` and `KOPPLN`.

- `VBFNLOAmplitudeVVJJNeutralBase`, `VBFNLOMEVVJJNeutralBase`: Intended as abstract base classes all for VBF processes with an electromagnetic neutral-boson final state, such as Zjj or W^+W^-jj. Convert momenta from Herwig++ convention to VBFNLO convention. Filter only the relevant

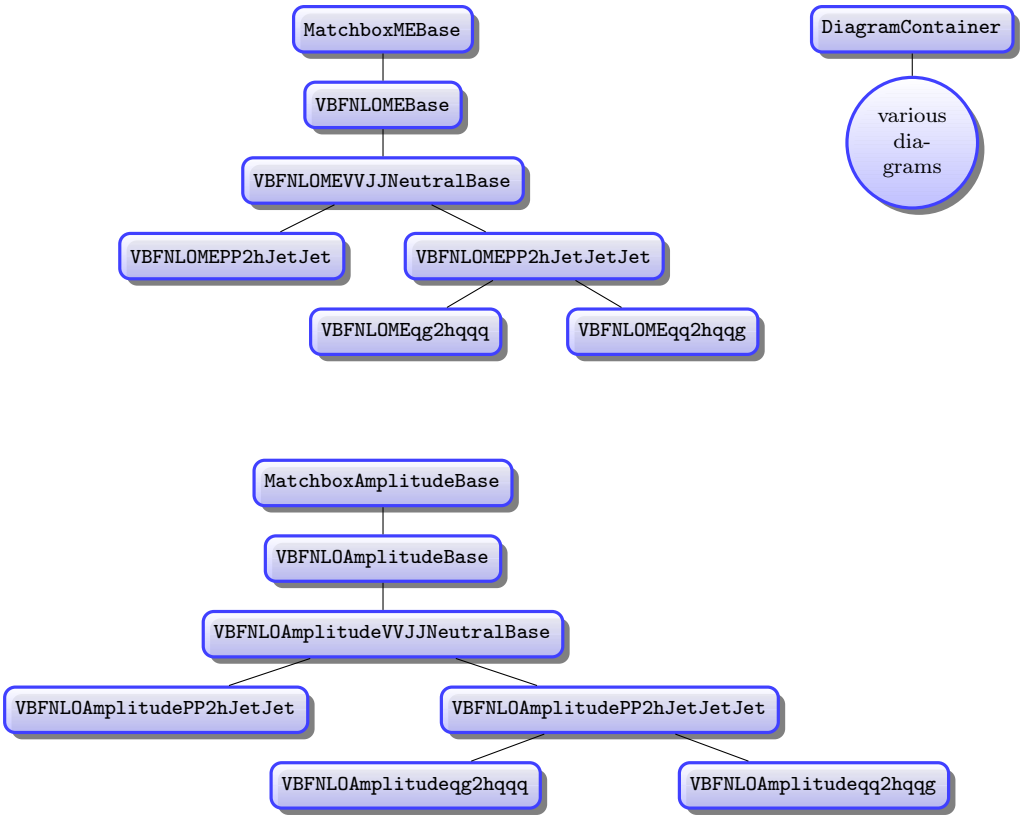

Figure B.1: Inheritance diagram for the classes that were implemented in Herwig++.

subprocess required by Herwig++ from the different flavour dependent subprocesses which are calculated by VBFNLO for each phase space point.

- `VBFNLOAmplitudePP2hJetJet`, `VBFNLOMEPP2hJetJet`: Concrete implementation of all the $qq \to hqq$-type matrix elements squared. Set up diagrams and other process dependent information. Call the VBFNLO coupling initialisation `QQHQQGI` and matrix-element implementation `QQHQQ`. Are capable of calculating the virtual interference terms by calling the Born matrix elements with an additional flag requesting the interference.

- `VBFNLOAmplitudePP2hJetJetJet`, `VBFNLOMEPP2hJetJetJet`: Abstract base classes for the two real-emission configurations. Call the VBFNLO coupling initialisation `QQHQQGI` and matrix element implementation `QQHQQJ`.

- `VBFNLOAmplitudeqq2hqqg`, `VBFNLOMEqq2hqqg`: Concrete implementation of all the $qq \to hqqg$-type matrix elements squared. Initialise process-dependent information such as diagrams and colour flows.

- `VBFNLOAmplitudeqq2hqqg`, `VBFNLOMEqq2hqqg`: Same for the $qg \to hqqg$-type matrix elements.

- `DiagramContainer`: Abstract base class for process dependent diagram and colour flow information which was generated automatically with the help of output from QGRAF [105].
- Various classes derived from `DiagramContainer`: Automatically generated diagrams, one class for each process, t-channel charge flow and initial-state particle/antiparticle configuration.

For documentational purposes, the subroutines that were interfaced are listed below in form of their definition within Herwig++.

```
PROTOCCALLSFSUB0(INITCOUPLINGS,initcouplings)
#define INITCOUPLINGS() CCALLSFSUB0(INITCOUPLINGS,initcouplings)

PROTOCCALLSFSUB9(KOPPLN,koppln,INT,DOUBLE,DOUBLE,DOUBLE,DOUBLE,
  DOUBLE,DOUBLE,DOUBLE,DOUBLE)
#define KOPPLN(INFO,e,g2,s,c,z,w,q,g) CCALLSFSUB9(KOPPLN,koppln,
  INT,DOUBLE,DOUBLE,DOUBLE,DOUBLE,DOUBLE,DOUBLE,DOUBLE,DOUBLE,
  INFO,e,g2,s,c,z,w,q,g)

PROTOCCALLSFSUB8(SETEWPARA,setewpara,PDOUBLE,PDOUBLE,PDOUBLE,
  PDOUBLE,PDOUBLE,PDOUBLE,PDOUBLE,PDOUBLE)
#define SETEWPARA(e,g2,s,c,z,w,q,g) CCALLSFSUB8(SETEWPARA,setewpara,
  PDOUBLE,PDOUBLE,PDOUBLE,PDOUBLE,PDOUBLE,PDOUBLE,PDOUBLE,PDOUBLE,
  e,g2,s,c,z,w,q,g)

PROTOCCALLSFSUB1(CTRANS,ctrans,DOUBLE)
#define CTRANS(xmb) CCALLSFSUB1(CTRANS,ctrans,DOUBLE,xmb)

PROTOCCALLSFSUB0(CLEARWIDTHS,clearwidths)
#define CLEARWIDTHS() CCALLSFSUB0(CLEARWIDTHS,clearwidths)

PROTOCCALLSFSUB1(DEF_PS_VNJ,def_ps_vnj,INT)
#define DEF_PS_VNJ(bos) CCALLSFSUB1(DEF_PS_VNJ,def_ps_vnj,INT,bos)

PROTOCCALLSFSUB10(QQHQQ,qqhqq,DOUBLEVV,INTV,INT,PDOUBLE,PDOUBLE,
  PDOUBLE,PDOUBLE,PDOUBLE,PDOUBLE,DOUBLEV)
#define QQHQQ(pbar,sign,nlo,uucc,uuss,ddcc,ddss,udsc,ducs,tree)
  CCALLSFSUB10(QQHQQ,qqhqq,DOUBLEVV,INTV,INT,PDOUBLE,PDOUBLE,
  PDOUBLE,PDOUBLE,PDOUBLE,PDOUBLE,DOUBLEV,pbar,sign,nlo,uucc,
  uuss,ddcc,ddss,udsc,ducs,tree)

PROTOCCALLSFSUB10(QQHQQJ,qqhqqj,DOUBLEVV,INTV,DOUBLEV,INT,PDOUBLE,
  PDOUBLE,PDOUBLE,PDOUBLE,PDOUBLE,PDOUBLE)
#define QQHQQJ(pbar,fsign,qbar,gsign,uucc,uuss,ddcc,ddss,udsc,ducs)
```

```
  CCALLSFSUB10(QQHQQJ,qqhqqj,DOUBLEVV,INTV,DOUBLEV,INT,PDOUBLE,
  PDOUBLE,PDOUBLE,PDOUBLE,PDOUBLE,PDOUBLE,pbar,fsign,qbar,gsign,
  uucc,uuss,ddcc,ddss,udsc,ducs)

PROTOCCALLSFSUB1(QQHQQGI,qqhqqgi,INT)
#define QQHQQGI(bosdec) CCALLSFSUB1(QQHQQGI,qqhqqgi,INT,bosdec)
```

The Herwig++ definitions of VBFNLO's common blocks that need to be accessed are listed in the following:

```
struct BLIPSIVNJ_DEF{
  mutable double RM2,RMG,RM2MIN,RM2MAX,S,M2MIN;
  mutable double YJMIN[4],YJMAX[4],PTJMIN[4],EJMIN[4];
  mutable int INFOJ[4];
};
#define BLIPSIVNJ COMMON_BLOCK(BLIPSIVNJ,blipsivnj)
COMMON_BLOCK_DEF(BLIPSIVNJ_DEF,BLIPSIVNJ);

struct BKOPOU_DEF{
  mutable double CLR[3][5][4],XM2[6],XMG[6],B[6][6][6],V[5][4],A[5][4];
};
#define BKOPOU COMMON_BLOCK(BKOPOU,bkopou)
COMMON_BLOCK_DEF(BKOPOU_DEF,BKOPOU);


struct BKOPIN_DEF{
  mutable double ALFAS,XMT,ALFA,XMZ,XMW,SIN2W,XMH,GF,ALFAS_LO;
};
#define BKOPIN COMMON_BLOCK(BKOPIN,bkopin)
COMMON_BLOCK_DEF(BKOPIN_DEF,BKOPIN);

struct QUARKMASSES_DEF{
  mutable double XMB,BMASS_H,XMC,CMASS_H,XMTAU;
};
#define QUARKMASSES COMMON_BLOCK(QUARKMASSES,quarkmasses)
COMMON_BLOCK_DEF(QUARKMASSES_DEF,QUARKMASSES);

struct CGLOBALD_DEF{
  mutable double ECM;
};
#define CGLOBALD COMMON_BLOCK(CGLOBALD,cglobald)
COMMON_BLOCK_DEF(CGLOBALD_DEF,CGLOBALD);

struct CGLOBALL_DEF{
  mutable bool FEYNH_SWITCH,SLHA_SWITCH,EWCOR_SWITCH;
```

```
  mutable bool LOOPSQR_SWITCH,LOOPSQR_SWITCHIN;
  mutable bool HASNLO,HASFLOOPS;
  mutable bool DOBORN,DOVIRTUALS,DOEMISSIONS,DOFLOOPS;
  mutable bool INFLOOPS;
};
#define CGLOBALL COMMON_BLOCK(CGLOBALL,cgloball)
COMMON_BLOCK_DEF(CGLOBALL_DEF,CGLOBALL);

struct CGLOBALI_DEF{
  mutable int EWAPPROX,MODEL,HIGGSTYPE,EWSCHEME,FLOOPS;
  mutable int SECTOR,MHLOOPS,PROCID;
  mutable int N_ITERATIONS1,N_ITERATIONS2;
  mutable int N_POINTS[7];
  mutable int N_P,N_V;
  mutable int SIGN1,SIGN2,NLO_LOOPS,PS_DIMENSION;
  mutable int PARTICLE_IDS[10];
  mutable int PS_LOOPS,SUB_NUMBER,LOOPS_SUB_LO,LOOPS_SUB_NLO;
};
#define CGLOBALI COMMON_BLOCK(CGLOBALI,cglobali)
COMMON_BLOCK_DEF(CGLOBALI_DEF,CGLOBALI);

struct CGLOBAL2_DEF{
  mutable int N_KIN,N_QED;
};
#define CGLOBAL2 COMMON_BLOCK(CGLOBAL2,cglobal2)
COMMON_BLOCK_DEF(CGLOBAL2_DEF,CGLOBAL2);

struct ANOM_SWITCH_DEF{
  mutable bool WITH_ANOM;
};
#define ANOM_SWITCH COMMON_BLOCK(ANOM_SWITCH,anom_switch)
COMMON_BLOCK_DEF(ANOM_SWITCH_DEF,ANOM_SWITCH);

struct ANOMHIGGS_DEF{
  mutable bool WITH_ANOMHIGGS;
};
#define ANOMHIGGS COMMON_BLOCK(ANOMHIGGS,anomhiggs)
COMMON_BLOCK_DEF(ANOMHIGGS_DEF,ANOMHIGGS);

struct KK_SWITCH_DEF{
  mutable bool WITH_KK;
};
#define KK_SWITCH COMMON_BLOCK(KK_SWITCH,kk_switch)
COMMON_BLOCK_DEF(KK_SWITCH_DEF,KK_SWITCH);
```

```
struct CSCALES_DEF{
  mutable double MUFSQ[25][2],MURSQ[25][2],ALS[25][3],XIR,XIF;
  mutable double MUR_USER,MUF_USER;
  mutable int ID_MUR,ID_MUF;
};
#define CSCALES COMMON_BLOCK(CSCALES,cscales)
COMMON_BLOCK_DEF(CSCALES_DEF,CSCALES);

struct BRANCH_DEF{
  mutable double BWNE,BWUD,BWTB,BZNN,BZEE,BZUU,BZDD,BZTT;
  mutable double BHWW,BHZZ,BHGG,BHTT,BHBB,BHCC,BHTAU,BHMU;
  mutable double BHGAM, BHGAMZ, XGW, XGZ, XGH, GAMT;
};
#define BRANCH COMMON_BLOCK(BRANCH,branch)
COMMON_BLOCK_DEF(BRANCH_DEF,BRANCH);

struct SPLITCB_DEF{
  mutable bool PRINTOUTPUT, ALLSUBPROCS;
  mutable int SUBPROCID,PARTICLEID[10],IHACK,SUBPROCCOUNTER,GLUONID;
};
#define SPLITCB COMMON_BLOCK(SPLITCB,splitcb)
COMMON_BLOCK_DEF(SPLITCB_DEF,SPLITCB);

struct CQQHQQA_DEF{
  mutable double FCPLA[2][6][4],FCPLA1[2][4][4],FCPLA2[2][4][4],FCPLA3[2][4][4];
  mutable int V2INI1[4],V3INI1[4],V2INI2[4],V3INI2[4],V2INI3[4],V3INI3[4];
};
#define CQQHQQA COMMON_BLOCK(CQQHQQA,cqqhqqa)
COMMON_BLOCK_DEF(CQQHQQA_DEF,CQQHQQA);

struct LHCOUP_DEF{
  mutable double TREEFACW,TREEFACZ,LOOPFAC;
};
#define LHCOUP COMMON_BLOCK(LHCOUP,lhcoup)
COMMON_BLOCK_DEF(LHCOUP_DEF,LHCOUP);
```

Bibliography

[1] I. Newton, *Philosophiae naturalis principia mathematica*. J. Societatis Regiae ac Typis J. Streater, 1687.

[2] J. C. Maxwell, *A dynamical theory of the electromagnetic field*, *Phil.Trans.Roy.Soc.Lond.* **155** (1865) 459–512.

[3] S. Frixione and B. R. Webber, *Matching NLO QCD computations and parton shower simulations*, *JHEP* **06** (2002) 029, [hep-ph/0204244].

[4] P. Nason, *A new method for combining NLO QCD with shower Monte Carlo algorithms*, *JHEP* **11** (2004) 040, [hep-ph/0409146].

[5] S. Frixione, P. Nason and C. Oleari, *Matching NLO QCD computations with Parton Shower simulations: the POWHEG method*, *JHEP* **11** (2007) 070, [arXiv:0709.2092].

[6] K. Arnold, J. Bellm, G. Bozzi, M. Brieg, F. Campanario *et. al.*, *VBFNLO: A Parton Level Monte Carlo for Processes with Electroweak Bosons – Manual for Version 2.5.0*, arXiv:1107.4038.

[7] M. Bähr et al., *Herwig++ Physics and Manual*, *Eur. Phys. J.* **C58** (2008) 639–707, [arXiv:0803.0883].

[8] K. Arnold, L. d'Errico, S. Gieseke, D. Grellscheid, K. Hamilton *et. al.*, *Herwig++ 2.6 Release Note*, arXiv:1205.4902.

[9] D. Barber, U. Becker, H. Benda, A. Boehm, J. Branson *et. al.*, *Discovery of Three Jet Events and a Test of Quantum Chromodynamics at PETRA Energies*, *Phys.Rev.Lett.* **43** (1979) 830.

[10] European Muon Collaboration , J. Aubert *et. al.*, *The ratio of the nucleon structure functions $F2_n$ for iron and deuterium*, *Phys.Lett.* **B123** (1983) 275.

[11] UA1 Collaboration , G. Arnison *et. al.*, *Experimental Observation of Lepton Pairs of Invariant Mass Around* $95\mathrm{GeV}/c^2$ *at the CERN SPS Collider*, *Phys.Lett.* **B126** (1983) 398–410.

[12] CDF Collaboration , F. Abe *et. al.*, *Observation of top quark production in $\bar{p}p$ collisions*, *Phys.Rev.Lett.* **74** (1995) 2626–2631, [hep-ex/9503002].

[13] D0 Collaboration , S. Abachi *et. al.*, *Observation of the top quark*, *Phys.Rev.Lett.* **74** (1995) 2632–2637, [hep-ex/9503003].

[14] ATLAS Collaboration , G. Aad *et. al.*, *Observation of a new particle in the search for the Standard Model Higgs boson with the ATLAS detector at the LHC*, *Phys.Lett.* **B716** (2012) 1–29, [arXiv:1207.7214].

[15] CMS Collaboration , S. Chatrchyan *et. al.*, *Observation of a new boson at a mass of 125 GeV with the CMS experiment at the LHC*, *Phys.Lett.* **B716** (2012) 30–61, [arXiv:1207.7235].

[16] T. Adye, *Measurements of Higgs Boson Properties in ATLAS*, *Moriond* (2013). Talk.

[17] A. J. Whitbeck, *Measurements of Higgs Boson Properties in CMS*, *Moriond* (2013). Talk.

[18] J. Ellis, R. Fok, D. S. Hwang, V. Sanz and T. You, *Distinguishing 'Higgs' Spin Hypotheses using gamma gamma and WW* Decays*, arXiv:1210.5229.

[19] L. Landau, *On the angular momentum of a two-photon system*, *Dokl.Akad.Nauk Ser.Fiz.* **60** (1948) 207–209.

[20] C.-N. Yang, *Selection Rules for the Dematerialization of a Particle Into Two Photons*, *Phys.Rev.* **77** (1950) 242–245.

[21] A. Djouadi, *The Anatomy of electro-weak symmetry breaking. I: The Higgs boson in the standard model*, *Phys.Rept.* **457** (2008) 1–216, [hep-ph/0503172].

[22] K. Arnold, *Simulation von Partonschauern bei Higgs-Produktion durch Gluonfusion*, *Diploma Thesis* (2009). Universität Karlsruhe, in German.

[23] U. Aglietti, A. Belyaev, S. Berge, A. Blum, R. Bonciani *et. al.*, *Tevatron for LHC report: Higgs*, hep-ph/0612172.

[24] LHC Higgs Cross Section Working Group , S. Dittmaier *et. al.*, *Handbook of LHC Higgs Cross Sections: 1. Inclusive Observables*, arXiv:1101.0593.

[25] R. V. Harlander and W. B. Kilgore, *Next-to-next-to-leading order Higgs production at hadron colliders*, *Phys.Rev.Lett.* **88** (2002) 201801, [hep-ph/0201206].

[26] C. Anastasiou and K. Melnikov, *Higgs boson production at hadron colliders in NNLO QCD*, *Nucl.Phys.* **B646** (2002) 220–256, [hep-ph/0207004].

[27] V. Ravindran, J. Smith and W. L. van Neerven, *NNLO corrections to the total cross-section for Higgs boson production in hadron hadron collisions*, *Nucl.Phys.* **B665** (2003) 325–366, [hep-ph/0302135].

[28] T. Figy, C. Oleari and D. Zeppenfeld, *Next-to-leading order jet distributions for Higgs boson production via weak boson fusion*, *Phys.Rev.* **D68** (2003) 073005, [hep-ph/0306109].

[29] M. Ciccolini, A. Denner and S. Dittmaier, *Electroweak and QCD corrections to Higgs production via vector-boson fusion at the LHC*, *Phys.Rev.* **D77** (2008) 013002, [arXiv:0710.4749].

[30] P. Bolzoni, F. Maltoni, S.-O. Moch and M. Zaro, *Higgs production via vector-boson fusion at NNLO in QCD*, *Phys.Rev.Lett.* **105** (2010) 011801, [arXiv:1003.4451].

[31] R. Alkofer and J. Greensite, *Quark Confinement: The Hard Problem of Hadron Physics*, *J.Phys.* **G34** (2007) S3, [hep-ph/0610365].

[32] D. Gross and F. Wilczek, *Ultraviolet Behavior of Nonabelian Gauge Theories*, *Phys.Rev.Lett.* **30** (1973) 1343–1346.

[33] H. D. Politzer, *Reliable Perturbative Results for Strong Interactions?*, *Phys.Rev.Lett.* **30** (1973) 1346–1349.

[34] V. Gribov and L. Lipatov, *Deep inelastic e p scattering in perturbation theory*, *Sov.J.Nucl.Phys.* **15** (1972) 438–450.

[35] G. Altarelli and G. Parisi, *Asymptotic Freedom in Parton Language*, *Nucl.Phys.* **B126** (1977) 298.

[36] Y. L. Dokshitzer, *Calculation of the Structure Functions for Deep Inelastic Scattering and e+ e- Annihilation by Perturbation Theory in Quantum Chromodynamics.*, *Sov.Phys.JETP* **46** (1977) 641–653.

[37] N. Metropolis and S. Ulam, *The monte carlo method*, *Journal of the American statistical Association* **44** (1949), no. 247 335–341.

[38] G. P. Lepage, *A New Algorithm for Adaptive Multidimensional Integration*, *J.Comput.Phys.* **27** (1978) 192.

[39] G. P. Lepage, *VEGAS: An adaptive multidimensional integration Program*, . CLNS-80/447.

[40] S. Plätzer, *ExSample: A Library for Sampling Sudakov-Type Distributions*, *Eur.Phys.J.* **C72** (2012) 1929, [arXiv:1108.6182].

[41] T. Sjöstrand, S. Mrenna and P. Skands, *PYTHIA 6.4 Physics and Manual*, *JHEP* **05** (2006) 026, [hep-ph/0603175].

[42] S. Catani, F. Krauss, R. Kuhn and B. R. Webber, *QCD Matrix Elements + Parton Showers*, *JHEP* **11** (2001) 063, [hep-ph/0109231].

[43] Z. Nagy and D. E. Soper, *Matching parton showers to NLO computations*, *JHEP* **10** (2005) 024, [hep-ph/0503053].

[44] N. Lavesson and L. Lönnblad, *Extending CKKW-merging to One-Loop Matrix Elements*, *JHEP* **12** (2008) 070, [arXiv:0811.2912].

[45] T. Gehrmann, S. Höche, F. Krauss, M. Schönherr and F. Siegert, *NLO QCD matrix elements + parton showers in –> hadrons*, arXiv:1207.5031.

[46] S. Höche, F. Krauss, M. Schönherr and F. Siegert, *QCD matrix elements + parton showers: The NLO case*, arXiv:1207.5030.

[47] R. Frederix and S. Frixione, *Merging meets matching in MC@NLO*, arXiv:1209.6215.

[48] B. Andersson, *The Lund Model*. Cambridge monographs on particle physics, nuclear physics, and cosmology. Photography by S. Vascotto.

[49] D. Amati and G. Veneziano, *Preconfinement as a Property of Perturbative QCD*, *Phys.Lett.* **B83** (1979) 87.

[50] B. R. Webber, *A QCD Model for Jet Fragmentation Including Soft Gluon Interference*, *Nucl. Phys.* **B238** (1984) 492.

[51] S. Gieseke, C. Röhr and A. Siodmok, *Colour reconnections in Herwig++*, *Eur.Phys.J.* **C72** (2012) 2225, [arXiv:1206.0041].

[52] G. C. Blazey, J. R. Dittmann, S. D. Ellis, V. D. Elvira, K. Frame *et. al.*, *Run II jet physics*, hep-ex/0005012.

[53] G. P. Salam and G. Soyez, *A Practical Seedless Infrared-Safe Cone jet algorithm*, *JHEP* **0705** (2007) 086, [arXiv:0704.0292].

[54] S. Catani, Y. L. Dokshitzer, M. Seymour and B. Webber, *Longitudinally invariant K_t clustering algorithms for hadron hadron collisions*, *Nucl.Phys.* **B406** (1993) 187–224.

[55] S. D. Ellis and D. E. Soper, *Successive combination jet algorithm for hadron collisions*, *Phys.Rev.* **D48** (1993) 3160–3166, [hep-ph/9305266].

[56] Y. L. Dokshitzer, G. Leder, S. Moretti and B. Webber, *Better jet clustering algorithms*, *JHEP* **9708** (1997) 001, [hep-ph/9707323].

[57] M. Wobisch, *Measurement and QCD analysis of jet cross-sections in deep inelastic positron proton collisions at* $\sqrt{S} = 300\ GeV$, .

[58] M. Cacciari, G. P. Salam and G. Soyez, *The Anti-k(t) jet clustering algorithm*, *JHEP* **0804** (2008) 063, [arXiv:0802.1189].

[59] R. K. Ellis, W. J. Stirling and B. R. Webber, *QCD and Collider Physics*. Cambridge monographs on particle physics, nuclear physics, and cosmology. Photography by S. Vascotto.

[60] S. Catani, S. Dittmaier and Z. Trocsanyi, *One loop singular behavior of QCD and SUSY QCD amplitudes with massive partons*, *Phys.Lett.* **B500** (2001) 149–160, [hep-ph/0011222].

[61] A. Gehrmann-De Ridder, M. Ritzmann and P. Skands, *Timelike Dipole-Antenna Showers with Massive Fermions*, *Phys.Rev.* **D85** (2012) 014013, [arXiv:1108.6172].

[62] S. Plätzer and S. Gieseke, *Coherent Parton Showers with Local Recoils*, *JHEP* **01** (2011) 024, [arXiv:0909.5593].

[63] E. Byckling and K. Kajantie, *N-particle phase space in terms of invariant momentum transfers*, *Nucl.Phys.* **B9** (1969) 568–576.

[64] T. Kinoshita, *Mass singularities of Feynman amplitudes*, *J. Math. Phys.* **3** (1962) 650–677.

[65] T. Lee and M. Nauenberg, *Degenerate Systems and Mass Singularities*, *Phys.Rev.* **133** (1964) B1549–B1562.

[66] S. Catani and M.H. Seymour, *A general algorithm for calculating jet cross sections in NLO QCD*, *Nucl. Phys.* **B485** (1997) 291–419, [hep-ph/9605323].

[67] J. M. Butterworth, A. R. Davison, M. Rubin and G. P. Salam, *Jet substructure as a new Higgs search channel at the LHC*, *Phys.Rev.Lett.* **100** (2008) 242001, [arXiv:0802.2470].

[68] T. Plehn, G. P. Salam and M. Spannowsky, *Fat Jets for a Light Higgs*, *Phys.Rev.Lett.* **104** (2010) 111801, [arXiv:0910.5472].

[69] A. Ballestrero, G. Bevilacqua and E. Maina, *A New analysis of PP –> b anti-b l nu jj at the LHC: Higgs and W boson associated production with two tag jets*, *JHEP* **0808** (2008) 059, [arXiv:0806.4075].

[70] D. L. Rainwater, *A New method for measuring the bottom quark Yukawa coupling at the CERN Large Hadron Collider*, *Phys.Lett.* **B503** (2001) 320–324, [hep-ph/0004119].

[71] E. Gabrielli, F. Maltoni, B. Mele, M. Moretti, F. Piccinini *et. al.*, *Higgs Boson Production in Association with a Photon in Vector Boson Fusion at the LHC*, *Nucl.Phys.* **B781** (2007) 64–84, [hep-ph/0702119].

[72] M. L. Mangano, M. Moretti, F. Piccinini, R. Pittau and A. D. Polosa, *ALPGEN, a generator for hard multiparton processes in hadronic collisions*, *JHEP* **07** (2003) 001, [hep-ph/0206293].

[73] F. Maltoni and T. Stelzer, *MadEvent: Automatic event generation with MadGraph*, *JHEP* **0302** (2003) 027, [hep-ph/0208156].

[74] D. Asner, M. Cunningham, S. Dejong, K. Randrianarivony, C. S. Rios *et. al.*, *Search for a Light Standard Model Higgs Boson Produced in Association with a Photon in Vector Boson Fusion*, arXiv:1006.0669.

[75] K. Arnold, T. Figy, B. Jäger and D. Zeppenfeld, *Next-to-leading order QCD corrections to Higgs boson production in association with a photon via weak-boson fusion at the LHC*, *JHEP* **1008** (2010) 088, [arXiv:1006.4237].

[76] K. Arnold, T. Figy, B. Jäger and D. Zeppenfeld, *Higgs boson production in association with a photon via weak boson fusion*, arXiv:1110.2402.

[77] H. Murayama, I. Watanabe and K. Hagiwara, *HELAS: HELicity amplitude subroutines for Feynman diagram evaluations*, *KEK Report* **91-11** (1992).

[78] G. Passarino and M. Veltman, *One Loop Corrections for e+ e- Annihilation Into mu+ mu- in the Weinberg Model*, *Nucl.Phys.* **B160** (1979) 151.

[79] F. Campanario, *Towards pp –> VVjj at NLO QCD: Bosonic contributions to triple vector boson production plus jet*, *JHEP* **1110** (2011) 070, [arXiv:1105.0920].

[80] T. Stelzer and W. Long, *Automatic generation of tree level helicity amplitudes*, *Comput.Phys.Commun.* **81** (1994) 357–371, [hep-ph/9401258].

[81] J. Alwall, P. Demin, S. de Visscher, R. Frederix, M. Herquet *et. al.*, *MadGraph/MadEvent v4: The New Web Generation*, *JHEP* **0709** (2007) 028, [arXiv:0706.2334].

[82] J. Pumplin, D. Stump, J. Huston, H. Lai, P. M. Nadolsky *et. al.*, *New generation of parton distributions with uncertainties from global QCD analysis*, *JHEP* **0207** (2002) 012, [hep-ph/0201195].

[83] H.-L. Lai, M. Guzzi, J. Huston, Z. Li, P. M. Nadolsky *et. al.*, *New parton distributions for collider physics*, *Phys.Rev.* **D82** (2010) 074024, [arXiv:1007.2241].

[84] A. D. Martin, W. J. Stirling, R. S. Thorne and G. Watt, *Parton distributions for the LHC*, *Eur. Phys. J.* **C63** (2009) 189–285, [arXiv:0901.0002].

[85] S. Catani, Y. L. Dokshitzer and B. Webber, *The $k_\perp$ clustering algorithm for jets in deep inelastic scattering and hadron collisions*, *Phys.Lett.* **B285** (1992) 291–299.

[86] S. Frixione, *Isolated photons in perturbative QCD*, *Phys.Lett.* **B429** (1998) 369–374, [hep-ph/9801442].

[87] G. Klämke and D. Zeppenfeld, *Higgs plus two jet production via gluon fusion as a signal at the CERN LHC*, *JHEP* **0704** (2007) 052, [hep-ph/0703202].

[88] V. Hankele, G. Klämke, D. Zeppenfeld and T. Figy, *Anomalous Higgs boson couplings in vector boson fusion at the CERN LHC*, *Phys.Rev.* **D74** (2006) 095001, [hep-ph/0609075].

[89] C. Ruwiedel, N. Wermes and M. Schumacher, *Prospects for the measurement of the structure of the coupling of a Higgs boson to weak gauge bosons in weak boson fusion with the ATLAS detector*, *Eur.Phys.J.* **C51** (2007) 385–414.

[90] J. R. Andersen, K. Arnold and D. Zeppenfeld, *Azimuthal Angle Correlations for Higgs Boson plus Multi-Jet Events*, *JHEP* **1006** (2010) 091, [arXiv:1001.3822].

[91] B. D. Burow, *Mixed Language Programming*, *Proc. Conf. High-Energy Physics CHEP95* (1995) 610–614.

[92] R. Kleiss, W. J. Stirling and S. Ellis, *A New Monte Carlo Treatment Of Multiparticle Phase Space At High-Energies*, *Comput.Phys.Commun.* **40** (1986) 359.

[93] S. Plätzer and S. Gieseke, *Dipole Showers and Automated NLO Matching in Herwig++*, arXiv:1109.6256.

[94] S. Asai, G. Azuelos, C. Buttar, V. Cavasinni, D. Costanzo *et. al.*, *Prospects for the search for a standard model Higgs boson in ATLAS using vector boson fusion*, *Eur.Phys.J.* **C32S2** (2004) 19–54, [hep-ph/0402254].

[95] S. Abdullin, S. Banerjee, L. Bellucci, C. Charlot, D. Denegri *et. al.*, *Summary of the CMS potential for the Higgs boson discovery*, *Eur.Phys.J.* **C39S2** (2005) 41–61.

[96] M. Cacciari, G. P. Salam and G. Soyez, *FastJet User Manual*, *Eur.Phys.J.* **C72** (2012) 1896, [arXiv:1111.6097].

[97] M. Cacciari and G. P. Salam, *Dispelling the N^3 myth for the k_t jet-finder*, *Phys.Lett.* **B641** (2006) 57–61, [hep-ph/0512210].

[98] V. Del Duca, G. Klämke, D. Zeppenfeld, M. L. Mangano, M. Moretti *et. al.*, *Monte Carlo studies of the jet activity in Higgs + 2 jet events*, *JHEP* **0610** (2006) 016, [hep-ph/0608158].

[99] L. D'Errico and P. Richardson, *A Positive-Weight Next-to-Leading-Order Monte Carlo Simulation of Deep Inelastic Scattering and Higgs Boson Production via Vector Boson Fusion in Herwig++*, arXiv:1106.2983.

[100] B. Jäger and G. Zanderighi, *Electroweak W+W-jj prodution at NLO in QCD matched with parton shower in the POWHEG-BOX*, arXiv:1301.1695.

[101] S. Alioli, P. Nason, C. Oleari and E. Re, *A general framework for implementing NLO calculations in shower Monte Carlo programs: the POWHEG BOX*, *JHEP* **1006** (2010) 043, [arXiv:1002.2581].

[102] S. Alioli, P. Nason, C. Oleari and E. Re, *NLO Higgs boson production via gluon fusion matched with shower in POWHEG*, *JHEP* **04** (2009) 002, [arXiv:0812.0578].

[103] S. Höche, F. Krauss, M. Schönherr and F. Siegert, *A critical appraisal of NLO+PS matching methods*, arXiv:1111.1220.

[104] D. L. Rainwater, R. Szalapski and D. Zeppenfeld, *Probing color singlet exchange in Z + two jet events at the CERN LHC*, *Phys.Rev.* **D54** (1996) 6680–6689, [hep-ph/9605444].

[105] P. Nogueira, *Automatic Feynman graph generation*, *J.Comput.Phys.* **105** (1993) 279–289.

Danksagung

Mein Dank geht an Prof. Dr. Dieter Zeppenfeld für die Möglichkeit der Mitarbeit in seiner Arbeitsgruppe. Bei Prof. Dr. Matthias Steinhauser bedanke ich mich für die Übernahme des Korreferats.

Ich danke Dr. Francisco Campanario und meinen anderen Bürokollegen für Diskussionen über physikalische Probleme und andere Dinge. Weiterer Dank geht an die Korrekturleser der vorliegenden Arbeit. Der übrigen Arbeitsgruppe bin ich dankbar für das angenehme Arbeitsumfeld, das mir geboten wurde.

Ein großer Dank geht an Dr. Simon Plätzer für seine Zusammenarbeit und Hilfe. Weiterhin möchte ich insbesondere Dr. Stefan Gieseke danken, der stets ein offenes Ohr für Fragen hatte und mir durch seine gelassene Art ein Vorbild war.

Zuletzt gilt mein besonderer Dank Eva Richter, die mich während der letzten Jahre stets unterstützt und motiviert hat.